Chemical Reaction Engineering Modeling of Flow Field in Polymer Electrolyte Fuel Cell

Ma Yulei

Contents

Contents

Introduction

0.1 Polymer Electrolyte Fuel Cell

0.1.1 Background

As the increase of population and development of economy, the energy demand also grows at a rapid rate. As shown in Fig. 0.1, the global primary energy consumption was 176431 TWh (terawatt-hours) in 2021, which is nearly 6.18 times to 28564 TWh in 1950.[1] Especially, 77.1 % of the global primary energy consumption was from fossil fuel (crude oil, coal, and natural gas).

However, the energy resources, especially fossil fuels, are limited. According to the estimation by BP Statistical Review of World Energy, years of fossil fuel reserves left of coal, oil and gas in 2020 are 139, 54 and 49 years, respectively.[2] Humans are about to face the exhaustion of resources and energy dilemma as the increasing demand of energy. More importantly, as the price of the high-speed modernization, phenomena, *i.e.,* the rise in sea level, extreme climate, food security problems, ecosystem degradation, *etc.*, appear, due to the global warming, which is considered caused by the greenhouse gas emission such as carbon dioxide (CO_2). According to the data applied from National Oceanic and
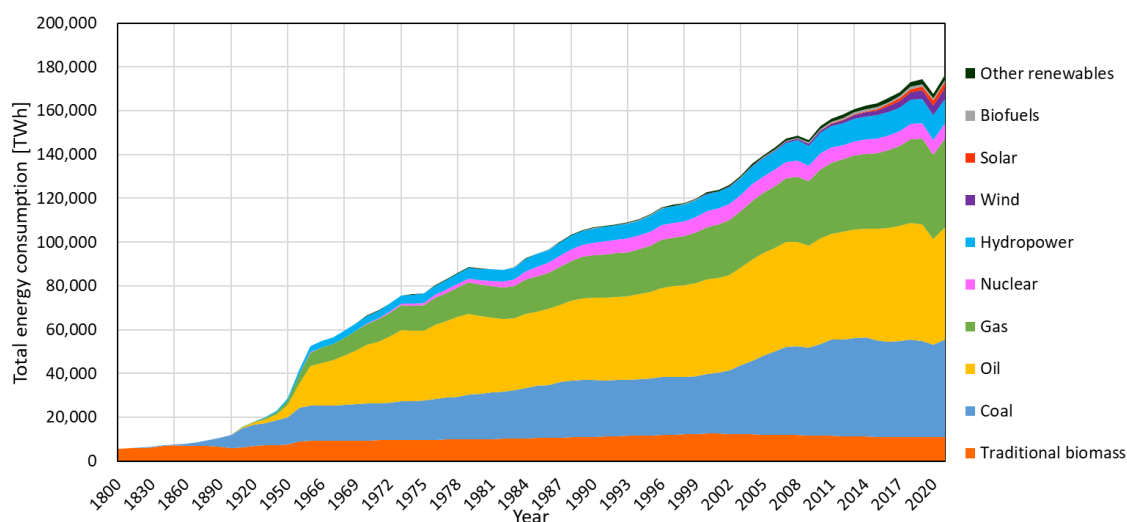
Figure 0.1: Global primary energy consumption[1]
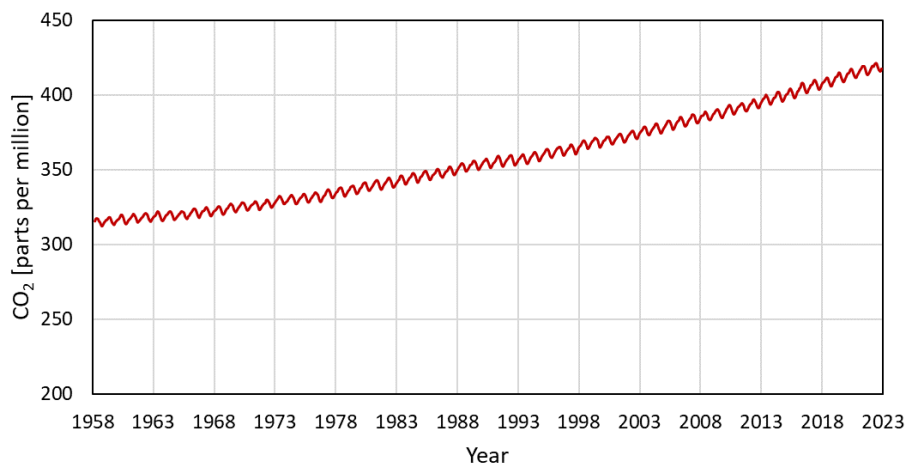
Figure 0.2: Global CO_2 content[3]

Atmospheric Administration (NOAA), the global CO_2 content had been varied in a limited range near 220 ppm before the first industrial revolution, while in the recent 70 years, the continuously increasing CO_2 level has reached 419 ppm in September 2022,[3] as shown in Fig. 0.2. As the result, the sea level rises 103 mm in August 2022 comparing to that in January 1993.[4]

Addressing the situation of global warming, the Paris Agreement was negotiated in 2015 United Nations Climate Change Conference (COP21), and the goal of limiting global warming to well below 2 °C compared to pre-industrial levels was set. The concept of carbon neutrality was also made, to achieve which the measures of carbon offsetting and reducing emissions are required.

To mitigate this situation, diverse energy resources should be utilized. Hydrogen (H_2), which provides high heating value without producing CO_2 has been expected as an ideal energy carrier. Meanwhile, the fuel cell, which is regarded as an important energy conversion device of H_2, has been paid attention for decades.

Fuel cell

A fuel cell is an electrochemical device that converts the chemical energy of a fuel and an oxidizing agent into electricity through a pair of redox reactions. In a fuel cell, the fuel (*e.g.*, hydrogen, hydrocarbon, *etc.*) and the oxidizing agent (usually oxygen in air) can be fed to react and convert chemical energy into electricity continuously at normal or high temperature. Comparing to the traditional energy conversion device such as internal combustion engines, the fuel cell has higher theoretical maximum efficiency[5], since there is no limitation of Carnot's efficiency which exists in the former. According to the advantages mentioned above, fuel cells are supposed to be applied in various fields from

transportation, *i.e.,* vehicles, trains, airplanes, boats, and submarines, to home-use cogeneration systems which can work in power outage,[6, 7] and portable power sources for laptops and smart phones.[8]

Fuel cells which are fed by H_2 as fuel can be classified in several types according to the electrolytes, which have been realized and are currently in use and development, as below.

(1) Alkaline fuel cell (AFC)

AFCs were the first type of fuel cells used inside power generators. The AFCs were developed by the space sector due to their wide operative temperature ranges. AFCs use liquid KOH as the electrolyte and are fueled by hydrogen. The oxidant must be pure oxygen, not air, due to the carbonatation of the electrolyte by CO_2 contained in the air (300 ppm). Each cell generates a voltage between 0.5 V and 0.9 V depending on the design with an electrical efficiency that can be up to 65 %.[6]

(2) Phosphoric acid fuel cell (PAFC)

PAFCs were the first type of cell to be commercialized. The electrolyte used inside PAFCs is phosphoric acid (H_3PO_4), requires operative temperatures between 150 ℃ and 220 ℃ to properly work, due to its poor ionic conductivity. However, relatively impure hydrogen is allowed, owing to their high operation temperature. Their cell efficiency is 37–42 %, and the total efficiency can be over 60 % by combined with heat generated system.[6]

(3) Molten carbonate fuel cell (MCFC)

MCFCs operate at temperatures up to 650 °C which use a liquid solution of alkali carbonate salts as the electrolyte. Due to the high temperature, MCFCs can be fueled with gases like methane, natural gas, or coal reformed gases. However, they also suffer from many problems such as fast degradation of the cell structure and continuous loss of the electrolyte, also because of the high temperature. Their efficiency can go up to 45 %, and total efficiency can exceed 50–60 % by utilizing the waste heat.[6]

(4) Solid carbonate fuel cell (SOFC)

SOFCs are another technology of high temperature fuel cell operate at 800–1000 °C, and the electrolytes are Yttria-stabilized zirconia (YSZ). A wide array of different fuels containing hydrogen (coal gas, biogas, propane, natural gas, and hydrogen) can be used since the fuel reforming takes place directly inside the cell because of the high temperature. High quality heat can also be generated so that the total efficiency can be up to 80 %. However, the high temperature drawback is that heat control inside this type of fuel cell becomes difficult, so that these cells can hardly be integrated on portable systems for electric power generation.[6]

(5) Polymer electrolyte fuel cell (PEFC)

The electrolyte in the PEFCs are ion exchange membranes operating at 60–120 ℃. Their overall cell efficiency can be 30–60 %.[6]

Owing to the relatively low operating temperature of PEFCs, only a short warm-up time is needed so that they can be started quickly. They do not require use of hazardous fluids, so that they are easy to repair, maintain, and recycle. Consequently, PEFCs are being pursued for a wide variety of applications and are also expected to play a dominant role in future energy solutions.

Nowadays, PEFCs have already been commercialized in many applications, and are still processing rapid growth and development. For example, home-use cogeneration system *ENE-FARM* has been produced in 2008 and commercialized in 2009. Fuel cell vehicles (FCVs) of first and second generation *MIRAI* produced by Toyota Motor Corporation has been commercialized in 2014 and 2020 respectively.[9] Associations such as Japan New Energy and Industrial Technology Development Organizations (NEDO), United States Department of Energy (DOE) and European Union Fuel Cells and Hydrogen 2 Joint Undertaking (EU-FCH2JU) respectively demonstrated their PEFC power density goals and technology roadmaps.

0.1.2 Work principles of PEFC
Components of PEFC

The smallest integrated component of the PEFC system is a single cell. To extract higher power, single cells are usually connected in series, which is called a cell stack. In this study, the objective is mainly focused on the single cell, so the PEFC mentioned in this dissertation refers to the single cell, if there is no specific explanation.

The core of a PEFC is the membrane electrode assembly (MEA). The MEA consists of the following components: proton exchange membrane (PEM), which is the electrolyte; anode and cathode catalyst layers (CLs), which act as the electrodes. These three parts are joined together by usually hot-pressing process. For the reactant gas uniformly supplied to the CLs effectively, gas diffusion layers (GDLs), in which the gas permeates and mixes, are also used. The microporous layers (MPLs) are also sometimes fabricated on the GDLs to manage water. The MEA as well as the GDLs for anode and cathode sides are sandwiched between bipolar plates (BPs), which are the mechanical support structure in the PEFC. On PEFCs' catalyst layers, the catalyst nanoparticles (usually platinum) are supported on carbon black (CB) particle. The CB particles are covered with ionomer, which provides the proton conduction path. The reactions below take place on the surface of catalyst.
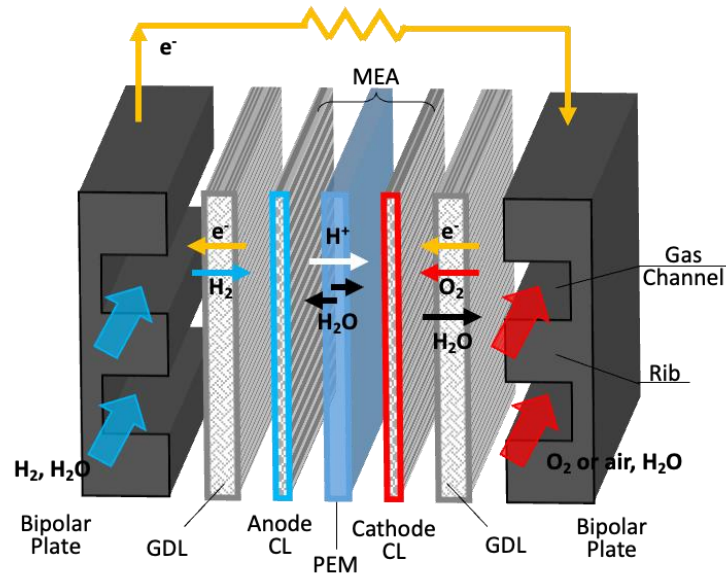
Figure 0.3: Processes in PEFC

Anode:	$2H_2 \rightarrow 2H^+ + 2e^-$	(0.1)
Cathode:	$O_2 + 4H^+ + 4e^- \rightarrow 2H_2O$	(0.2)
Total reaction:	$2H_2 + O_2 \rightarrow 2H_2O$	(0.3)
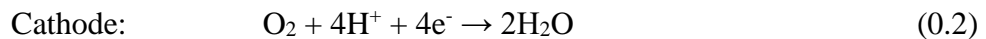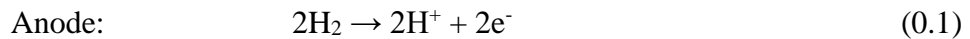
On the anode side, hydrogen oxidation reaction (HOR) (0.1) converts the supplied hydrogen to proton (H^+) and electron (e^-). Protons conduct from anode to cathode through the PEM, while the electrons generated on anode CL conduct the GDL, BPs and outer circuit to the cathode side. On the cathode side, the supplied oxygen reacts with protons and electrons in oxygen reduction reaction (ORR) (0.2), and water produces. The generated water transfers through the GDL to the gas channel. The ORR reaction is exothermal, so the temperature in cathode CL (CCL) is usually higher than the other parts, and the water droplets usually condense in the GDL and gas channels, especially at the high current density. On the other hand, the ORR at cathode is inherently slower by 6 orders of magnitude than the HOR at anode,[10] so that most of research focus on the processes at cathode. Typical processes in a PEFC are shown in Fig. 0.3.

Performance of PEFC

Theoretically, the maximum cell voltage is determined by thermodynamics. Electromotive force (EMF) can be calculated by Eq. (0.4).

$$E = \frac{-\Delta G}{zF} \tag{0.4}$$
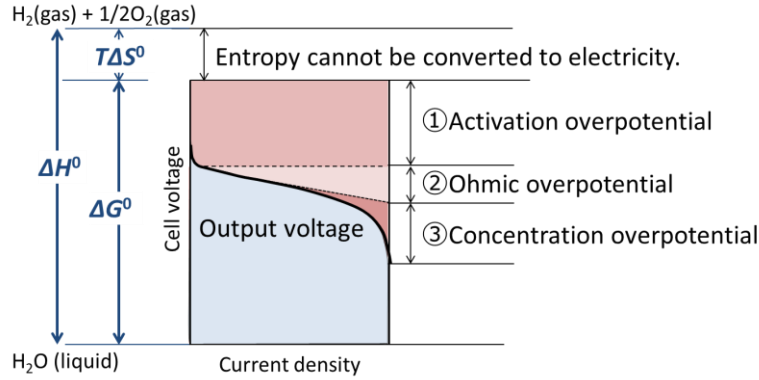
Figure 0.4: Polarization curve and overpotential

In this equation, ΔG is Gibbs free energy of reaction, F is Faraday constant, and z is the stoichiometry number of exchanged electrons which is 2 for reaction (0.3). The maximum efficiency (limited by thermodynamics) can be calculated by Eq. (0.5).

$$\eta = \frac{\Delta G}{\Delta H} \times 100 \ \% \tag{0.5}$$

ΔH represents the enthalpy of reaction. At 80 °C, the theoretical maximum efficiency is 80 % based on the higher heating value (HHV).

According to the Nernst equation (0.6), the theoretical emf is also determined by activity of each component in PEFC.

$$E = E^{\circ} + \frac{RT}{2F} \ln(\frac{a_{H_2} a_{O_2}^{1/2}}{a_{H_2O}}) \tag{0.6}$$

where a represents the activity. When the gas is regarded as ideal gas, the activity can be calculated from partial pressure, as shown in Eq. (0.7). And for liquid water, $a_{H_2O} = 1$.

$$a_i = \frac{p_i}{P^{\circ}} \ , P^{\circ} = \begin{cases} 0.1 \ \text{MPa}, i = H_2, O_2 \\ P_S^{\text{sat}}, i = H_2O \end{cases} \tag{0.7}$$

However, the actual cell voltage is lower than theoretical EMF, as the current increases, due to the 4 kinds of loss or overpotential: activation loss, ohmic loss, concentration loss, and crossover loss. The activation loss occurs due to the properties of electrodes. The activation loss is mainly contributed to the ORR at cathode[11] since it is apparently slower than HOR as mentioned above. The ohmic loss is caused by ohmic resistance when ions and electrons cross the electrolyte or contact parts. The concentration loss is from the mass transport resistance due to the concentration gradient. And the crossover loss origins from the fuel or oxidant flux across the electrolyte without electrochemical reaction. Cell performance of PEFC can be valued by polarization curve which plots the relationship of

output cell voltage and current density. A typical polarization curve is shown in Fig. 0.4, when crossover loss is ignored.

0.1.3 Issues of PEFC

Although PEFCs have attracted attention owing to their advantages and their remarkable technical progress in recent years, further development is still required to promote their larger scale commercialization.[12] The stack power densities with and without end plates in the second-generation MIRAI, the fuel cell vehicles (FCV) launched by Toyota in 2020, have reached 4.4 kW/L and 5.4 kW/L, respectively.[12] On the other hand, according to NEDO roadmap, the targets of the stack power density for automotive application are 6.0 kW/L and 9.0 kW/L by 2030 and 2040.[12] The EU-FCH2JU demonstrated the goal of PEMFC stack is 9.3 kW/L by 2024[12]. There is still a gap between the goal and current status.

Improving the activity of catalyst and the mass transport capacity are the direct method to develop the PEFC's efficiency, since the kinetic and transport losses contribute to more than 65 % of the cathode losses which dominate the total cell performance losses.[13] For PEFC cathode CL, although increasing the Pt-loading is beneficial for the efficiency, the cost of platinum group metal (PGM), which accounts around 50 % of the stack cost,[14] prevents the large-scale commercialization of PEFC. Therefore, developing novel non-PGM catalyst with high activity and durability is critically important.[2] On the other hand, the mass transport resistance, especially for future ultrahigh-power-density operations, should also be decreased[12] by *e.g.*, controlling the complex structure of CL as well as GDL,[15] optimizing the flow field structure,[12] *etc*.

Water management is another essential way to achieve the maximum cell performance. The supplied gases need to be humidified in order to prevent dry-out and maintain the proton conductivity of PEM. On the other hand, the liquid water can be filled in the void of catalyst layer and GDL. When a large amount of liquid water accumulates in the porous layer's pores, the oxygen transport resistance increases, and the oxygen mass flow rate decreases.[16] This kind of phenomenon is called flooding which usually happens on cathode side in PEFC. Therefore, the dry-out and the flooding should both be avoided. Water management relies on the improvement of material wettability and control of the operating conditions.

Besides improving power densities, reducing cost and increasing durability are also critical issues of PEFCs. These three criteria are connected to and also constrained by each other.[12] Due to the complicated phenomenon in PEFC, establishing well-used theories to understand the phenomenon, which makes developing design procedures to

maximize the power density output capacity possible, offers promising ways for the development of PEFC.

0.2 Cell Performance Improvement of PEFC

The performance of PEFC is determined by the local current density or the ORR rate. Extensive studies have been carried out on explorations of the effects of factors such as temperature,[17] total pressure,[18] oxygen partial pressure,[19] relative humidity (RH)[20] on the ORR rate as well as the mass transfer. However, these parameters have distributions either in a stack and in a single cell, and they are dependent on each other due to the complex phenomenon including inherent three-dimensional heat transport, species and charge transport, multi-phase flow, and electrochemical reactions.[21]

0.2.1 Analysis method of physicochemical properties distributions
Experimental methods

The distributions of properties, especially gas composition inside the cell, are difficult to be measured precisely without complicated equipment and high experimental techniques. Technologies such as gas chromatograph and laser absorption spectroscopy can be used to analyze the gas composition inside the cell.[22] However, these *ex-situ* characterizations only yield the effective properties of the whole layer and do not resolve the local impact of morphological heterogeneity.[23] By inserting an oxygen sensor, such as optical fiber covered by oxygen-sensitive dye film,[24] microelectrochemical cell,[25] into a specific location in a cell, the oxygen partial pressure can be measured *in situ*. Micro-gas-chromatograph and tunable diode laser absorption spectroscopy techniques can be utilized to measure the water vapor partial pressure *in situ*.[5] However, only limited locations in the cell can be measured. By employing neutron and X-ray imaging,[26, 27] the liquid water distribution can be measured, whereas the gas composition distribution remains unknown. To understand the different properties distributions in PEFC, numerical computation method is required.

Simulation methods

Mathematical and computational modeling allow the prediction of the behavior of certain parameters in PEFC which would be nearly impossible to measure experimentally.[28] A large amount of numerical models which provide detailed

information of fluid flows, heat transfer, and electrochemical reactions, have been established to help understanding the complex phenomenon within the fuel cell.[29] Typically, computational fluid dynamics (CFD) was widely employed, which uses governing equations that apply to all the regions within a PEFC to provide solutions for multiple properties distributions.[30] The PEFCs can be thus analyzed and optimized over a wide range of conditions with innovative flow field designs.[16] However, most of models using CFD requires large workload and long time to calculate especially in complex flow field,[31, 32] and therefore, they are mainly applied to analyze the detailed behaviors inside PEFCs.

Moreover, there is no necessity of giving precise values for every physical quantity over the computational domain, the numerical models on well-verified transport modeling of PEFC can accurately predict the trends of cell performance varying operating parameters.[21] The model containing well-described transport phenomenon can thus provide promising results, especially the fluid velocity and pressure distributions inside the PEFC, which are difficult to be measured experimentally.

0.2.2 Flow field

The flow fields of the reactant and coolant are fabricated on the BP, which plays an important part in flow distribution, current collection, and heat dissipation, and water management.[12, 33] The BP comprises more than 60 % of the weight and more than 30 % of the total cost of the PEFC stack.[34, 35] By optimizing the design of the BP, the overall PEFC stack performance in terms of costs can be improved about 50 %.[36] The mass transport capacity is an important criterion of a BP design, which mainly depends on the flow field design.[37] A good flow field requires (a) providing even distribution of the reactant gases, (b) having enough rib area to provide high electronic conductivity, (c) having a low pressure drop, (d) removing liquid water efficiently to prevent flooding, (e) supplying oxygen to the catalytic layer sufficiently.[33]

The conventional design of the flow fields contains serpentine, parallel, interdigitated and the hybrid designs of them, as shown in Fig. 0.5(a)–(c). The serpentine flow field has a good performance, good water removal topology, and provides a good under-rib convection.[38] However, high resistivity to flow, as well as pressure drop, and non-uniform reactant distribution in the GDL are the disadvantages of the serpentine design.[39] The parallel flow field has a low pressure drop, which can be beneficial for the entropy production rate.[33] However, this feature is not capable of pushing out the liquid water efficiently.[33] The liquid water grows and results in blocking the flow field channels, leading to a non-uniform distribution of reactant gases and temperature and reducing the
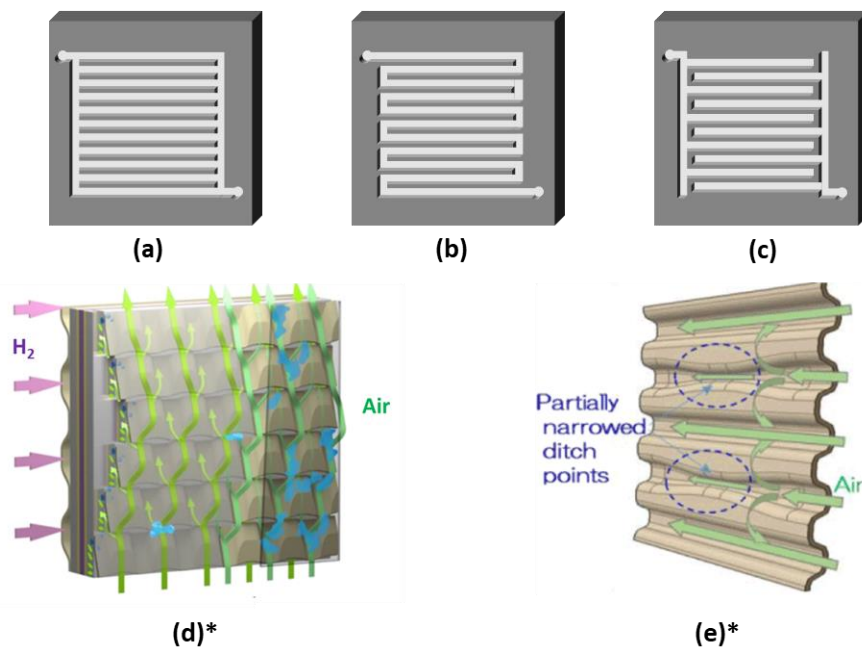
Figure 0.5: Flow field designs: (a) parallel, (b) serpentine, (c) interdigitated, (d) 3D fine-mesh[9], (e) partially narrowed[9]

overall performance and the life of the system.[40] The interdigitated flow fields have dead-end channels, aiming at forcing gas to flow through the GDL to the CL and removing water efficiently.[11] Interdigitated designs generally have better performance than parallel designs but worse than serpentine designs.[41, 42] However, the interdigitated design is vulnerable for the high pressure drop and possible long-term damage to the GDL and MEA.[33] In addition, gas flows through the GDL via channel-to-channel pressure difference is known as under-rib convection or cross flow, which also promotes the under-rib mass transfer,[43] in cases of both the serpentine and interdigitated. On the other hand, the cross flow always occurs along with the phenomenon that the gas flows into the GDL, which is called diving flow in this study.

Currently, some innovated flow field designs are developed and commercialized, for example the three-dimension (3D) fine-mesh flow field of the first-generation MIRAI produced by Toyota, as shown in Fig. 0.5(d). The 3D fine-mesh flow field has baffles stamped in a fish-scale pattern, which exhibit efficient mass transfer and good water removal.[12] However, due to the complex structure, high cost and additional pressure loss become the main drawbacks of the 3D fine-mesh flow filed. Additionally, the tearing fabrication process may cause the fracture and surface cracks, exposing the metallic substrate to an acidic electrochemical environment, which decreases the durability.[12, 44]

In 2020, Toyota launched the second-generation MIRAI, which applied the two-dimensional straight flow channel with partially narrowed ditch points, as shown in Fig. 0.5(e). This narrowed channel increases the local gas velocity as well as the local hydraulic resistance, which forces a portion of the reactant gas to flow through the GDL to the catalytic layer under the gas channels and ribs. The simplification of the BP also helps decrease the manufacturing cost and pressure loss. However, although the partially narrowed flow field was developed to balance the mass transfer and pressure drop, limited study reveals the relationship between the partially narrowed channel enhancement on the mass transfer and the cell performance quantitively, which is necessary to be comprehended to improve the stack power density and achieve the goals.

The partially narrowed channel can be regarded as a baffle or obstacle, which shrinks the cross sectional area of a part of the channel and locally increases the pressure drop. The performance of PEFC with partially blocked baffle flow field has been discussed in many studies, most of which were by numerical simulations. By installing the partially blocked baffle in a single channel, where the height of the baffle to the straight channel were 60–90 %, the net power density of the cell increases about 4–10 %, according to the numerical models.[45, 46, 47] The height and the number of the baffles were important parameters, increasing which can reduce the concentration overpotential but increase the pressure drop, therefore the optimal height and the number of the baffles exist, according to numerical models[47, 48, 49]. On the other hand, the length of the baffle does not obviously affect the cell performance, and the net power density even decreases by increasing the length due to the increased pressure drop.[49] The shape design of the baffle is another popular direction in this field, since the cell performances in cases of different baffle shapes can be easily obtained by computational fluid dynamic (CFD) method. The cell performance simulations with different shapes of triangle, trapezoid, semicircle, and the mixture of them were carried out to discuss the optimal shape of the baffle, which can lead the gas to dive into the GDL smoothly and improve the mass transfer with a minimized pressure drop.[46, 50, 51, 52, 53] Additionally, instead of a single straight gas channel flow field, the parallel flow fields with baffles arranged in stagger pattern was also investigated by experiment and simulation, which has better performance than the neat-arranged pattern.[54] However, most of the studies only discussed the mass transfer by one-sidedly investigating the reactant concentration distribution without discussing the detailed mass transport mechanism. Shen *et al.* offered the synergy principle to understand and evaluate the improvement of mass transfer,[55] but the relative magnitude of diffusion and convection fluxes, as well as the cell performance improvement due to the diving flow and cross flow phenomenon, were not mentioned. Although the oxygen

diffusion and convection fluxes were compared by Yin *et al.* [52] and Zhang *et al*[56], they did not investigate the mass transport mechanism between adjacent channels in case of the staggered pattern. Thus, the phenomenon in the partially narrowed flow channel should be further investigated.

0.2.3 Operating conditions and water management

The operating conditions also dramatically affect the PEFC performance. As what is mentioned above, parameters, *e.g.*, pressure, temperature, RH, *etc.*, remarkably influence the PEFC performance. Coolant flow rate is a factor for removing the heat to control and adjust the temperature,[57] particularly in PEFC stack system, which indirectly affects the cell performance. A proper stoichiometric ratio, which is equated with a proper water management, are essential for obtaining high efficiency.[58] Additionally, the inappropriate operating conditions may cause flooding issues or fuel/oxygen starvation, which is related to the performance decrease and irreversible CL degradation.[59]

The water management is the main concern when optimizing the operating conditions. The RH of inlet gases should be humidified sufficiently to prevent dehydration of PEM, which results in high ohmic loss in PEM and proton and oxygen transfer resistance in CL.[60, 61] On the other hand, the RH in the gas channel should be controlled to be lower than the saturated pressure of water vapor to avoid flooding, which may cause high mass transport resistance,[61] unstable cell performance,[62] and even degradation of the cell durability.[63] In addition, the water transport inside PEFC is complex, which contains 3 different mechanisms: electro-osmotic drag, diffusion, and hydraulic permeation.[64] The electro-osmotic drag occurs when the protons conduct through the PEM, so that the water molecules are accompanied by the proton. The diffusion is caused by the water concentration difference between anode and cathode sides. The hydraulic permeation origins from the gas phase pressure gradient across the MEA, which can be neglectable when the pressure difference between anode and cathode is not obvious. These three different fluxes are determined by multiple properties distributions in the PEFC, meanwhile they determine the water transport, which makes the water management becoming more complicated.

Moreover, the PEFC system without external humidification is preferable, since the cost of the humidifier can be reduced. The humidification requirements of the anode and cathode are different. At anode, the humidified hydrogen at the PEFC outlet can be recirculated to the inlet, so that the water generated in the PEFC can be applied to humidify the system itself, meanwhile the unreacted hydrogen can be also utilized, and the anode humidifier can be thus removed.[65] Therefore, the gas recirculation flow rate is

another important parameter, which is similar to the effects of the stoichiometry, in case of the PEFC system with hydrogen recirculation. However, the effects of this parameter and the optimization method in this kind of system is seldom reported in the literature.

0.3 Objective and Outline

As mentioned above, the processes including momentum, mass and heat transfer, and electrochemical reaction inside PEFC influence the distributions of properties, *i.e.*, temperature, pressure, velocity, composition, potential, *etc.*, which reversely affect the transport phenomenon and reactions. However, most of the distributions of properties are approximately impossible to be obtained experimentally. Although a large number of simulation models which were employed to explain the complex phenomenon inside PEFC were reported, most of them are computationally expensive, time-consuming, and unable to separate the effects of parameters, so that they are unsuitable to meet the requirement of design procedure and controller. Therefore, a model which can explain the multiple behaviors with less computational load for PEFC design and operation is required.

In this study, the theories of chemical engineering are applied to PEFC, since the latter can be regarded as a reactor. The chemical engineering has proven theories which have been verified in industry for above a century and is considered that can be applied in more fields. Moreover, the study of PEFC in the perspective of chemical engineering is lack of report. Therefore, this study intends to demonstrate the possibility and the method which employs the theories of chemical engineering to PEFCs, in order to improve their performance for their large-ground commercialization.

From the viewpoint above, 4 topics were investigated and summarized. The outline of this dissertation is described below:

Introduction (this chapter) describes the background and work principles of PEFC. The literature review of cell performance improvement issues, particularly flow fields and operating conditions, are presented.

Chapter 1 exhibits the analysis method of cathode ORR kinetics and physicochemical properties from the cathode CL Pt-loading dependency. The cathode CL dimensionless model[66] is applied to explain the relative rates among ORR reaction, oxygen diffusion, and proton conduction in the perspective in chemical reaction engineering, so that the limitation step can be clearly demonstrated under different conditions. The Pt-loading

dependency of cell performance is investigated by both experiment and theory model. The model also indicates the optimal Pt-loading which can be utilized efficiently to decreases the cost.

Chapter 2 evaluates the effects of gas macromixing in the cathode gas channel and GDL in order to explain the different cell performance of PEFC with parallel and serpentine flow fields. The concept of residence time distribution (RTD) is applied to PEFC, and the reactor compartment model is presented according to the RTD characters by using CFD technique. The cell performance difference of various flow fields and space times measured by experiment thus can be explained by 1 parameter. The optimal gas channel can be also suggested according to the specific ORR behavior.

Chapter 3 furtherly demonstrates the effects and detailed mechanisms of mass transfer in the cathode partially narrowed flow fields. By comparing the conventional parallel flow fields and partially narrowed flow fields with various shapes by experiment and numerical simulation, the effects of through-plane and in-plane gas flows, *i.e.*, diving flow and cross flow, are discussed respectively. The unique phenomenon in the partially narrowed flow fields was observed, which is seldom mentioned in the literature. The relative magnitude of mass convection and diffusion inside GDL is also investigated to evaluate the effects of cross flow.

Chapter 4 explores the effects of gas flow direction, *i.e.*, co-flow and counterflow, and the requirement of hydrogen one-pass conversion in the PEFC system with hydrogen recirculation to maximize the cell performance, from the viewpoints of process-scale water management. The water transport by different mechanism is investigated in the cell which is regarded as an ideal flow reactor. The CL dimensionless model is applied to demonstrate the competition of ORR and mass transport at different humidifying conditions.

Conclusions (the last chapter) summarizes the general conclusions drawn from the previous chapters. The contribution of this research for the large-scale commercialization of PEFCs is described. In addition, the future works and the possibility of the methods mentioned in this dissertation are also discussed.

0.4 Abbreviations

ACL   Anode catalyst layer

BP   Bipolar plate

CB	Carbon black
CL	Catalyst layer
CCL	Cathode catalyst layer
CFD	Computational fluid dynamics
EMF	Electromotive force
FCV	Fuel cell vehicle
GDL	Gas diffusion layer
HOR	Hydrogen oxidation reaction
MEA	Membrane electrode assembly
MPL	Microporous layer
ORR	Oxygen reduction reaction
PEFC	Tafel slope
PEM	Proton exchange membrane
RH	Relative humidity
RTD	Residence time distribution

0.5 References

[1] Our World in Data <https://ourworldindata.org/global-energy-200-years> (2022.11.15).

[2] Our World in Data <https://ourworldindata.org/grapher/years-of-fossil-fuel-reserves-left> (2022.11.15).

[3] National Oceanic and Atmospheric Administration (NOAA) <https://climate.nasa.gov/vital-signs/carbon-dioxide/> (2022.11.15).

[4] NASA's Goddard Space Flight Center <https://climate.nasa.gov/vital-signs/sea-level/> (2022.11.15).

[5] Y. Haseli, *Int. J. Hydrog. Energy*, **43**, 9015–9021 (2018).

[6] L. Giorgi, and F. Leccese, *The Open Fuel Cells Journal*, **6**, 1–20 (2013).

[7] EG&G Technical Services, Inc., *Fuel Cell Handbook (7th Edition)* (2004).

[8] P. Agnolucci, *Int. J. Hydrog. Energy*, **32**, 4319–4328 (2007).

[9] T. Yoshizumi, H. Kubo, and M. Okumura, *SAE Tech. Pap.*, 2021-01-0740 (2021).

[10] M. K. Debe, *Nature*, **486**, 43–51 (2012).

[11] J. X. Wang, T. E. Springer and R. R. Adzic, *J. Electrochem. Soc.*, **153**, A1732–A1740 (2006).

[12] K. Jiao, J. Xuan, Q. Du, Z. Bao, B. Xie, B. Wang, Y. Zhao, L. Fan, H. Wang, Z. Hou, S. Huo, N. P. Brandon, Y. Yin, and M. D. Guiver, *Nature*, **595**, 361–369 (2021).

[13] A. Kongkanand, and M.F. Mathias, *J. Phys. Chem. Lett.*, **7**, 1127–1137 (2016).

[14] J. Marcinkoski, J. Spendelow, A. Wilson, and D. Papageorgopoulos, Fuel Cell System Cost–2015, US DOE (2015).

[15] K. Karan, *Curr. Opin. Electrochem.*, **5**, 27–35 (2017).

[16] A. Aiyejina and M. K. S. Sastry, *J. Fueal Cell Sci. Technol.*, **9**, 011011 (2012).

[17] Y. Qi, X. Li, S. Li, T. Li, M. Espinoza-Andaluz, P. Tunestål, and M. Andersson, *Int. J. Energy Res.*, **44**, 4352–4365 (2020).

[18] F. Akitomo, T. Sasabe, T. Yoshida, H. Naito, K. Kawamura, and S. Hirai, *J. Pow. Sour.*, **431**, 205–209 (2019).

[19] K. Takanohashi, T. Suga, M. Uchida, T. Ueda, Y. Nagumo, J. Inukai, H. Nishide, and M. Watanabe, *J. Pow. Sour.*, **343**, 135–141 (2017).

[20] H. Nakajima, and K. Matsutani, *ECS Trans.*, **64**(3), 763–769 (2014).

[21] H. Wu, *Appl. Energy*, **165**, 81 (2016).

[22] K. Nishida, R. Nakauchi, Y. Maeda, T. Umekawa, and M. Kawasaki, *ECS Trans.*, **80** (8), 527–534 (2017).

[23] C. Chan, N. Zamel, X. Li, and J. Shen, *Electrochim. Acta*, **65**(30), 13–21 (2012).

[24] Y. Kakizawa, T. Kobayashi, M. Uchida, T. Ohno, T. Suga, M. Teranishi, M. Oneda, T. Saiki, H. Nishide, M. Watanabe, A. Iiyama, and J. Inukai, *J. Surf. Finish. Soc. Jpn*, **72**, 230–237 (2021).

[25] W. K. Epting, and S. Litster, *Int. J. Heat Mass Transf.*, **306**, 674–684 (2016).

[26] O. Panchenko, E. Borgardt, W. Zwaygardt, F. J. Hackemüller, M. Bram, N. Kardjilov, T. Arlt, I. Manke, M. Müller, D. Stolten, and W. Lehnert, *J. Pow. Sour.*, **390**, 108–115 (2018).

[27] K. Nishida, R.Funaok, T. Furukawa, and Y. Kono, *ECS Trans.*, **98** (9), 89–96 (2020).

[28] E. Caradea, I. Stefanescu, R. E. Ionete, H. Ene, D. B. Ingham, and L. Ma, *Int. J. Mulyiphys.*, **2**, 313–326 (2008).

[29] L. Wang, A. Husar, T. Zhou, and H. Liu, *Int. J. Hydrog. Energy*, **28**, 1263 (2003)

[30] D. Cheddie, and N. Munroe, *J. Pow. Sour.*, **147**, 72–84 (2005).

[31] Y. Chen, O. L. Enearu, D. Montalvao, and T. Sutharssan, *J. Appl. Mech. Eng.*, **5**, 1000241 (2016).

[32] L. M. Pant, M. R. Gerhardt, N. Macauley, R. Mukundan, R. L. Borup, and A. Z. Weber, *Electrochim. Acta*, **326**, 134963 (2019).

[33] M. Sauermoser, N. Kizilova, B. G. Pollet, and S. Kjelstrup, *Front. Energy Res*, **8**, 525 (2020).

[34] X. Li, and I. Sabir, *Int. J. Hydrog. Energy*, **30**, 359 (2005).

[35] M. Z. Chowdhury, O. Genc, and S. Toros, *Int. J. Hydrog. Energy*, **43**, 10798 (2018).

[36] H. Kahraman, and M.F. Orhan, *Energy Convers. Manag.*, **133**, 363 (2017).

[37] T. Wilberforce, Z.E. Hassan, E. Ogungbemi, O. Ijaodola, F. N. Khatib, A. Durrant, J. Thompsom, A. Baroutaji, and A.G. Olabi, *Renew. Sust. Energy*, **111**, 236 (2019).

[38] J.H. Nam, K.J. Lee, S. Sohn, and C.J. Kim, *J. Pow. Sour.*, **188**, 14 (2009).

[39] D.H. Jeon, S. Greenway, S. Shimpalee, and J.W. Van Zee, *Int. J. Hydrog. Energy*, **33**, 1052 (2008).

[40] X. Wang, Y. Duan, W. Yan, and X. Peng, *Electrochim. Acta*, **53**, 5334 (2008).

[41] A. Arvay, J. French, J.C. Wang, X.H. Peng, and A.M. Kannan, *Int. J. Hydrog. Energy*, **38**, 3717 (2013).

[42] D. Spernjak, A.K. Prasad, and S.G. Advani, *J. Pow. Sour.*, **195**, 3553 (2010).

[43] A. D. Santamaria, M. K. Bection, N. J. Cooper, A. Z. Weber, and J. W. Park, *J. Pow. Sour.*, **293**, 162 (2015).

[44] L. Dubau, L. Castanheira, F. Maillard, M. Chatenet, O. Lottin, G. Maranzana, J. Dillet, A. Lamibrac, J.C. Perrin, E. Moukheiber, A. ElKaddouri, G.D. Moor, C. Bas, L. Flandin, and N. Caqué, *WIREs Energy Environ.*, **3**, 540 (2014).

[45] M. Bilgili, M. Bosomoiu, and G. Tsotridis, *Int. J. Hydrog. Energy*, **40**, 2303 (2015).

[46] A. Ghanbarian, and M. J. Kermani, *Energy Convers. Manag.*, **110**, 356 (2016).

[47] W. Li, W. Yang, N. Wang, Y. Jiao, Y. Yang, and Z. Qu, *Int. J. Hydrog. Energy*, **45**, 17759 (2020).

[48] H. Heidary, M. J. Kermani, and B. Dabir, *Energy Convers. Manag.*, **124**, 51 (2016).

[49] Y. Cai, J. Sun, F. Wei, and B. Chen, *Energies*, **15**, 3812 (2022).

[50] H. Guo, H. Chen, F. Ye, and C. F. Ma, *Int. J. Energy Res.*, **43**, 2737 (2019).

[51] P. Dong, G. Xie, and M. Ni, *Energy*, **206**, 117977 (2020).

[52] Y. Yin, S. Wu, Y. Qin, O. N. Otoo, and J. Zhang, *Appl. Energy*, **271**, 115257 (2020).

[53] Y. Cai, D. Wu, J. Sun, and B. Chen, *Energy*, **222**, 119951 (2021).

[54] X. Wang, Y. Qin, S. Wu, X. Shangguan, J. Zhang, and Y. Yin, *J. Pow. Sour.*, **457**, 228034 (2020).

[55] J. Shen, L. Zeng, Z. Liu, and W. Liu, *Int. J. Heat Mass Transf.*, **55**, 811 (2019).

[56] X. Zhang, X. Ma, F. Xi, X. Zhu, and S. Shuai, *Int. J. Heat Mass Transf.*, **191**, 122766 (2022).

[57] J. Supra, H. Janben, W. Lahnert, and D. Stolten, *Int. J. Hydrog. Energy*, **38**, 1943–1951 (2013).

[58] F. Urbani, O. Barbera, G. Giacoppo, G. Squadrito, and E. Passalacqua, *Int. J. Hydrog. Energy*, **33**, 3137–3141 (2008).

[59] S. Enz, T. A. Dao, M. Messerschmidt, and J. Scholta, *J. Pow. Sour.*, **274**, 521–535 (2015).

[60] M. Ji, and Z. Wei, *Energies*, **2**, 1057–1106 (2009).

[61] H. Meng, and C. Y. Wang, *J. Electrochem. Soc.*, **152**(9), A1733–A1741 (2005).

[62] H. Li, Y. H. Tang, Z. W. Wang, Z. Shi, S. H. Wu, D. T. Song, J. L. Zhang, K. Fatih, J. J. Zhang, H. J. Wang, Z. S. Liu, R. Abouatallah, and A. Mazza, *J. Pow. Sour.*, **178**, 103–117 (2008).

[63] J. St-Pierre, D. P. Wilkinson, S. Knights, and M. Bos, *J. New Mater. Electrochem. Syst.* **3**, 99–106 (2000).

[64] Y. A. Gandomo, M. D. Edmundson, F. C. Busby, and M. M. Mench, *J. Elelctrochem. Soc.*, **163**, F933 (2016).

[65] T. Kitahara, H. Nakajima, and K. Mori, *J. Pow. Sour.*, **199**, 29–36 (2012).

[66] M. Kawase, K. Sato, R. Mitsui, H. Asonuma, M. Kageyama, K. Yamaguchi, and G. Inoue, *AIChE J.*, **63**(1), 249–256 (2017).

Chapter 1

Analysis of ORR Kinetics and Mass Transport from Catalytic Pt-Loading Dependency

1.1 Introduction

The cost of the Pt in the CL is the one of the main issues addressing in the PEFCs' wider commercialization. While the endeavor of (1) exploring the new material of the catalyst[1], (2) modifying the catalyst structure[2] and (3) boosting ionomer performance[3] have been processing in recent years, the improvement of catalyst efficiency with minimum Pt utilization at the MEA and stack scales is also a considerable strategy.[4] In the other words, the utilization of the catalyst should be minimized while the activity is sufficiently employed, which requires the enhancement of mass transfer.

   As mentioned in the previous chapter, the phenomenon in the PEFC is complicated. The ORR of the CCL acts as the limit step of processes in the PEFC, which is paid much attention in the literature. Although many studies have been proceeded in characterization and modeling of the CCL,[5, 6] a simple but effective model which is suitable for cell-level design is lack of report, and the evaluation and prediction of the CCL performance in a comprehensive model proven experimentally has been remained as an issue.

   The purpose in this chapter is to analyze the Pt-loading dependency of the catalyst activity and to derive the intrinsic ORR kinetics without mass transport resistance. The CCL dimensionless model[7] is helpful to demonstrate the relative rate of reaction and mass transfer by expressing of the dimensionless moduli, in the perspective of chemical engineering.

1.2 Theory

1.2.1 Formula of ORR rate

The ORR rate has been experimentally proven to be the first order reaction to the oxygen partial pressure[8], and the emf dependency follows the Tafel's equation, when the reverse reaction of ORR is not remarkable. Therefore, the ORR rate per unit volume of the CCL r_{vc} can be expressed as Eq. (1.1),[8]

$$r_{vc} = k_{vc}^{\oplus} \exp(-E_c/b_c)\, p_O \tag{1.1}$$

where E_c is the cathode emf, *i.e.*, potential difference at interfaces between electron and proton [V], $k_{vc}^{\oplus}$ is the reaction rate constant per unit volume of CCL [mol/(Pa·m³·s)] at $E_c = 0$, b_c is the Tafel slope [V] and p_O is the oxygen partial pressure [Pa]. The cathode emf is the potential difference between the electron and the proton. The ORR rate is the function of the location in the CCL, instead of a constant, due to the distributions of oxygen partial pressure and emf. The ORR rate constant is also the function Pt-loading, which can be regarded to have the linear relationship with the later, since the active area was experimentally proven to be proportional to the Pt-loading.[9] Then the ORR rate constant can be written in Pt-mass-based form as Eq. (1.2),

$$k_{vc}^{\oplus} = k_{mc}^{\oplus}\rho_b \tag{1.2}$$

where $k_{mc}^{\oplus}$ is the reaction rate constant per unit mass of Pt [mol/(Pa·s·kg-Pt)] at $E_c = 0$, ρ_b is Pt mass per unit volume of CCL [kg-Pt/m³-CCL]. Additionally, the Pt-loading is assumed to distribute evenly in the CCL.

Based on the ORR rate formula mentioned above, the distributions of ORR reaction rate, oxygen partial pressure and electrical potential can be solved according to the CCL dimensionless model.

1.2.2 CCL dimensionless model

The isothermal field is assumed in the CCL dimensionless model which provides the reaction rate profile in the CCL thickness direction at a point in the gas channel. In this model, the anode HOR loss is neglected, and all of the IR is assumed to be attributed in the PEM, so that the emf at CCL–PEM boundary equals to IR-corrected cell voltage. Therefore, the CCL-volume-based reaction rate constant at the CCL-PEM boundary k_{vcm} can be written as Eq. (1.3).

$$k_{vcm} = k_{mc}^{\oplus}\, \rho_b \exp(-E_{cm}/b_c) \tag{1.3}$$

The current generates in the CCL, which is equative to the integration of the electron generates rate in the CCL thickness direction. The current density i [A/m^2] thus can be calculated by Eq. (1.4),

$$i = 4F \int_0^\delta r_{vc} dz = 4F\delta k_{vcm} p_{Oc} F_e \tag{1.4}$$

where δ is the thickness of CCL [m], p_{Oc} is the oxygen partial pressure at CCL- GDL boundary [Pa], F_e is the effectiveness factor [-], *i.e.*, the ratio of the observed ORR rate to the ORR rate without any transport resistances. The subscript m denotes the PEM–CCL boundary and the subscript c denotes the CCL–GDL boundary. When F_e equals to 1, the ORR occurs without transport resistance, so that the k_{vc} and the p_O are a constant in the CCL thickness direction. Increase in mass transport resistance decreases the effectiveness factor, and the k_{vcm} and the p_{Oc} are the greatest in the CCL. The effectiveness factor can be solved by the CCL dimensionless model, and 4 dimensionless moduli are required: (1) Thiele modulus at the PEM–CCL boundary M_{Om}, (2) our proposed dimensionless modulus M_{pm}, (3) Péclet number at the PEM–CCL boundary P_{Om} and (4) oxygen mole fraction at the CCL–GDL boundary y_{Oc}. The dimensionless moduli (1) – (3) are defined as below.

$$M_{Om} = \delta \sqrt{\frac{k_{vcm}RT}{D_{eO}}} \tag{1.5}$$

$$M_{pm} = \delta \sqrt{\frac{4F k_{vcm} p_{Oc}}{\sigma_{ep} b_c}} \tag{1.6}$$

$$P_{Om} = \frac{\delta N_{gm}}{C_g D_{eO}} \tag{1.7}$$

where D_{eO} is the effective oxygen diffusion coefficient [m^2/s], σ_{ep} is the effective proton conductivity [S/m], and N_{gm} is the total gas flux at the PEM–CCL boundary [mol/(m^2·s)]. M_{Om} represents a ratio of oxygen diffusion resistance to reaction resistance, and M_{pm} represents a ratio of proton transport resistance to reaction resistance, and P_{Om} represents a ratio of oxygen diffusion resistance to convection resistance. M_{Om} and M_{pm} can be also regarded as the relative rapidness of the reaction to the oxygen or proton transport.

It is assumed that the water only exists in the vapor phase, and the hydrogen, oxygen and nitrogen crossover are 0, so that the water flux permeating through the PEM, $N_A^{(M)}$ [mol/(m^2·s)], equals the total gas flux at PEM–CCL boundary, N_{gm}.

According to the assumptions and theories described above, when y_{Oc} and P_{Om} are fixed or negligibly little, the dimensionless moduli as well as ORR kinetics is possibly

analyzed from experiment by only varying one parameter in CCL thickness δ, oxygen partial pressure p_{Oc}, effective oxygen diffusivity D_{eO}, and ORR rate constant k_{vcm}.[10] In this study, the objective is to analyze the impact of Pt-loading, which directly affects k_{vcm}.

1.2.3 Determination method of dimensionless moduli

When δ and p_{Oc} are fixed, and the properties, e.g., D_{eO} and σ_{ep}, are constants, the F_e, M_{Om} and M_{pm} can be expressed as Eqs. (1.8) – (1.10),

$$F_e = c_{F_e} i / \{\rho_b \exp(-E_{cm}/b_c)\} \tag{1.8}$$

$$M_{Om} = c_{M_O} \rho_b^{0.5} \exp(-E_{cm}/2b_c) \tag{1.9}$$

$$M_{pm} = c_{M_p} \rho_b^{0.5} \exp(-E_{cm}/2b_c) \tag{1.10}$$

where c_{Fe}, c_{MO} and c_{Mp} are constants, as shown in Eq. (1.11) – (1.13).

$$c_{F_e} = 1/(4Fp_{Oc}\delta k_{mc}^{\oplus}) \tag{1.11}$$

$$c_{M_O} = \delta / \sqrt{k_{mc}^{\oplus} RT/D_{eO}} \tag{1.12}$$

$$c_{M_p} = \delta / \sqrt{4Fp_{Oc}k_{mc}^{\oplus}/(\sigma_{ep}b_c)} \tag{1.13}$$

By varying the Pt-loading, M_{pm}/M_{Om} are constant, and F_e and M_{Om} are linear to i/ρ_b and $\rho_b^{0.5}$ respectively, so that the experimental data can be fitted to the theoretical curves of the relationship between F_e and M_{Om}, as shown in Fig. 1.1. On the other hand, when the dimensionless moduli are obtained, the properties, e.g., D_{eO} and σ_{ep}, can be also determined.

The algorithm is shown in Fig. 1.1. First of all, the constants c_{Fe}, c_{MO} and c_{Mp} should be assumed, so that the effectiveness factor and dimensionless moduli can be also derived from experimental data of current density and IR-corrected cell voltage from Eqs. (1.8) – (1.10). Then, the effectiveness factor can be theoretically solved by the CCL dimensionless model in cases of different Pt-loading. Next, the error of experimental and calculated effectiveness factor summed by all of the cases can be derived, and this error should be in a tolerance range. The error is evaluated by Eq. (1.14). If the error is larger than the tolerance, the constants c_{Fe}, c_{MO} and c_{Mp} should be assumed and the calculation should be processed again, until the error is small enough. However, several solutions may exist where the error is near but no equal to 0, due to the usually existing experimental data. Therefore, the optimal solution can be offered by minimizing the error. Finally, the effectiveness factors and dimensionless moduli, as well as the dimensioned properties, can be obtained.

$$\varepsilon = \sum_j \left(\log F_{e,j} - \log F_{e,j}^{\text{theo.}}\right)^2 \tag{1.14}$$
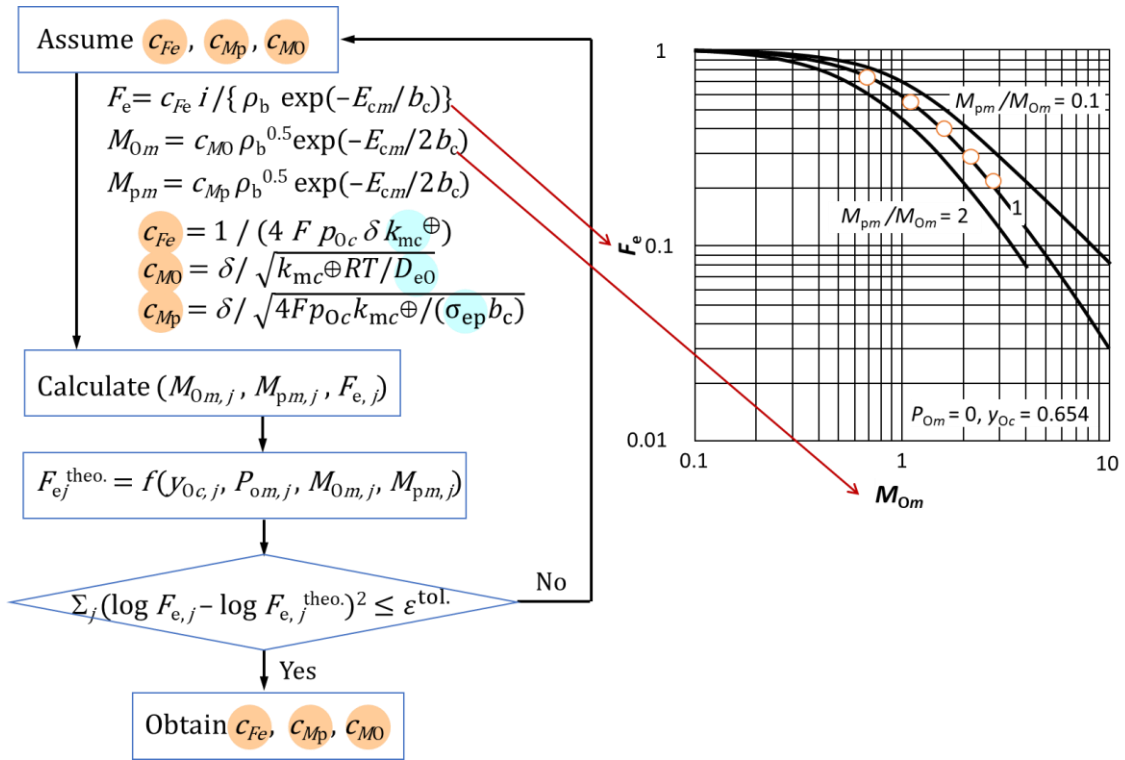
Figure 1.1: Algorithm of Pt-loading dependency analysis

1.3 Experimental

A Japan Automobile Research Institute (JARI) standard cell with decreased 2.0 cm×2.0 cm active area was applied in the experiment, as shown in Fig. 1.2. The flow channels for both anode and cathode were single serpentine. The width, depth of the channels and the width of the ribs were all 1 mm.

The MEA was consisted of the CL made of 30, 40 and 50 wt% Pt/carbon black catalyst particles with ionomer and the membrane (variation NR-212). Ionomer/carbon weight ratio was 1.0. The Pt-loading density and thickness of CCLs applied in the experiments are shown in Table 1.1.

Table 1.1: CCLs applied in the experiments

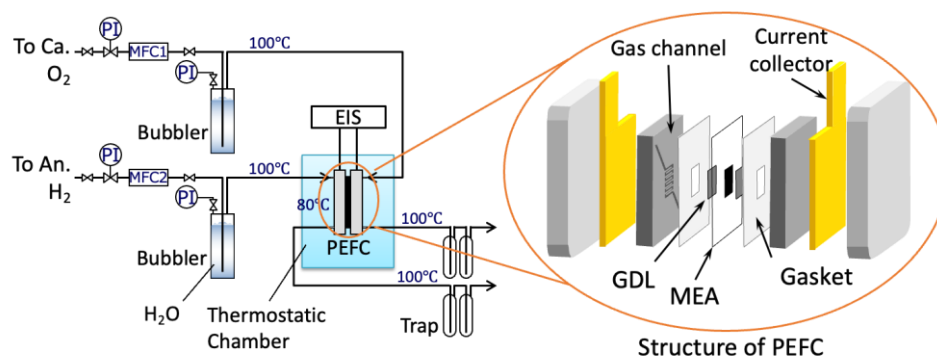| Pt-loading	ρ_b [kg-Pt/m^3-CCL]	δ [μm]
30 wt%	151.7	46.8
40 wt%	224.1	46.4
50 wt%	327.0	47.4

Figure 1.2: Experimental device

The GDLs of anode and cathode were Toray TGP-H-060, hydrophobically treated with 10 wt% PTFE. The cell temperature was controlled by a thermostatic chamber at 80 °C., and the back pressure was 1 atm. 600 cm^3/min (20 °C, 1 atm) and 300 cm^3/min (20 °C, 1 atm) O$_2$ were humidified in bubblers at 75 ˚C.

Polarization curves, electrochemical impedance spectra (EIS), and cyclic voltammetry (CV) were measured by electrochemical measurement system (Hokuto Denko Corp., HZ-7000). The polarization curves were measured in potentiostatic mode. The EIS were measured in a range of frequency from 100 mHz to 100 kHz. A standard equivalent circuit model was employed to determine the high frequency resistance (HFR),[11] which was regarded as the ohmic resistance of PEM in this study. The potential of working electrode was scanned between 0.05 V and 0.90 V vs. reversible hydrogen electrode (RHE) in the CV measurement by supplying hydrogen, where the sweeping rate was 50 mV/s. The average electrochemically active surface area (ECSA) calculated by integrating the CV in the hydrogen desorption and absorption regions was applied, where the monolayer hydrogen charge of 210 μC/cm^2-$_{Pt}$ was assumed.[12]

$N_A^{(M)}$ was calculated from the water flow rate of inlet and outlet in anode and cathode according to the water mass balance. The water flow rate of cell outlet was measured by collecting condensed water in the cold traps at the cell outlet for a certain time. By applying PTFE instead of MEA and the water permeation through the MEA thus can be prevented, the result can be regarded as the water flow rate at cell inlet.

1.4 Results and Discussion

1.4.1 Polarization curves

The measured polarization curves of varied Pt-loading, as shown in Fig. 1.3(a), which indicates that the greater Pt-loading provide better cell performance. However, the CCL
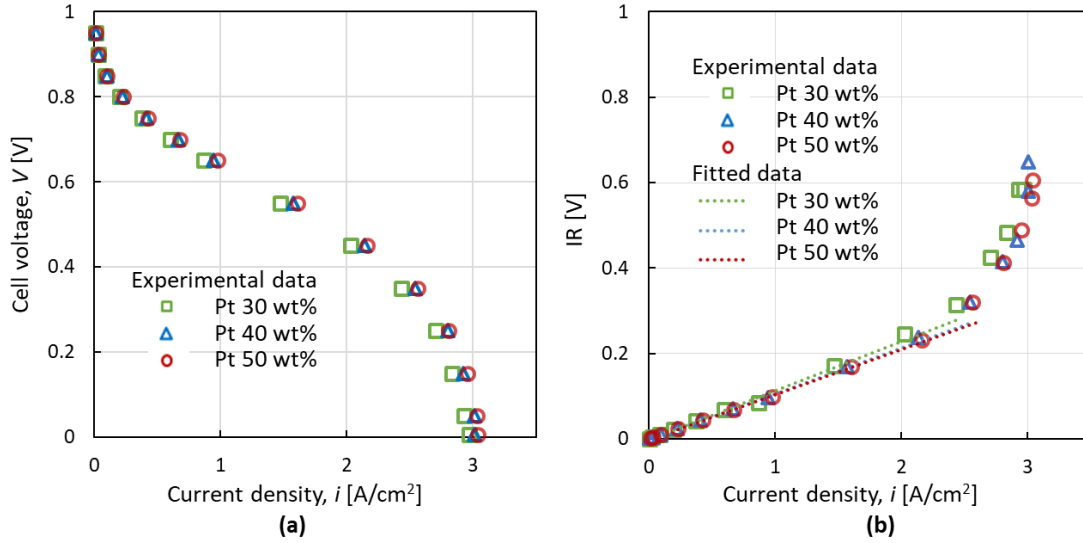
24

Figure 1.3: Polarization curves (a) and IR (a)

with 40 wt% Pt-loading has nearly the same cell performance as that with 50 wt% Pt-loading. Fig. 1.3(b) demonstrates that the relationships of IR and current density in different cases of Pt-loading are nearly the same. The slope of the curves in the low current density regions can be considered as a constant, which indicates that the RH of gas as well as the moisture content of PEM are almost constants, due to the low reactant conversion. When the current density is 2 A/cm^2, the oxygen conversion is 0.10 which equals to that of hydrogen, so that the proton conductivities of PEM and ionomer can be regarded as constants. On the other hand, the slope of IR increases in the high current density region, which may origin from the increased cell temperature. In addition, the approximate slopes less than $i = 2$ A/cm^2 in Fig. 1.3(b) were regarded as the ohmic loss which were applied to correct the cell voltage.

1.4.2 Determination of dimensionless moduli and ORR kinetics

Determination of dimensionless moduli. 9 experimental points shown in Fig. 1.5 were applied to determine the dimensionless moduli by the method mentioned in section 1.2.3. Tafel slope $b_c = 0.0346$ V applied in the calculation was obtained from the experiment by using Pt-sputtering catalyst for the analysis.[10, 13] y_{Oc} was calculated from the average of cell inlet and outlet, which is available based on the low conversion, so that the distribution of the oxygen concentration in the in-plane direction and the oxygen concentration decrease through the GDL can be ignored.

Fig. 1.4 shows the error of experimental and theoretical data in a range of assumed M_{Om} and M_{pm}/M_{Om} of the first experimental point. The calculation results indicate that the error is small enough when the $M_{Om} = 0.300$ in case of 30 wt% Pt-loading at $E_{cm} = 0.80$ V,
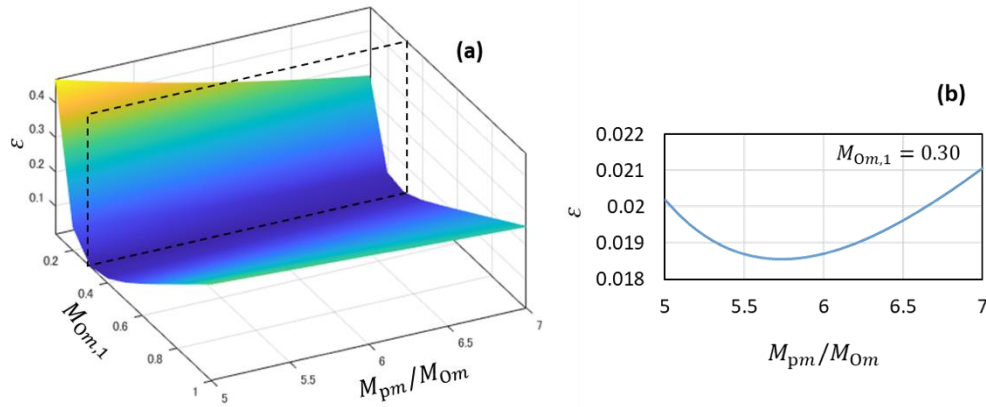
Figure 1.4: Error of experimental and theoretical data at different assumed dimensionless moduli
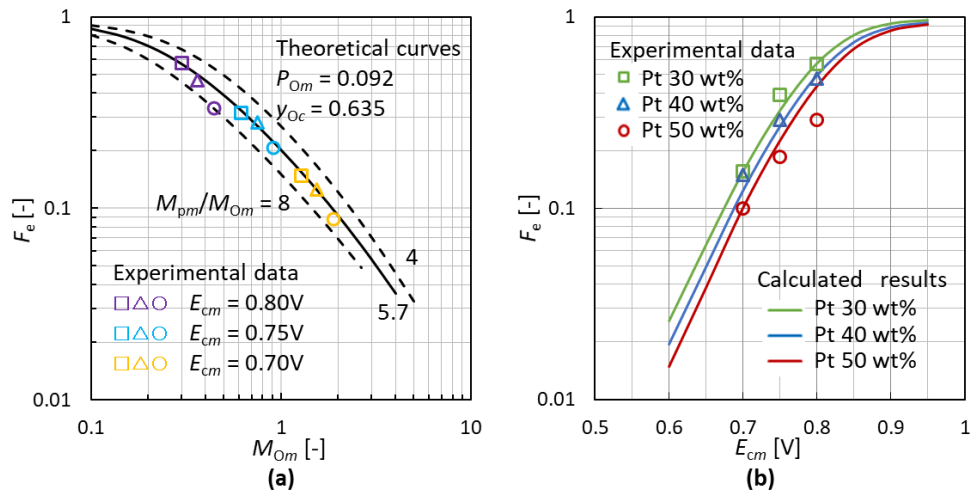

Figure 1.5: Comparison of experimental and theoretical effectiveness factors at different (a) M_{Om} and (b) IR-corrected cell voltage

which can be considered as the solution as shown in Fig. 1.5(a). On the other hand, although M_{pm}/M_{Om} varies in a small range as shown in Fig. 1.5(b), which may be affected by the experimental data, the optimal solution at $M_{pm}/M_{Om} = 5.7$ can be obtained. The determined dimensionless moduli of 9 experimental points are shown in Table 1.2.

The differences of experimental and theoretical effectiveness factor, which contribute the error obtained from Eq. (1.11), are shown in Fig. 1.5. The results indicate that the relatively large experimental error may occur in case of 50 wt% Pt-loading at $E_{cm} = 0.80$ V. It should be noted that each effectiveness factor F_e of experimental points was calculated from the actual P_{Om} and y_{Oc} respectively, and the theoretical curves were calculated at identical P_{Om} and y_{Oc}. On the other hand, according to the results shown in Table 1.2, P_{Om} and y_{Oc} only varied in a small range, so that the sensitivity of these 2 parameters on F_e are not remarkable.[10]

Table 1.2: Determined dimensionless moduli

E_{cm} [V]	Pt-loading	M_{Om} [-]	M_{pm} [-]	P_{Om} [-]	y_{Oc} [-]	$F_e^{theo.}$ [-]
	30 wt%	0.300	1.710	0.079	0.662	0.571
0.80	40 wt%	0.365	2.078	0.083	0.660	0.500
	50 wt%	0.440	2.511	0.087	0.659	0.433
	30 wt%	0.619	3.526	0.095	0.649	0.324
0.75	40 wt%	0.752	4.285	0.101	0.642	0.269
	50 wt%	0.908	5.176	0.170	0.634	0.217
	30 wt%	1.275	7.269	0.141	0.625	0.153
0.70	40 wt%	1.550	8.836	0.454	0.591	0.109
	50 wt%	1.872	10.673	0.486	0.588	0.086

Table 1.3: Determined dimensioned properties

b_c [V][10]	$k_{mc}\oplus$ [mol/(Pa·s·kg-Pt)]	D_{eO} [m²/s]	σ_{ep} [S/m]
0.0346	3.42×10^5	3.27×10^{-7}	2.52

Determination of ORR kinetics and dimensioned properties. The dimensioned properties derived from the dimensionless moduli are shown in Table 1.3. The literature value[14] of D_{eO} is 7.2×10^{-7} m²/s, which is larger than the result in this study. The literature value[15] of σ_{ep} is 0.8–1.9 S/m, which is smaller than the result in this study. In order to obtain the accurate results, more precise experimental condition, especially the humidification, should be improved in this study. In addition, since the oxygen transport resistance in ionomer was not considered in the model, the obtained value of ORR rate constant $k_{mc}\oplus$ contains this transport resistance, so that the ORR rate constant derived by the model is smaller than the real value.

1.4.3 Effects of Pt-loading

The Pt-loading directly affects the electrochemical active area, which is assumed to be linear to k_{vcm} in this study. Fig. 1.6 shows the CV measurement under different Pt-loading conditions. The result shows that the ECSA [m²-Pt] can be regarded as a linear function of the Pt-loading regardless of the CCL thickness variation, which indicates that the particle sizes can be regarded as constants and no agglomerates are formed in the present situations[16]. It also implies that k_{vcm} is a linear function of the ECSA is cases of the uniform distributed Pt in the CCL, so that Eq. (1.6) is applicable.

However, the current density at fixed IR-corrected cell voltage is not linear to the Pt-loading, and the reason can be attributed to the mass transport resistances. Fig. 1.7 shows
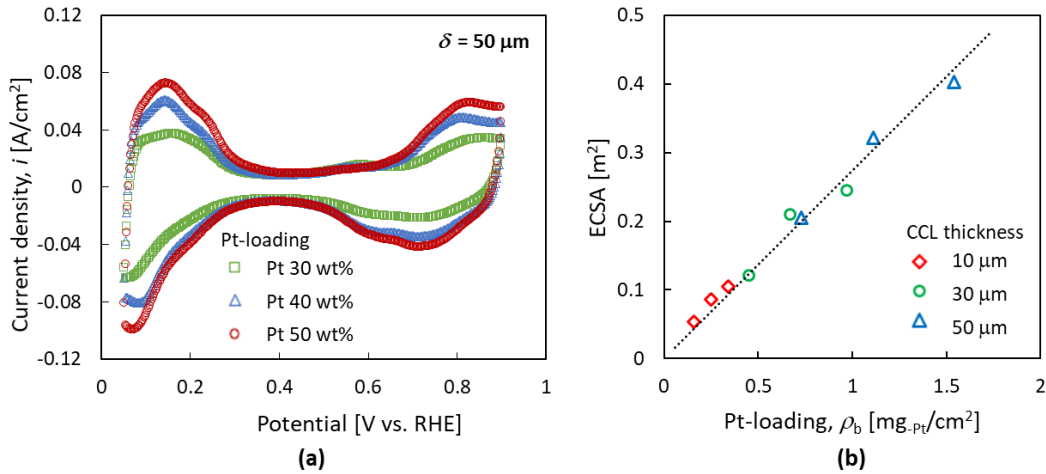
Figure 1.6: Cyclic voltammetry measurement (a) and impact of Pt-loading on electrochemical surface area (b) (electrolyte: Dupont NR-115, temperature: 80 °C, RH: 100%)
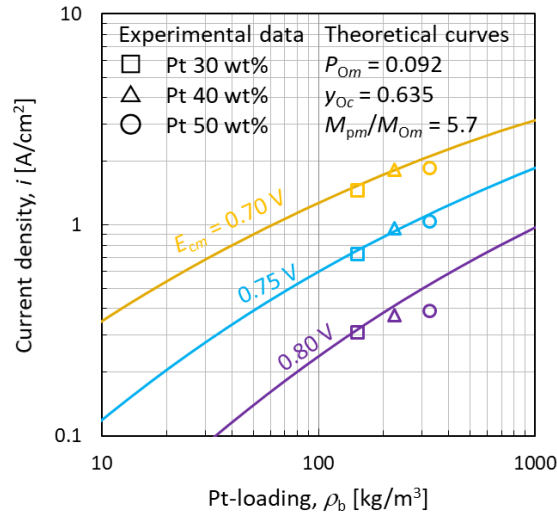

Figure 1.7: Pt-loading dependency of current density at fixed IR-corrected cell voltage

the impact of the Pt-loading on the current density at fixed IR-corrected cell voltage. The theoretical curves demonstrate that the current density increases in a gradually decreased acceleration as the Pt-loading increasing, which indicates that the high Pt-loading results in ineffective Pt utilization. Although higher Pt-loading CCL provides higher current density at an identical IR-corrected cell voltage, the relative mass transport resistances, $i.e.$, M_{Om} and M_{pm}, increase, therefore the effectiveness factor decreases, as shown in Fig. 1.5(a).

In addition, according to the analysis, M_{Om} is much smaller than M_{pm}, which indicates that the oxygen transport is not a main concern under the presented experimental conditions. On the other hand, the proton transport resistance is more remarkable, so that the proton transport is the limit step and should be improved.

The model well quantitively reproduces the effects of Pt-loading on the cell performance, as shown in Fig. 1.7. It should be noted that the experimental data exhibits that the current density of 50 w% Pt-loading is smaller than the theoretical value. The reason may be the that the unexpectedly worse humidification occurred in case of 50 wt% Pt-loading.

1.4.4 Model evaluation

The polarization curves recalculated by the CCL dimensionless model and Tafel equation are shown in Fig. 1.8, in which D_{eO} and σ_{ep} were applied from Table 1.3. Tafel equation provides a good agreement when the current density is lower than 0.2 A/cm^2. When the oxygen conversion is lower than 0.01, and the effectiveness factor approaches 1 in this region, as shown in Fig. 1.8, so that the mass transport resistance is not obvious, and the ORR reaction is the limit step.

The CCL dimensionless model precisely reproduced the experimental data when the current density is between 0.2 and 2.0 A/cm^2, *i.e.*, the oxygen conversion is between 0.01 and 0.10.

The deviation of the experiment and dimensionless model over 2 A/cm^2 may originate from the non-uniform distributions of physiochemical properties. In the high oxygen conversion region, the distributions of gas composition and dimensioned properties cannot be regarded as constants, so that the distributions of dimensionless moduli should be considered. In addition, the flooding may occur in this region, which results in the worse cell performance than the model estimation.
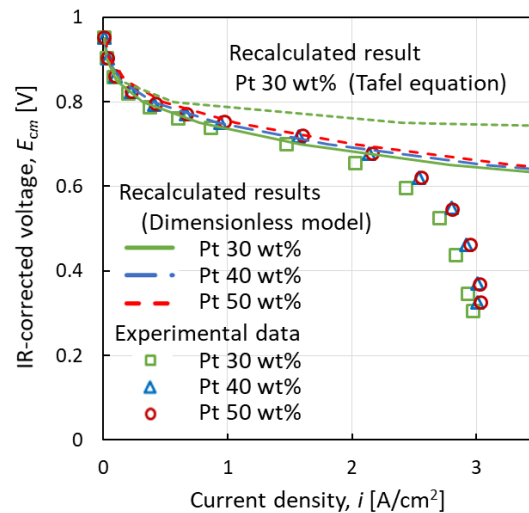

Figure 1.8: Polarization curve of experiment and calculation

1.5 Conclusion

This chapter described the method of determination of intrinsic ORR kinetics, effective oxygen diffusivity and proton conductivity from the Pt-loading dependency by the isothermal CCL dimensionless model. The determined dimensioned properties have good agreement with the literature values. Even though the effective oxygen diffusivity may be underestimated since the oxygen transport resistances in the CCL void and ionomer could not be separated, the oxygen transport resistance is not a main concern comparing to the proton transport. More accurate experimental data is required for the analysis in this model.

The effects of Pt-loading on the cell performance and relative rates among ORR, oxygen transport and proton transport were also quantitively described by the model. The higher Pt-loading offers better cell performance but lower effectiveness factor due to the limitation of the mass transfer, which infers that the Pt cannot be utilized efficiently when the Pt-loading is too high. This model also provides a theoretical basis for optimization of the Pt-loading.

Moreover, the CCL dimensionless model successfully reproduced the experimental data in the oxygen conversion region lower than 0.10, while the Tafel equation is only able to predict the cell performance at the oxygen conversion lower than 0.01, when the mass transport resistance can be ignored. In future work, the effects of the uneven distributions of physicochemical properties should be estimated to predict the phenomenon in the high conversion region.

1.6 Symbols

b_c	Tafel slope	[V]
D_{eO}	Effective oxygen diffusion coefficient in CCL	[m²/s]
E_c	Emf in cathode	[V]
E_{cm}	Emf at CCL-PEM boundary or IR corrected cell voltage	[V]
F	Faraday constant	[C/mol]
$k_{mc}\oplus$	Reaction constant at Emf = 0 per unit platinum mass	[mol/(Pa·kg·s)]
k_{vc}	1st-order cathode reaction rate constant per layer volume	[mol/(Pa·m³·s)]
M_{Om}	Thiele modulus	[-]

$M_{\mathrm{p}m}$	Our modulus	[-]
$N_{\mathrm{A}}^{(\mathrm{M})}$	Water permeation flux through PEM	[mol/(m²·s)]
$N_{\mathrm{g}m}$	Total gas flux at CCL–PEM boundary	[mol/(m²·s)]
$P_{\mathrm{O}m}$	Péclet number	[-]
p_{O}	Partial pressure of oxygen	[Pa]
R	Molar gas constant	[J/(K·mol)]
r_{vc}	ORR rate per unit volume of CCL	[mol/(Pa·m³·s)]
T	Temperature	[K]
V	Cell voltage	[V]
y_{O}	Oxygen mole fraction	[-]
z	Location at MEA thickness direction	[m]

Greeks

ε	Accumulated error between experimental and theoretical data	[-]
δ	Thickness of CCL	[m]
ρ_{b}	Platinum loading per unit layer volume	[kg/m³]
σ_{ep}	Effective proton conductivity	[S/m]

Subscripts

c	CCL–GDL boundary
m	CL–PEM boundary
j	Experimental point

Superscripts

theo.	Theoretical
tol.	Tolerance

1.7 References

[1] K. Karan, *Curr. Opin. Electrochem.*, **5**, 27–35 (2017).

[2] M. Uchida, *Curr. Opin. Electrochem.*, **21**, 209–218 (2020).

[3] G. Inoue, T. Ohnishi, M. So, K. Park, M. Ono, and Y. Tsuge, *J. Pow. Sour.*, **439**, 227060 (2019).

[4] K. Jiao, J. Xuan, Q. Du, Z. Bao, B. Xie, B. Wang, Y. Zhao, L. Fan, H. Wang, Z. Hou, S. Huo, N. P. Brandon, Y. Yin, and M. D. Guiver, *Nature*, **595**, 361–369 (2021).

[5] P. P. Mukherjee, and C. Wang, *J. Pow. Sour.*, **153**, A840 (2006).

[6] Y. Mu, P. He, Z. Gu, Z. Qu, and W. Tao, *Electroch. Acta*, **404**, 139721 (2022).

[7] M. Kawase, K. Sato, R. Mitsui, H. Asonuma, M. Kageyama, K. Yamaguchi, and G. Inoue, *AIChE J.*, **63**(1), 249–256 (2017).

[8] M. Kawase, K. Yamaguchi, M. Kageyama, K. Sato, and G. Inoue, *ECS Trans.*, **75**(14), 147–156 (2016).

[9] Y. Shih, G. V. Sagar, and S. D. Lin, *J. Phys. Chem. C*, **112**, 123–130 (2008).

[10] M. Kageyama, K. Yamaguchi, D. Heggo, Y. Ma, H. Ogawa, and M. Kawase, *ECS Trans.*, **98**(9), 163–175 (2020).

[11] S. Cruz-Manzo, and R. Chen, *J. Electroanal. Chem.*, **694**, 45–55 (2013).

[12] S. Trasatti, and O.A. Petrii, *Pure Appl. Chem.*, **63**, 711 (1991).

[13] K. Murase, Y. Makino, Y. Iijima, K. Yamaguchi, M. Kageyama, and M. Kawase, Preprint of the SCEJ 50th Autumn Meeting (Kagoshima, 2018), EG316 [in Japanese].

[14] Y. Tabe, T. Satake, T. Iiri, T. Hayashi, and T. Chikahisa, *ECS Trans.*, **80**(8), 205–214 (2017).

[15] R. Makharia, M. F. Mathias, and D. R. Baker, *J. Electrochem. Soc.*, **152**(5), A970–977 (2005).

[16] Emiliana Fabbri, Susan Taylor, Annett Rabis, Pieter Levecque, Olaf Conrad, Rüdiger Kötz, and Thomas J. Schmidt, *ChemCatChem*, **6**, 1410–1418 (2014).

Chapter 2

Effects of Gas Macromixing in Flow Channels and GDL

2.1 Introduction

For PEFCs' grand-scale commercialization, as mentioned in the Introduction chapter, their performance, which is determined by the local current density or the ORR rate, should be further improved. The distributions of temperature, total pressure, oxygen partial pressure, relative humidity (RH) affect the ORR rate as well as the mass transport resistance and are dependent on each other. Thus, the effects of a single factor in the cell are complicated and uneasy to be clarified.

The ORR in PEFC is an exothermal reaction, so that the temperature profile exists in a cell in both through-plane and in-plane directions. In the through-plane direction, the temperature at cathode catalyst layer surface is 1−2 K higher than the temperature at gas channel, when the current density is 0.8 A/cm^2 and the cell temperature is 80 ^{o}C[1, 2]. On the other hand, the temperature distribution in the in-plane direction is more ununiform than that in the through-plane direction. The difference of the highest and lowest temperature in the electrode was less than 10 K at 0.8 A/cm^2 in a cell with 50 mm $\times$ 50 mm active area observed by thermograph[3].

The total pressure also has a distribution in a cell due to the pressure drop along the gas channel. The pressure drop of the cell with 14.4 cm^2 active area and serpentine gas channel, whose depth, width, and total length are 1.0 mm, 1.0 mm and about 700.0 mm, is about 0.3 kPa, fed with 200 cm^3/min of N_2 at room temperature under atmospheric pressure[4].

The partial pressure profiles of oxygen and water vapor affect the ORR rate distribution. On the other hand, the ORR can change the composition of the reactant gas, i.e. the molar fraction of oxygen and water vapor, so that the performance can also be affected by reactant conversion[5]. Furthermore, gas flow pattern distributes the reactant gas in the in-plane direction, which also affect the cell performance[6]. Since the pressure gradients and concentration gradients exist in the porous GDL, the reactant gas can cross to the neighboring channels and the gas with different compositions are mixed, so that the gas composition distribution is also affected by the cross-flow phenomenon[7].

The distributions of properties are hard to be measured experimentally and should be analyzed and predicted by numerical methods, which have been discussed extensively in the literature. Although many 3-dimensional, non-isothermal, multi-phase models have been reported[8, 9], most of the models are complicated with heavy computation load, and difficult to separate the effects of fluid dynamic, heat transfer, proton/electron transfer and electrochemical phenomenon. A computationally inexpensive method to summarize and understand the distributions of properties in the cell is lack of reporting. To clarify the effects of gas composition inside the cell, the concept of gas mixing and residence time distribution (RTD) in the perspective of chemical reaction engineering can be helpful.

The objective of this study is to demonstrate a low-computation-load numerical model to evaluate the gas mixing property of gas channel and GDL, and to predict the cell performance. The RTD can be simulated by numerical method, so that the macromixing of gas with different space times can be evaluated. By regarding the PEFC as a reactor, the cell performance can also be predicted according to the reactor model which has similar RTD as the simulation results.

In addition, the cell performance under different space time conditions can be measured experimentally by changing the active area and gas flow rate, so that the gas composition profile can also be evaluated. The results can potentially provide a methodology to understand the gas macromixing in different shape of gas channels, which is helpful for the cell design.

2.2 Numerical Model

In this study, a 3-dimensional computational fluid dynamics (CFD) model was developed to simulate the velocity and pressure fields in the cathode gas channels and GDLs. To get the RTD of the gas channel, the tracer with a special physical property, e.g., concentration, electrical conductivity, temperature, was supplied to the gas inlet continuously from the

initial time. Then the step responses at the gas channel outlet were simulated by solving time-dependent advection equations of the specific physical property. The calculation was achieved by using an open source toolbox OpenFOAM 8, based on finite volume method.

2.2.1 Geometry

The geometries and meshes applied for parallel and serpentine channels in the calculation are shown in Fig. 2.1. The gas flows from the inlets to the outlets through the channel as well as the GDL which was implemented as porous medium. The width and depth of gas channels were 1 mm, and the width of the ribs between the channels was 1 mm. The size of the GDL was 22 mm in X direction, 21 mm in Y direction, and 0.19 mm in Z direction. The direction from the gas channel to the GDL in Z direction was defined as positive, where the original location was at the wall of the gas channel, as shown in Fig. 2.1. The meshes of manifolds in parallel channels, bended part in serpentine channels, and GDLs were denser than that in other parts. The total number of cells applied in simulation was 383 000 for parallel gas channel and 373 000 for serpentine gas channels.

2.2.2 Assumptions

Steady state was assumed. The gas flow was incompressible laminar due to low velocities. Isotropic and homogeneous ideal gas which has uniform temperature, density, and viscosity distributions was assumed. The GDL was regarded as a uniform porous medium. No liquid water condensed in the gas channel.

The tracer which has negligibly small diffusivity in the reactant gas was assumed. In another word, the convection of the tracer is great enough so that the diffusion of the tracer can be ignored.
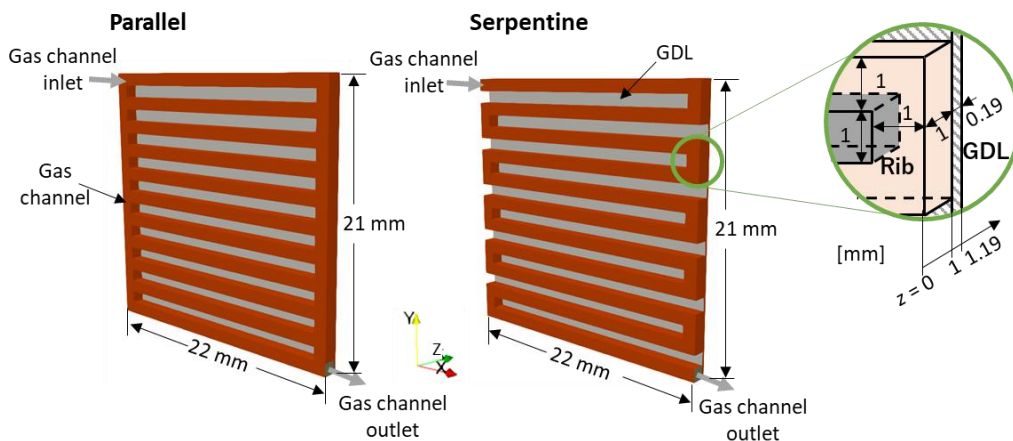

Figure 2.1: Geometries of parallel and serpentine flow fields

2.2.3 CFD simulation

Governing equations applied to calculate the velocity and pressure fields are expressed by Eqs. (2.1) and (2.2).

Mass conservation:

$$\nabla \cdot (\rho \boldsymbol{U}) = 0 \tag{2.1}$$

Momentum conservation:

$$\nabla \cdot (\rho \boldsymbol{U}\boldsymbol{U}) - \nabla \cdot (\mu \nabla \boldsymbol{U}) = -\nabla P + \boldsymbol{S_m} \tag{2.2}$$

where $\boldsymbol{U}$ represents the velocity vector [m/s]. ρ and μ represent the density [kg/m^3] and viscosity [Pa·s] of the reactant gas respectively. P is the total pressure [Pa]. $\boldsymbol{S_m}$ is the momentum source term, which equals $\boldsymbol{0}$ in the gas channels and satisfies the Darcy's law in the GDLs. The anisotropy of the permeability of the GDL is considered, thus $\boldsymbol{S_m}$ in each direction are calculated independently, given by Eq. (2.3).

$$\boldsymbol{S_m} = -(\frac{\mu}{K_x} U_x, \frac{\mu}{K_y} U_y, \frac{\mu}{K_z} U_z) \tag{2.3}$$

where K is the permeability of the GDL [m^2]. The subscripts x, y, z represent the directions.

The operating conditions and physical constants are listed in Table 2.1. The inlet Reynolds number is 127 so that the gas flow can be regarded as laminar.

Table 2.1: Operating conditions and physical constants (353 K)

Variable	Symbol	Value
Total pressure at gas channel outlet	P_L	101325 Pa
Cell temperature	T	353 K
Velocity at gas channel inlet	$|\boldsymbol{U}|$	2.6658 m s^{-1}
Inlet molar fraction of O$_2$	y_{O0}	0.7532
Inlet molar fraction of H$_2$O	y_{S0}	0.2468
Density	ρ	0.9850 kg m^{-3}
Viscosity[10, 11]	μ	2.0675×10^{-5} Pa s
Permeability of GDL (in-plane direction)[12]	K_x, K_y	1.30×10^{-11} m^2
Permeability of GDL (through-plane direction)[12]	K_z	8.99×10^{-12} m^2

2.2.4 RTD simulation

The transport equation of the tracer is given by Eq. (2.4).

$$\frac{\partial \varphi}{\partial t} + \nabla \cdot (\varphi \boldsymbol{U}) - \nabla \cdot (\Gamma \nabla \varphi) = S_\varphi \tag{2.4}$$

where φ represents the specific physical property of the tracer, Γ represents the diffusivity of property [m^2/s], and S_φ represents the source term. U is the velocity field calculated by CFD simulation mentioned above.

In this work, the effect of gas macromixing was focused on, so Γ which describes the diffusion in micro-scope was assumed 0. Since no reaction happens in the gas channels and the GDLs, S_φ equals 0. Thus, the Eq. (2.4) can be simplified to a time-dependent advection equation. For example, when the φ represents the concentration [mol/m^3], the Γ represents the diffusivity [m^2/s], which is neglected, and the tracer is thus assumed to be transferred only by convection.

When setting the φ equals 1 at the vessel inlet and 0 in the whole vessel at the start time, the tracer is carried in the flow field until it fulfills the whole vessel. Then by monitoring the φ at the vessel outlet, the time variation can be described as a cumulative RTD function, $F(t)$.

$$F(t) = \bar{\varphi}_L(t)/\bar{\varphi}_0(0) \tag{2.5}$$

where $\bar{\varphi}$ represents the integrated average value at inlet or outlet face, the subscripts 0 and L represent the gas channel inlet and outlet, respectively. And the RTD function $E(t)$ and the mean residence time $\bar{t}$ can be obtained by Eqs. (2.6) and (2.7).

$$E(t) = \frac{d}{dt}F(t) \tag{2.6}$$

$$\bar{t} = \int_0^\infty tE(t)dt \tag{2.7}$$

2.2.5 Reactor models

The ORR kinetics can be expressed as Eq. (2.8).

$$-r_{SO} = k_{gc}p_O \tag{2.8}$$

where p_O is the local oxygen partial pressure [Pa], and $-r_{SO}$ is the oxygen consumption rate per active area [mol/(m^{2}s)], which was experimentally proved to be 1st-order to the oxygen partial pressure[13]. k_{gc} represents the partial-pressure-based apparent kinetics constant [mol/(Pa·m^2·s)] which is the function of cathode electromotive force and RH at a fixed temperature[14]. k_{gc} is almost linear to the activity of the water vapor a_w which is equal to RH, when the mass transport resistance is not significant, according to our previous studies[15].

By assuming the water permeation flux through the membrane is 0, the oxygen partial pressure and the activity of the water vapor can be calculated from the oxygen conversion x_O and operating conditions by Eqs. (2.9) and (2.10), according to the material balance.

$$p_O = \frac{P y_{O0}(1 - x_O)}{1 + y_{O0}x_O} \tag{2.9}$$

$$a_w = \frac{P}{p_S^{sat}}\frac{y_{S0} + 2y_{O0}x_O}{1 + y_{O0}x_O} \tag{2.10}$$

where y_{S0} and y_{O0} represents the water vapor and oxygen mole fraction of the inlet gas [-], p_S^{sat} represents the saturated water vapor pressure at the cell temperature [Pa], and P is the total pressure in the gas channel [Pa].

When the GDL is thick enough, the continuous oxygen partial pressure and RH distribution on the CL surface can be assumed regardless of the location under gas channels and ribs. Therefore, the PEFC can be regarded as a continuous reactor, which has the gas macromixing behavior between 2 ideal reactor models, *i.e.*, plug flow reactor (PFR) and perfectly mixed flow reactor (CSTR), whose reactor model equations can be written as Eqs. (2.11) and (2.12), respectively.

PFR

$$-r_{SO}d(A/v_0) = C_{O0}dx_O \tag{2.11}$$

CSTR

$$-r_{SO}(A/v_0) = C_{O0}x_O \tag{2.12}$$

where A is the active area from the gas inlet [m^2], v_0 is the inlet gas volumetric flow rate [m^3/s], C_{O0} is the oxygen concentration in the inlet gas [mol/m^3], and x_O is the oxygen conversion [-]. A/v_0 can be regarded as the space time of the reactant gas in the cell. It should be noted that an assumption is made here that the residence time of the reactant gas has a linear relationship with the possibility of reacting on the surface of the catalyst layer. By solving Eqs. (2.8) – (2.10) and the reactor model equations, the distributions of oxygen conversion, as well as the oxygen partial pressure and RH, can be estimated. However, the reactor model for PEFC should be suggested according to the RTD and experiments.

2.3 Experimental

A Japan Automobile Research Institute (JARI) type cell was used in the experiments. The active area was reduced to 2.0 cm×2.0 cm so that the temperature distribution is less ununiform in the in-plane direction. Two kinds of gas channels, *i.e.*, parallel and serpentine as shown in Fig. 2.2, were used in the cell. The width and depth of gas channels
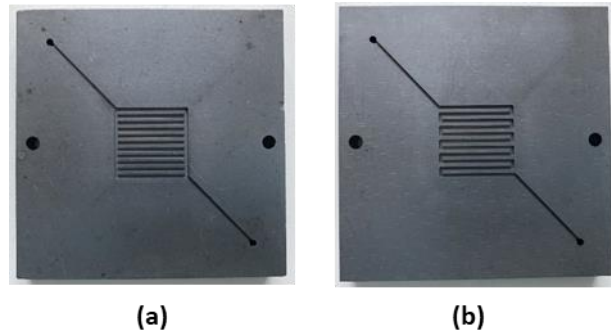
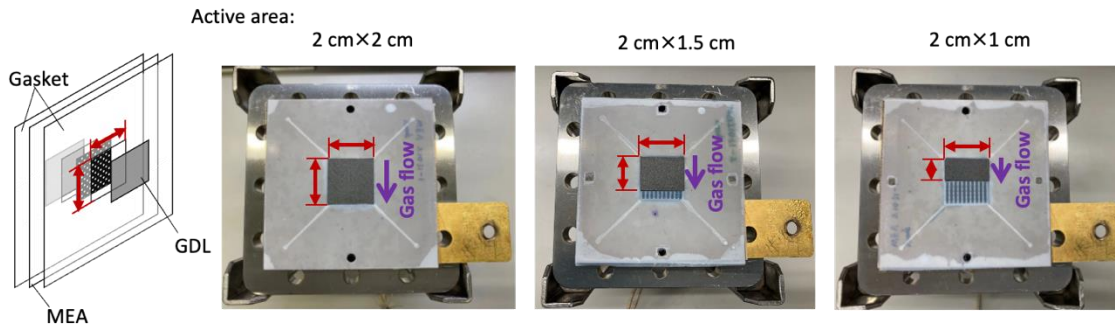Figure 2.2: Gas channels applied in the experiments: (a) parallel, (b) serpentine

Figure 2.3: Different active areas adjusted by the gasket opening

are 1 mm, and the width of the ribs between the channels was 1 mm. The membrane electrode assembly (MEA) was consisted of the catalyst layers made of 50 wt% Pt/carbon black catalyst particles with ionomer and the membrane (Chemours NR-212). Ionomer/carbon weight ratio was 1.0, and the catalyst layers (CL) thicknesses of anode and cathode were 10 μm. Carbon paper (Toray TGP-H-060) without microporous layer (MPL) was used as GDL. The measurement device is shown in the chapter 1.

The MEAs with the same thickness and catalyst of CLs were used in the experiments. On the other hand, the gaskets made of PTFE, which can block the mass transfer and electron conduction, had different opening area to obtain different active areas. The sizes of the gaskets opening were 2.0 cm×2.0 cm, 2.0 cm×1.5 cm, 2.0 cm×1.0 cm, and the GDLs which had the same size of the gaskets opening were utilized in each experiment, as shown in Fig. 2.3. Since the small active areas were applied, the distributions of the temperature and the total pressure in the gas channels were neglected.

The cell was operated in a thermostatic chamber in which the temperature at the center of the cathode gas channel was controlled at 80 °C. The pressure at the cell outlet was 1 atm. Undiluted H_2 and O_2 were humidified in bubblers, which were filled with 65 ˚C water. H_2 flow rate was 60–200 cm^3/min (20 °C, 1 atm) on dry basis. The stoichiometry of H_2/O_2 was 2.

Polarization curves and electrochemical impedance spectra were obtained using an electrochemical measurement system (Hokuto Denko Corp., HZ-7000). The polarization

curves were obtained by measuring the current at each cell voltage (0.005 V – OCV). The impedance spectra were measured in a range of frequency from 100 mHz to 100 kHz. A standard equivalent circuit model was employed to determine the high frequency resistance (HFR)[16]. The cell voltage was corrected by the HFR results.

2.4 Results and Discussion

2.4.1 Derivation of the residence time distribution

The velocity and pressure distributions of parallel and 1-serpentine gas channels simulated by OpenFOAM 8 are shown in Fig. 2.4. As shown in the velocity field in the gas channels ($z = 0.5$ mm, the coordinate refers to Fig. 2.1), since the gas flow is separated into several channels in case of parallel channels, the gas velocity in each channel is much lower than that in serpentine channel, and the pressure gradient of the serpentine channel is much higher than that of parallel channel. As a result, a large amount of gas flows across the rib to the neighbor channel in case of the serpentine channel, especially away from the bended parts where the neighbor gas channels are connected, and nearly no cross-flow gas was found in case of parallel channel as shown in the velocity field in the GDL ($z = 1.095$ mm).
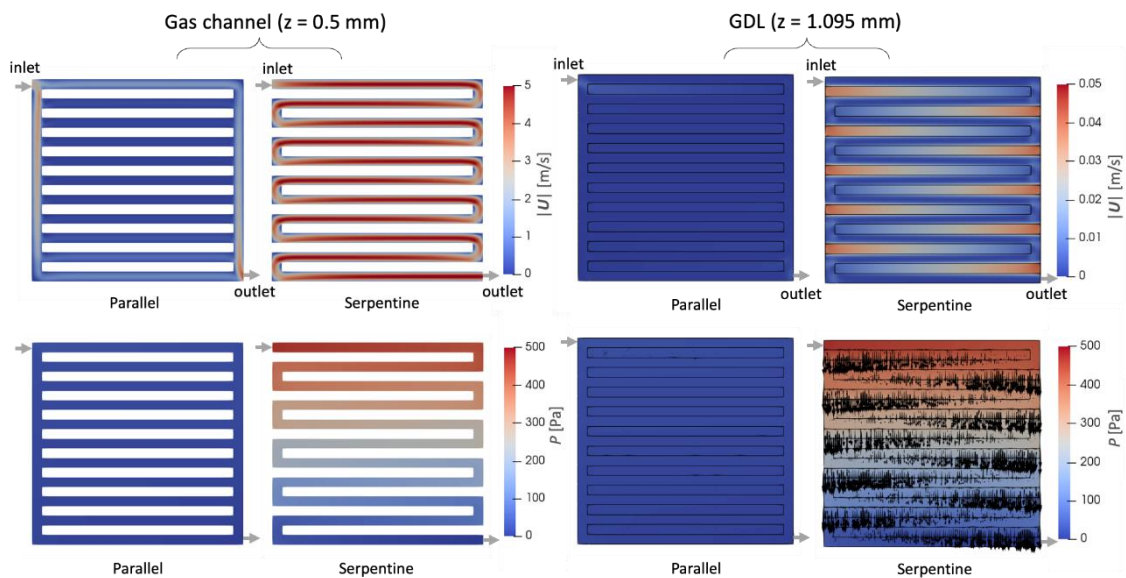

Figure 2.4: Velocity magnitude (top) and pressure (bottom) field in the center sections of gas channels and GDLs (the arrow represents the velocity in the pressure field in the GDL of the serpentine gas channel)
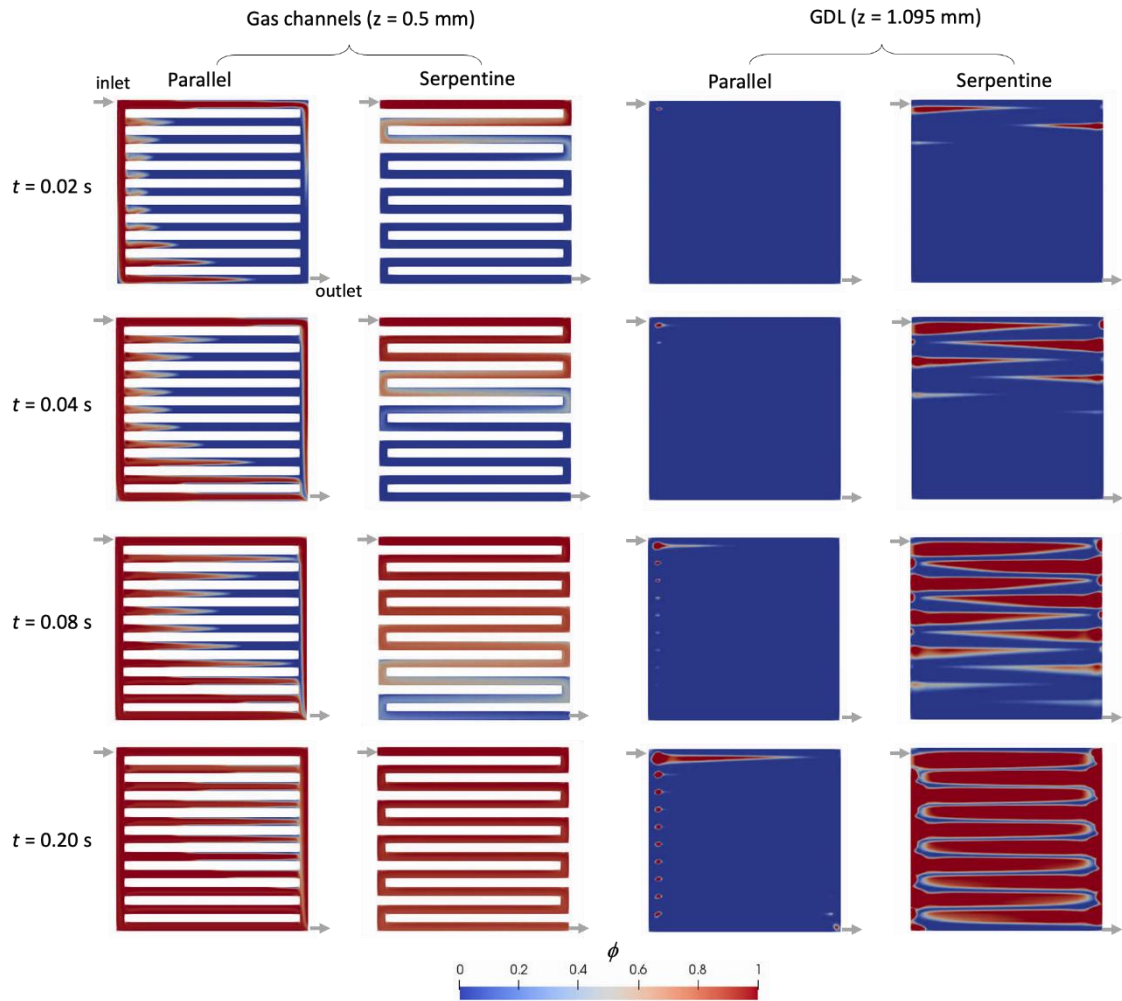
Figure 2.5: Time variation of the property of the tracer in the center sections of gas channels and GDLs

Fig. 2.5 shows the distribution of the property of the tracer changing over time after starting the continuous feed of the tracer to the inlet. In case of the parallel channel, the property convection rate in the channels near the inlet and outlet is 2–4 times higher than that in the middle channels, due to the nonuniform velocity distribution. This phenomenon happens because of the nonlinear pressure profile in the manifolds, as a result, the pressure drop as well as the velocity in each channel is different. When the manifold is wide enough, *i.e.* the pressure drop of the manifold is neglectable, the velocity distribution can be even. Since a part of the gas flows to the outlet quickly, the tracer can be detected at the outlet earlier than the case of serpentine. After 0.20 second from feeding the tracer, it filled most of the gas channel, and the concentration in the GDL of parallel channel is still much lower than that of the serpentine channel. The effect of cross flow in the GDL can be also intuitively observed in Fig. 2.5. In case of the serpentine channel, the pressure difference between neighboring channels remarkably promotes the gas
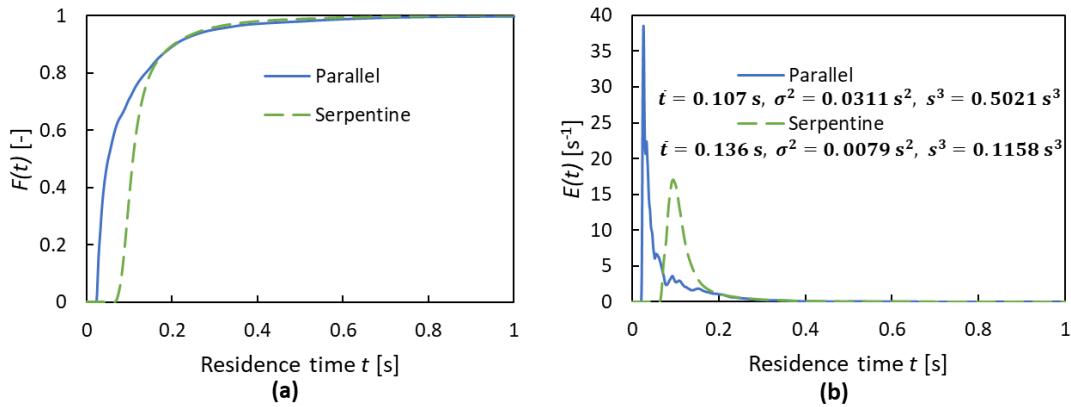
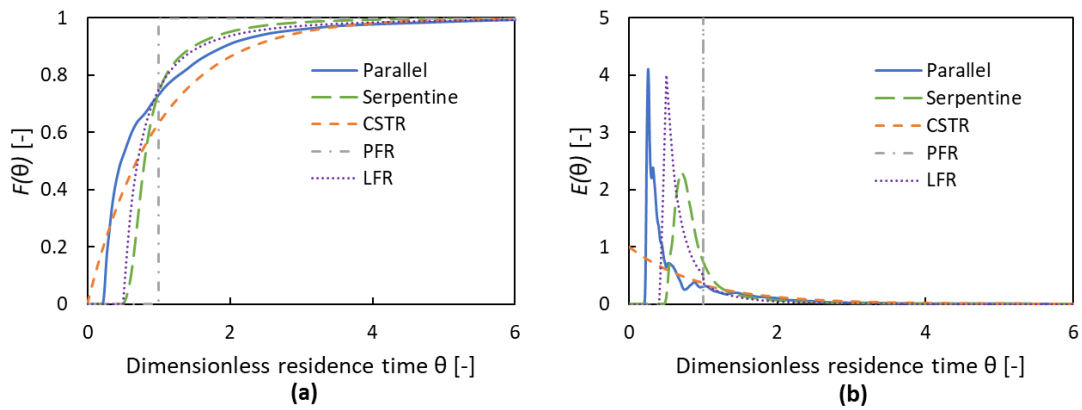Figure 2.6: Residence time distribution of parallel and serpentine channels with GDLs

Figure 2.7. Dimensionless-residence-time distributions of different gas channels with GDLs and ideal reactor models

flowing across the GDL. On the other hand, in case of the parallel channel, although the pressure difference also exists between neighboring channels owing to the uneven velocity distribution, the pressure difference is little so that the cross flow is much less obvious than that of the serpentine channel. Furthermore, the cross flow could be rather not observed when the manifold is wide in case of the parallel channel.

The RTD can be obtained by analyzing the time variation of integrated average property of the tracer on the outlet faces, as shown in Fig. 2.6. Both of the parallel and the serpentine channel exhibits that the characters of the RTD. The gas at cell outlet has no component of the residence time shorter than which the response of the tracer can be detected. The RTD function $E(t)$ has the maximum value near the time of initial response of tracer, and then gradually decreases at longer residence time. Three parameters: mean residence time, variance and skewness, which are often applied to describe the features of the RTD, are also shown in Fig. 2.6. The mean residence time of parallel is shorter than the serpentine channel, which indicates some dead volume where the gas cannot reach may exist in the GDL in case of parallel channel. Some oscillation of RTD function of the parallel channels can be detected, due to the nonuniform distribution of the velocity.
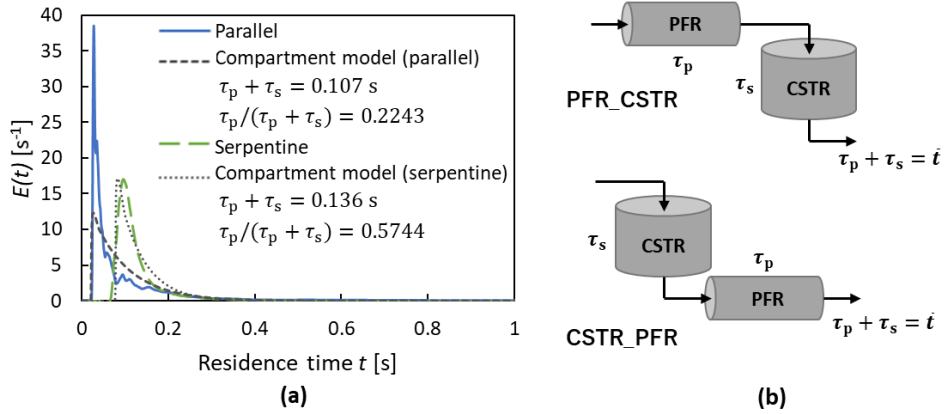
Figure 2.8: RTD functions of gas channels with GDLs (a) and compartment models (b)

Table 2.2: Dimensionless-residence-time-based RTD function of different model

Model	$F(\theta)$	$E(\theta)$
CSTR	$1 - \exp(-\theta)$	$\exp(-\theta)$
PFR	$U(\theta - 1)$ (Step function)	$\delta(\theta - 1)$ (Dirac delta function)
LFR	$\begin{cases} 0 & (0 \leq \theta < 0.5) \\ 1 - 1/(4\theta^2) & (\theta \geq 0.5) \end{cases}$	$\begin{cases} 0 & (0 \leq \theta < 0.5) \\ 1/(2\theta^3) & (\theta \geq 0.5) \end{cases}$

Dimensionless residence time: $\theta = t/\bar{t}$

The RTD functions of dimensionless residense time can be derived by normalizing the residence time by the mean residence time, as shown in Fig. 2.7. The RTD functions of CSTR, PFR and laminar flow reactor (LFR) plotted in Fig. 2.7 were calcutaled by equations listed in Table 2.2.

Various model can be suggested to express the RTD of cell with the parallel and the serpentine channels. The compartment models, which combines PFR and CSTR in series, is simple and direct so that is applied in this study. By applying appropriate resistence times of PFR and CSTR, the characters of RTD of the parallel and the serpentine channels can be reproduced, as shown in Fig. 2.8(a). The RTD function of the combination of PFR and CSTR in series which can be written as Eq. (2.13).

$$E(t) = \begin{cases} 0 & (t < \tau_p) \\ \dfrac{\exp\left(-\dfrac{t - \tau_p}{\tau_s}\right)}{\tau_s} & (t \geq \tau_p) \end{cases} \tag{2.13}$$

where t is the residence time, τ_p and τ_s are the space time of PFR and that of CSTR. The total space time, $i.e.$, the sum of τ_p and τ_s, is equal to the mean residence time, $\bar{t}$. By applying the suggested compartment model, the macromixing in the gas channel and

GDL can be thus simply represented by the ratio of the space time of PFR to the total space time. The serpentine channel exhibited $\tau_p/\bar{t} = 0.57$, which is closer to the plug flow than the parallel flow exhibiting $\tau_p/\bar{t} = 0.22$. The larger ratio of CSTR in case of the parallel channel indicates that the gas macromixing of each straight channel in its manifold is more remarkable than the gas macromixing due to the cross flow in the serpentine channel.

However, both of the PFR followed by the CSTR and the CSTR followed by the PFR has the same RTD function, as shown in Fig. 2.8(b). The orders of CSTR and PFR in cases of the parallel and the serpentine channels should be determiend accroding to the experimental results.

2.4.2 Performances of different gas channels

Fig. 2.9 shows the experimental polarization curves of different active areas and inlet gas flow rates in case of parallel gas channels, where the cell voltages are corrected by experimental HFR results. In case of large active area, higher current density, i.e., total current divided by active area, was observed under high cell voltage. It indicates that the local current density at the inlet is lower than that at the outlet, which resulted from the relatively high average RH of gas due to humidification by the water produced in ORR, and the decrease of oxygen partial pressure is little which cannot overtake the effects of the humidification. It infers that the ORR has the similar behavior of the self-catalytic reaction. The humidification of the water increases the ORR rate at low oxygen conversion, on the other hand, the decreasing oxygen partial pressure reduces the ORR rate at high conversion.
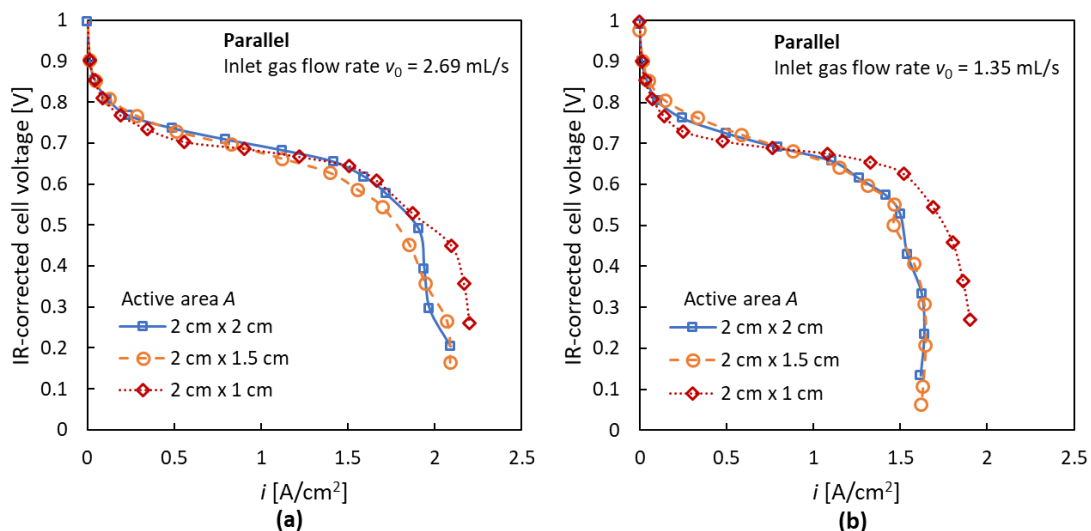

Figure 2.9: Polarization curves of different active areas

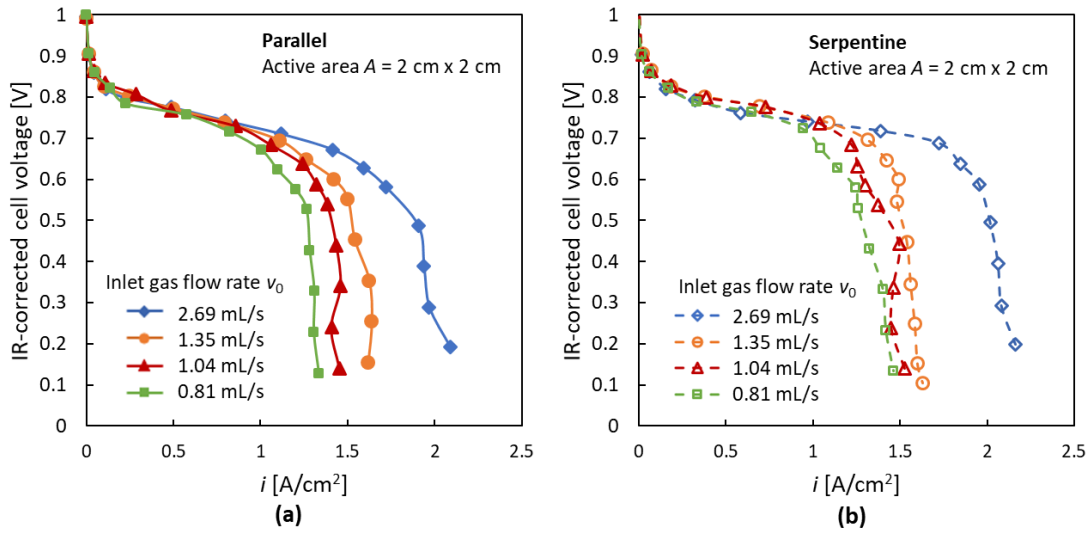(parallel channel, (a) $v_0 = 2.69$ mL/s, (b) $v_0 = 1.35$ mL/s)

Figure 2.10: Polarization curves of different inlet gas flow rates
((a) parallel gas channel, (b) serpentine gas channel)

However, the limited current density is higher in case of the 2 cm×1 cm, and limited current densities in cases of the 2 cm×1.5 cm and 2 cm×2 cm are nearly equal. The reason may be the flooding in case of the larger active area, so that the oxygen transfer resistance increases due to the presence of liquid water. On the other hand, the difference in limited current density between 2 cm×1 cm and other cases is smaller in case of gas flow rate of 2.69 mL/s, comparing to 1.35 mL/s, which infers that the humidification of the produced water is less effective in case of the high gas flow rate, so that the flooding is less remarkable. This result also indicates that the flooding occurs at the 1/2−3/4 length of the gas channel from the inlet.

Fig. 2.10 shows the polarization curves of different inlet gas flow rates in the fixed active area in case of the parallel and the serpentine gas channels. The performances under different inlet gas flow rate and gas channels conditions are nearly the same when the current density is lower than 0.6 A/cm^2, which indicates that the effect of the water humidification compensated the effects of the oxygen consumption. However, the limited current density is lower in cases of low inlet gas flow rate. The oxygen conversion and oxygen partial pressure at the limited current density are about 0.66 and 17.0 kPa in case of the gas flow rate of 0.81 mL/s, and 0.312 and 27.3 kPa in case of the gas flow rate of 2.69 mL/s, which indicated that the insufficient oxygen supply causes the low oxygen partial pressure so that the oxygen mass transport resistance increases near the limited current density.
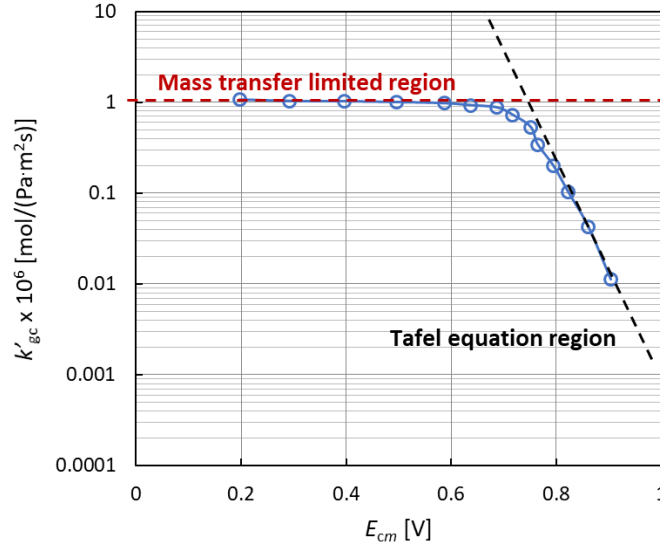
Figure 2.11: Kinetics data measured by differential reactor (Gas channel: parallel, humidified temperature: 65 °C, H_2 flow rate: 200 cm^3/min (20 °C, 1 atm), O_2 flow rate: 100 cm^3/min (20 °C, 1 atm))

2.4.3 Determination of reactor models

One polarization curve of the parallel gas channel in Fig. 2.9 was used to obtain the ORR kinetics. The oxygen flow rate was 100 cm^3/min (20 °C, 1 atm), where the oxygen conversion was 0.08 at 0.74 V of the IR-corrected cell voltage. Since the conversion is low, the cell can be regarded as a differential reactor, which assumes even concentration and reaction rate distributions in the reactor. By regarding the oxygen concentration in the reactor as the arithmetic mean of the cell inlet and outlet oxygen concentration, and calculating the oxygen partial pressure and RH from Eqs. (2.9) and (2.10), the reactor model equation can be written as Eq. (2.14),

$$\frac{x_O}{A/v_0} = k'_{gc} \frac{RTP}{p_S^{sat}} \frac{(1 - \bar{x}_O)(y_{S0} + 2y_{O0}\bar{x}_O)}{(1 + y_{O0}\bar{x}_O)^2} \tag{2.14}$$

where k'_{gc} represents the partial-pressure-based apparent kinetics constant [mol/(Pa·m^{2}s)] at RH = 1, and $\bar{x}_O$ represent the average oxygen conversion throughout the gas channel. Consequently, the observed ORR kinetics which contain the effectiveness factors can be calculated simply, as shown in Fig. 2.11. The ORR kinetics demonstrate that the polarization curve has 2 regions: Tafel equation region at high electrical potential and Mass transport limited region. at low electrical potential. The former region exhibits that the kinetics constant is proportional to the exponential of the IR-corrected cell voltage. The latter region indicates that the mass transfer is the limiting step so that the reaction rate tends to be independent to the IR-corrected cell voltage.

46
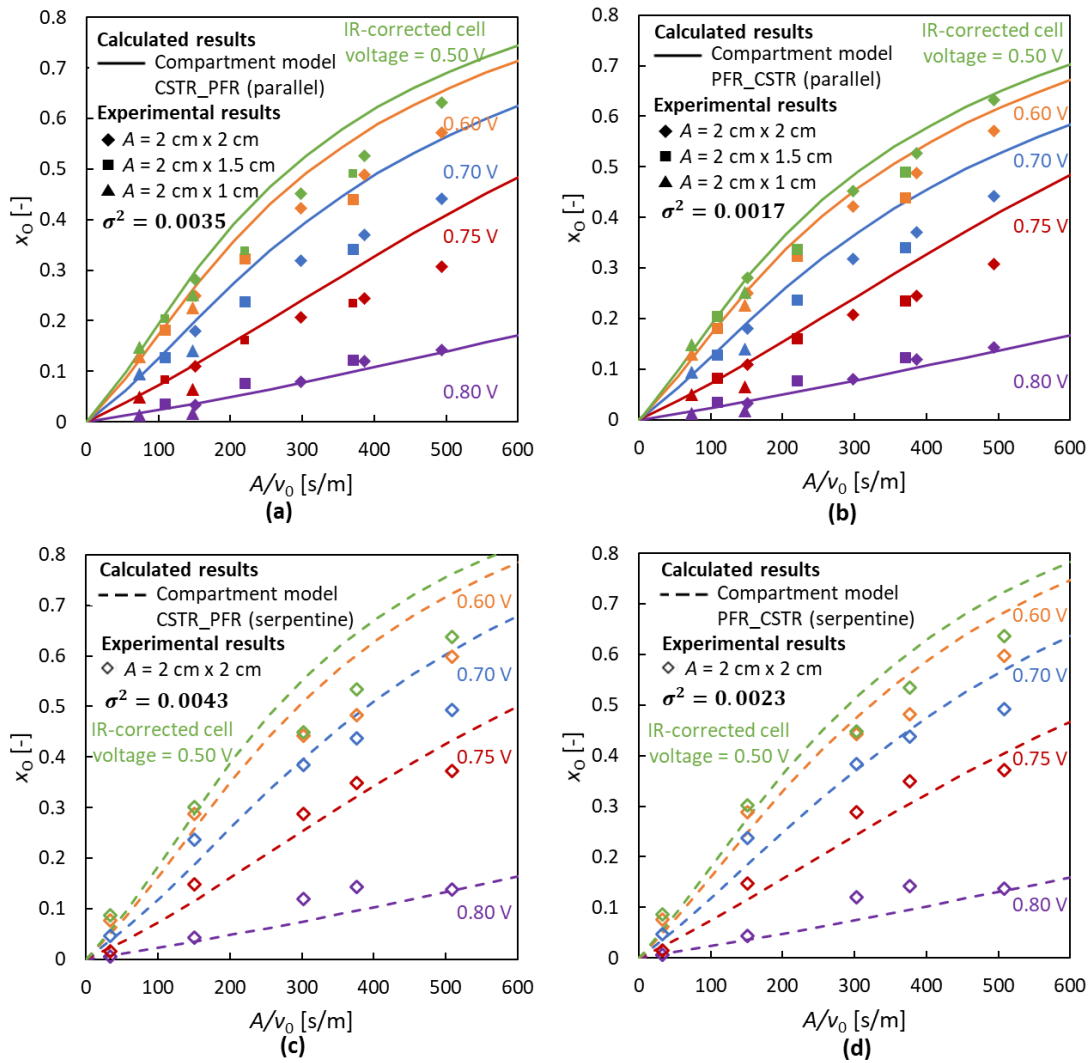
Figure 2.12: Relationship of oxygen conversion and active area/inlet flow rate at different IR-corrected cell voltage (the data at A = 2 cm × 2 cm, v_0 = 2.69 mL/s in case of the parallel channel was applied to derive the ORR kinetics. (a) CSTR followed by PFR model for the parallel channel, (b) PFR followed by CSTR model for the parallel channel, (a) CSTR followed by PFR model for the serpentine channel, (b) PFR followed by CSTR model for the serpentine channel)

By applying the ORR kinetics derived above, the oxygen conversion at different space time, *i.e.*, the ratios of the active area to the inlet flow rate, can be calculated. Different orders of PFR and CSTR in the compartment model shown in Fig. 2.8(b) in cases of the parallel and the serpentine channels were applied in the calculation and compared with experimental results, as shown in Fig. 2.12.

The deviations of the calculated results from the experimental results were evaluated by the variance, σ^2, which is calculated by summarizing the differences of the oxygen

conversion between calculated and experimental data at the fixed space time at varied IR-corrected cell voltage. According to the results, the PFR followed by CSTR models offer lower variance in cases of both the parallel and the serpentine channels, which indicates that the PFR followed by CSTR models have higher accuracy to express the cell performance, as shown in Fig. 2.12(b) and (d).

Generally, the curves fit well with the experimental data. However, different degrees of deviations occur in Fig. 2.12(b) and (d). In case of the parallel channel, the predicted oxygen conversion is higher than the experimental data in the region where the space time is longer than 300 s/m, the reason may be caused by the liquid water flooding. In this region, lager active area or lower flow rate is beneficial for the liquid water generation. Some dead space, where the gas is unable to arrive, forms due to the liquid water, so that the residence time of the reactant is shortened. As a result, the actual residence time is shorter than the expected space time, and the oxygen conversion as well as the total current decreases. At high IR-corrected cell voltage, *e.g.*, 0.80 V, the water generation rate is slow, and the water droplet does not form, so that the model successfully reproduces the experimental results. Similar deviation occurs in the region of IR-corrected cell voltage lower than 0.60 V and space time longer than 300 s/m in cases of the serpentine channel, so that the same reason mentioned above can be attributed.

2.4.4 Effects of gas macromixing

The compartment model of combining PFR and CSTR in series can describe the macromixing of the gas channel with GDL quantitively. According to the compartment models derived in the previous section, the parallel channel has larger ratio of CSTR to the space time, its performance is closer to the CSTR. On the other hand, the serpentine
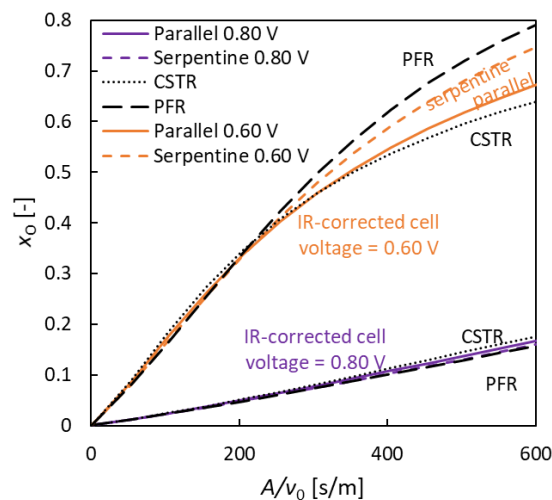

Figure 2.13: Impact of active area/inlet flow rate in cases of different reactor models
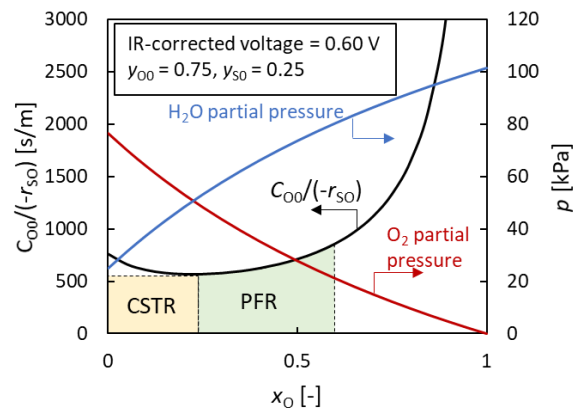
Figure 2.14: Optimal oxygen conversion of ORR reaction at fixed IR-corrected cell voltage and inlet gas composition. The combination of 32.8% CSTR + 67.2% PFR gives the minimum A/v_0 requirement to reach 0.6 of oxygen conversion.

channel has larger ratio of PFR to the space time, so that it is closer to the PFR, shown as Fig. 2.13.

Since the ORR conversion has the similar behavior as the self-catalytic reaction, as mentioned in the previous section, a critical value of the oxygen conversion exists. The humidification due to the reaction promotes the ORR rate when the oxygen conversion is lower than the critical value, where the gas macromixing is beneficial to the cell performance. On the other hand, the oxygen consumption restrains the ORR rate when the oxygen conversion is higher than the critical value, so that the gas macromixing is unbeneficial to the cell performance. Therefore, comparing to PFR, higher oxygen conversion at fixed space time in CSTR can be obtained when the oxygen conversion is lower than the critical value, *vice versa*. It also indicates that the parallel has better performance than the serpentine at relatively low oxygen conversion, and serpentine has better performance than the parallel at relatively high oxygen conversion. However, at low oxygen conversion, the difference of the performance among PFR, CSTR, parallel and serpentine is not obvious in the present situation.

A cell design procedure can also be suggested according to the theory of chemical reaction engineering. Since the enhancement of water humidification is beneficial to the cell performance at low oxygen conversion, the gas macromixing is expected to be promoted in this region, and CSTR can be thus applied in this region. On the other hand, the oxygen consumption is a main drawback of the cell performance at high oxygen conversion, the gas macromixing should be restrained, so that PFR can be applied in the high oxygen conversion region. It indicates that a structure which promotes the gas macromixing can be designed near the cell inlet in the gas channel to improve the cell

performance. For example, under the operating condition illustrated in Fig. 2.14, the area of yellow rectangular, *i.e.*, 113 s/m, represents the required A/v_0 of CSTR when the oxygen conversion of the inlet and outlet are 0 and 0.21. The area of the green parts surrounded by the $C_{O0}/(-r_{SO})$ curve and x_O-axis, *i.e.*, 232 s/m, represents the required A/v_0 of PFR when the oxygen conversion of the inlet and outlet are 0.21 and 0.6, according to the physical meaning of Eq. (2.11) and (2.12). And a cell whose characteristic can be described as a series of 113/(113 + 232)=32.8% CSTR followed by 67.2 % PFR has optimally minimum requirement of $A/v_0 = 345$ s/m to achieve 0.60 of oxygen conversion. In the other words, when the gas flow rate condition is determined, oxygen conversion can be adjusted to obtain the expected current density fixed IR-corrected cell voltage, and then the gas channel suggested by this method offers the minimized active area.

2.4.5 Model evaluation

The polarization curve can be also obtained from the oxygen conversion at different IR-corrected cell voltage, as shown in Fig. 2.15, where the parameter $\tau_p/\bar{t}$ is fixed in cases of the parallel and the serpentine respectively. The calculated results in case of the parallel channel have a good agreement with the experimental results in the whole region of the current density in cases. On the other hand, the calculated results in case of the serpentine channel cannot reproduce the experimental results in the high current density region. The calculated cell performance is worse than the experimental results in case of 2.69 mL/s flow rate condition, which is opposite when the flow rate is lower than 1.35 mL/s. The reason can be attributed to the severer liquid water flooding, and the inlet flow rate lower than 1.35 mL/s is not high enough for the water removal. The ORR kinetics
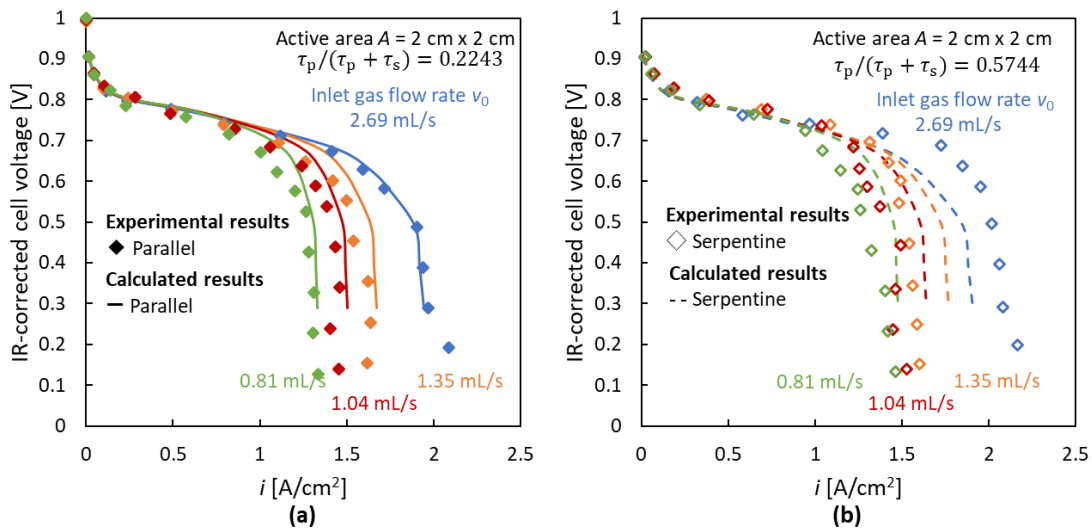

Figure 2.15: Comparison of experimental and calculated polarization curve at different inlet gas flow rate ((a) parallel channel, (b) serpentine channel)
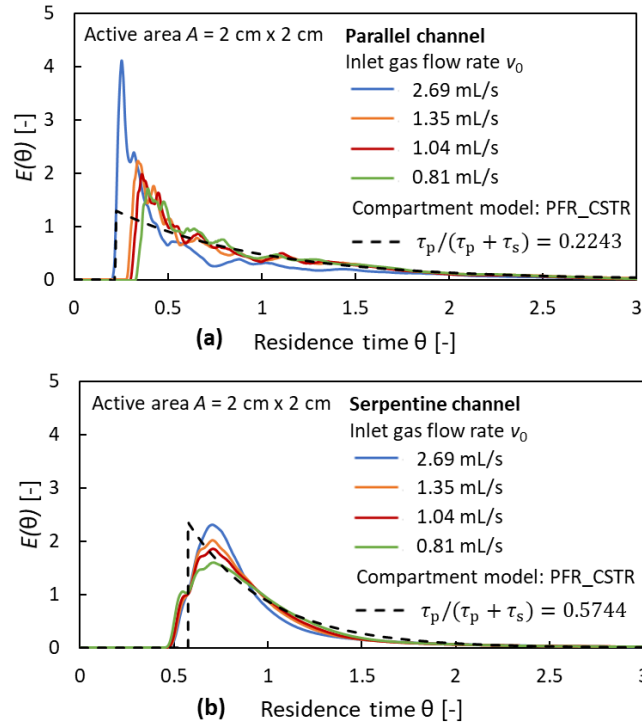
Figure 2.16: Dimensionless RTD functions at different gas flow rate
((a) parallel channel, (b) serpentine channel)

was derived from the data in case of the parallel at 2.69 mL/s, in which the flooding may occurs. However, the same ORR kinetics was applied in case of the serpentine at 2.69 mL/s, in which the liquid water can be removed due to the high gas velocity, so that the experimental performance is better than the prediction. On the other hand, when the gas flow rate is lower than 1.35 mL/s, severe flooding happens in both of the parallel and the serpentine channels, so that their experimental cell performances approaches each other, regardless of the calculated results by the compartment model.

In addition, the RTD is affected by the operating conditions. In order to compare the cell performance, fixed parameter $\tau_p/\bar{t}$ under different conditions in the same gas channel was applied, and the calculated results had a good agreement with the experimental data. However, the compartment model may need to be modified under the different conditions to predict the cell performance more accurately. Fig. 2.16 shows the dimensionless RTD functions at different gas flow rate conditions, which indicates that the applied compartment model may offer a result deviating from the actual case. Moreover, the RTD is also affected by the reaction, which changes gas velocity, pressure, composition, and temperature, especially at the high oxygen conversion condition. In future work, the effect of the flooding, the variation of RTD due to the reaction, and the

uneven distributions of temperature and pressure should be concerned to modify the reactor model and eliminate the deviation of the model from the experimental results.

2.5 Conclusions

The method in the perspective of chemical engineering was applied to understand the gas macromixing in PEFC, by regarding which as a continuous reactor. To characterize the gas mixing behavior, the RTDs of parallel and serpentine gas channels were simulated by numerical method. The gas macromixing due to different mechanism occurs in these 2 channels: the cross flow due to the steep pressure gradient between the neighbor channels in the serpentine channels, and the uneven velocity distribution in the parallel channels. A compartment model of PFR followed by CSTR in series in considered to describe the macromixing of gas with different residence time according to the RTD. Consequently, the cell with parallel channel can be regarded as 22.4 % PFR and 77.6 % CSTR, and the cell with the serpentine can be regarded as 57.4 % PFR and 42.6 % CSTR.

The self-catalytic reaction behavior of ORR was observed experimentally, which indicates that the water humidification is more beneficial to the ORR rate at low oxygen conversion, and the oxygen consumption becomes the main drawback at high oxygen conversion, so that a critical oxygen conversion exists. Therefore, the gas macromixing is beneficial to the cell performance at relatively low oxygen conversion, *vice versa*. According to the compartment models, the serpentine channel has better performance than the parallel channel at high oxygen conversion due to the lager ratio of PFR, and the parallel channel has better performance at low oxygen conversion. It also indicates that a structure which promotes the gas macromixing can be designed near the cell inlet in the gas channel to improve the cell performance.

The compartment model reproduces the experimental results well, especially at low oxygen conversion. To satisfy the requirement of higher accuracy for the further usage, more accurate reactor model can be suggested according to the RTD. Furthermore, a model which can estimate the effects of RTD under different operating conditions is another potential direction of this work. The method mentioned in this study can be applied to other shapes of gas channels and may be helpful for the cell design in the future.

2.6 Symbols

A	Active area	[m^2]
a_w	Water activity	[-]
C_{O0}	Oxygen concentration in the inlet gas	[mol/m^3]
$E(t)$	RTD function	[s^{-1}]
$F(t)$	Cumulative RTD function	[-]
F	Faraday constant	[C/mol]
i	Current density	[A/m^2]
k_{gc}	Reaction rate constant	[mol/(Pa$\cdot$m$^2\cdot$s)]
k'_{gc}	Reaction rate constant at RH=1	[mol/(Pa$\cdot$m$^2\cdot$s)]
K	Permeability	[m^2]
p_i	Partial pressure of species i	[Pa]
p_S^{sat}	Saturated pressure of water vapor	[Pa]
P	Total pressure	[Pa]
$-r_{si}$	Surface consumption rate of species i	[mol/(m$^2\cdot$s)]
R	Molar gas constant	[J/(K$\cdot$mol)]
s^3	Skewness	[s^3]
S	Source term	
t	Residence time	[s]
T	Temperature	[K]
U	Velocity vector	[m/s]
v_0	Inlet gas volume flow rate	[m^3/s]
x_O	Oxygen conversion	[-]
y_{i0}	Mole fraction of species i at cell inlet	[-]
Greeks		
ϕ	Specific physical property of the tracer	
Γ	Diffusivity of specific physical property	[m/s^2]
θ	Dimensionless residence time	[-]
μ	Viscosity	[Pa$\cdot$s]
ρ	Density	[kg/m^3]
σ^2	Variance	[s^3], [-]
τ	Space time	[s]
Subscripts		
0	Cell inlet	

L	Cell outlet
i	Species *i*
O	Oxygen
S	Water steam
s	CSTR
p	PFR
x	*x* direction
y	*y* direction
z	*z* direction

2.7 References

[1] M. Kawase, M. Nagayoshi, G. Inoue, and M. Kageyama, *ISCRE 23 & APCRE 7, Bangkok*, Sep. 8, OE03 (2014).

[2] A. Nishimura, K. Yamamoto, T. Okado, Y. Kojima, M. Hirota, and M. L. Kolhe. *Energy*, **205**, 117875 (2020).

[3] A. Nishimura, K.Shibuya, A. Morimoto, S. Tanaka, M. Hirota, Y. Nakamura, M, Kijima, and M. Narita, *J. Environ. Eng.*, **6**, 1–16 (2011).

[4] F. Liu, M. Kvesić, K. Wippermann, U. Reimer, and W. Lehnert, *J. Electrochem. Soc.*, **160**, F892 (2013).

[5] A.A. Kulikovsky, *Electrochim. Acta*, **49**, 617–625 (2004).

[6] G. Inoue, T. Yoshimoto, Y. Matsukuma. M. Minemoto, H. Itoh, and S. Tsurumaki, *J. Pow. Sour.*, **162**, 94–104 (2006).

[7] J. Park, and X. Li, *Int. J. Energy Res.*, **35**, 583–593 (2011).

[8] T. Berning, N. Djilali, and *J. Electrochem. Soc.*, **150**, 1589–1598 (2003).

[9] S. Zhang, S. B. Beale, U. Reimer, M. Andersson, and W. Lehnert, *Int. J. Hydrog. Energy*, **45**, 19761–19777 (2020).

[10] P. D. Neufeld, A. R. Janzen, and R. A. Aziz, *J. Chem. Phys.*, **57**, 1100 (1972).

[11] C. R. Wilke, and *J. Chem. Phys.*, **18**, 517 (1950).

[12] J. T. Gostick, M.W. Fowler, M. D. Pritzker, M. A. Ioannidis, and L. M. Behra, *J. Pow. Sour.*, **162**, 228–238 (2006).

[13] M. Kawase, K. Yamaguchi, M. Kageyama, K. Sato, and G. Inoue, *ECS Trans.*, **75**(14), 147–156 (2016).

[14] M. Kawase, K. Sato, R. Mitsui, H. Asonuma, M. Kageyama, K. Yamaguchi, and G. Inoue, *AIChE J.*, **63**, 249–256 (2017).

[15] H. Ogawa, M. Kageyama, and M. Kawase, *ECS Trans.*, **104** (8), 45–58 (2021).

[16] S. Cruz-Manzo, and R. Chen, *J. Electroanal. Chem.*, **694**, 45–55 (2013).

Chapter 3

Diving Flow and Cross Flow in Partially Narrowed Flow Fields

3.1 Introduction

Flow fields of PEFC play important parts in flow distribution and water management. By optimizing the flow fields, the mass transport resistance as well as the performance of PEFC can be expected to be improved. The novel partially narrowed flow fields have been employed in the second-generation MIRAI by Toyota. However, limited literature has reported the mass transport mechanisms and the effects of under-rib convection, *i.e.*, cross flow, in this kind of flow fields, as mentioned in the Introduction chapter.

In this chapter, the innovated flow fields with varied partially narrowed channel are applied to comprehend the mass transfer promoted by the convection caused by the baffle structure of the flow field in the in-plane and through-plane directions quantitively. The polarization curves as well as high frequency impedances under different operation conditions were directly measured by the experiments. A 3D CFD model was also developed to investigate the transport phenomenon within the cell.

3.2 Experimental

A Japan Automobile Research Institute (JARI) type cell was used in the experiments. The active area was reduced to 20 mm×22 mm so that the temperature distribution is less
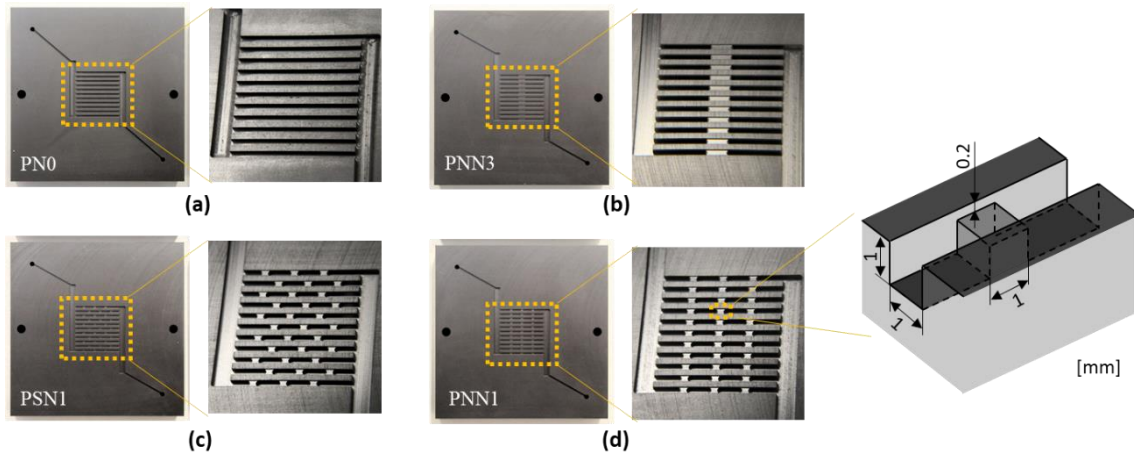
Figure 3.1: Bipolar plates applied in the experiments:
(a) PN0; (b) PNN3; (c) PSN1; (d) PNN1

uneven in the in-plane direction. The membrane electrode assembly was consisted of the cathode and anode catalyst layers made of 50 wt% Pt/carbon black catalyst particles with ionomer and the membrane (Chemours Nafion™ PFSA NR-212). The carbon black utilized in the CLs is Ketjen black, which has secondary pores inside carbon particles, and Pt is supported on both secondary pores' and particles' surfaces of the carbon. Ionomer/carbon weight ratio was 1.0, and the catalyst layers thicknesses of anode and cathode were 10 μm. 85 wt% carbon paper (Toray TGP-H-060) dealt with 15 wt% PTFE was used as GDL. The MPL was not employed in this study.

The BPs were made of carbon. Four kinds of flow fields were used in the cell: parallel without narrowed channels (PN0), parallel with staggered 1-mm-long narrowed channels (PSN1), parallel with neat-arranged 1-mm-long and 3-mm-long narrowed channels (PNN1, PNN3). On these BPs, 11 separated flow channels were parallelly arranged. The length, width and depth of each separated flow channels were 20 mm, 1 mm and 1 mm respectively. The ribs, whose width were 1 mm, were located between separated flow channels. The widths of manifolds of flow field were 3 mm, wider than that of the separated channels, so that a nearly equal flow rate in each separated channel could be supplied. The narrowed channels in the flow channels shrink the channel heights between the land and the GDL to 0.2 mm. Along with suddenly increased local pressure drop at the narrowed channels, a portion of the reactant gas are forced to flow into the GDL, and the mass transfer in the GDL can be thus enhanced. The GDLs as well as the active area covered all flow fields but the manifolds. The BPs were changed only on the cathode side, and PN0 was always applied on the anode side in the experiments.

The cell was operated in a thermostatic chamber whose temperature was controlled to maintain the temperature at the center of the cathode gas channel at 80 °C. The pressure
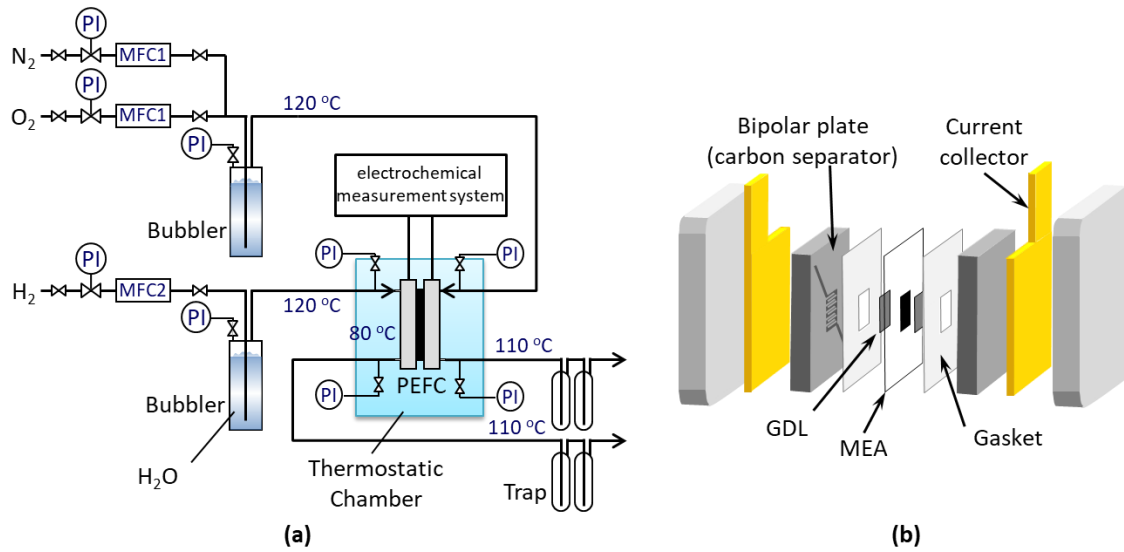
Figure 3.2: Experiment apparatus and cell structure

at the cell outlet was 1 atm. Reactant gases, *i.e.* pure H_2 supplied to the anode and O_2 mixed with N_2 supplied to the cathode, were humidified in the bubblers, in which 65 ˚C distilled water was filled. The O_2 flow rate was 50–200 cm³/min (20 °C, 101.325 kPa on dry basis, applied to all flow rate mentioned in this article), which is 0.5 times to the H_2 flow rate. The O_2 mole fraction, as well as the total flow rate, on the cathode side was varied by the N_2 flow rate.

Polarization curves and electrochemical impedance spectra were obtained using an electrochemical measurement system (Hokuto Denko Corp., HZ-7000). The polarization curves were measured by potentiostatic method at fixed inlet total flow rates. The cell voltages were controlled from OCV to 0.05 V by steps, and the average current was utilized at each cell voltage. The impedance spectra were measured in a range of frequency from 100 mHz to 100 kHz. A standard equivalent circuit model was employed to determine the high frequency resistance (HFR)[1]. The cell voltage was corrected by the HFR results.

3.3 Numerical Models

The 3D CFD model in this work was established to simulate the distribution of velocity, pressure, composition, local current density, at a specific electromotive force in the computational domain, which contains the flow channels and GDLs on the cathode side.

The calculation was achieved by using an open source toolbox OpenFOAM 9 based on finite volume method[2].

3.3.1 Geometry

The geometries of the flow fields in the calculation were applied same as those in the experiments, as shown in Fig. 3.3. The manifolds of the flow fields were omitted to simplify the calculation. The sizes of gas channels, ribs and narrowed channels were all set as experiments. The GDLs were implemented as porous medias, whose size were 20 mm in x direction, 22 mm in y direction, and 0.190 mm in z direction. The original coordinate was defined at a corner of the GDL in the GDL-CCL boundary plane. In addition, the meshes of GDLs were denser than those in other parts.

3.3.2 Assumptions

The cell is in steady state and isothermal. The reactant gas is regarded as ideal gas and the flow is laminar. The GDL is considered as a uniform porous medium in which the gas flow obeys Darcy's law. Water only exists in vapor phase, since the relatively low RH condition is applied in the experiments due to the low humidification temperature and high flow rate. The permeation fluxes of reactant and water through PEM are neglected.
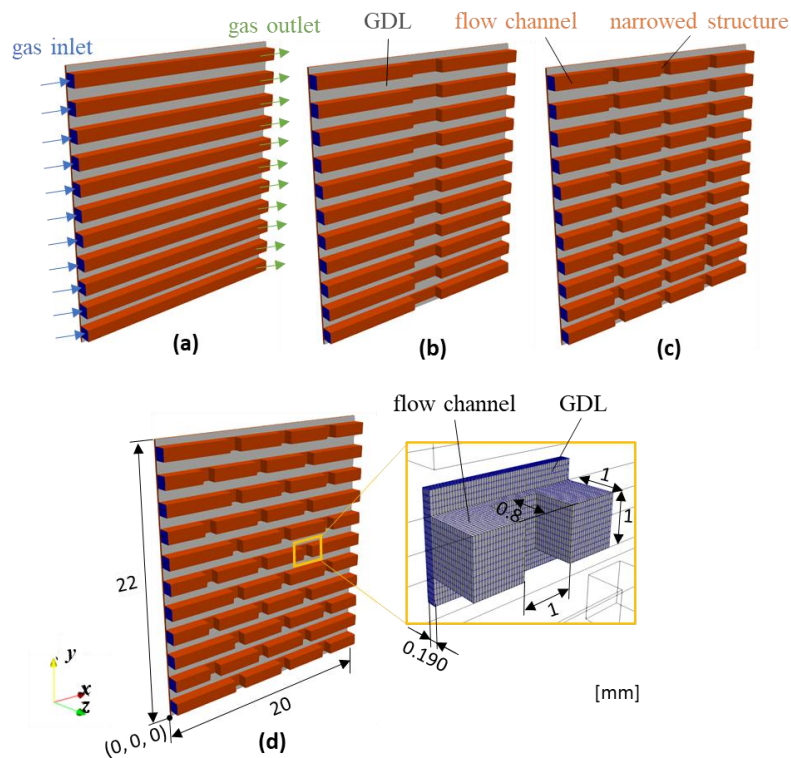

Figure 3.3: Geometries of cathode side flow fields and a part of the mesh:
(a) PN0, (b) PNN3, (c) PNN1, (d) PSN1

The IR of the PEM, as well as the IR-corrected cell voltage, evenly distributes in the in-plane direction. The ORR is considered as a surface reaction which completely occurs on the GDL-CL boundary surface. Thus, the computational domain only consists the flow channels and GDLs on the cathode side. Moreover, the inlet gas mass flow rate of each channel is assumed to be equal, and the pressure at outlet of each channel is regarded as atmosphere pressure

3.3.3 Governing equations

__Fluid flow.__ Equations applied to calculate the velocity and pressure fields are expressed by Eqs. (3.1) and (3.2).

Mass conservation:

$$\nabla \cdot (\rho \boldsymbol{U}) = 0 \tag{3.1}$$

Momentum conservation:

$$\nabla \cdot (\rho \boldsymbol{U} \boldsymbol{U}) - \nabla \cdot (\mu \nabla \boldsymbol{U}) = -\nabla P - \mu \boldsymbol{D_K} \boldsymbol{U} \tag{3.2}$$

where $\boldsymbol{U}$ and P represent the velocity vector and the static pressure, respectively. $\boldsymbol{D_K}$ is Darcy coefficient tensor, which represents the reciprocal of the permeability K [m^2] of the GDL in different directions, shown as Eq. (3.3). Although the GDL is anisotropic, the permeability K in the in-plane directions, *i.e.* x and y directions, can be regarded as a constant, but different in the through-plane[3], *i.e.* z direction. Moreover, $\boldsymbol{D_K}$ equals to 0 in the flow channels.

$$\boldsymbol{D_K} = \begin{pmatrix} 1/K_x & 0 & 0 \\ 0 & 1/K_y & 0 \\ 0 & 0 & 1/K_z \end{pmatrix} \tag{3.3}$$

ρ and μ represent the density [kg/m^3] and viscosity [Pa·s] of the reactant gas, which are the functions of the gas composition, calculated from Eqs. (3.4) and (3.5).

$$\rho = \frac{P}{RT} \sum y_i M_i = \frac{P}{RT} / \sum \frac{\omega_i}{M_i} \tag{3.4}$$

$$\mu = \sum y_i \mu_i \tag{3.5}$$

where y_i and ω_i represent the mole and the mass fraction of species i. M_i and μ_i are the molar mass [kg/mol] and the viscosity of pure component i. R is the universal gas constant, and T is the temperature [K].

__Mass transfer.__ The set of mass transfer equations, shown as Eq. (3.6), is solved for $i = 1, 2, ..., n - 1$. In this study, 2 species, O_2 and H_2O, were solved by Eq. (3.6). The inert

species n, which is N_2 in this study, is obtained algebraically according to the sum of the fractions being 1.

Mass transfer:

$$\nabla \cdot (\rho \boldsymbol{U} \omega_i) - \nabla \cdot (\boldsymbol{D_{ei}} \rho \nabla \omega_i) = 0 \tag{3.6}$$

where the $\boldsymbol{D_{ei}}$ represents the effective diffusivity [m^2/s] tensor of species i, which is obtained by Eq. (3.7).

$$\boldsymbol{D_{ei}} = \begin{pmatrix} (\varepsilon/\tau)_x & 0 & 0 \\ 0 & (\varepsilon/\tau)_y & 0 \\ 0 & 0 & (\varepsilon/\tau)_z \end{pmatrix} D_i \tag{3.7}$$

where ε/τ is the ratio of the porosity [-] to tortuosity [-] in a specific direction in the porous layer. Given that the Knudsen diffusion is neglected due to the high porosity of the GDL, so that ε/τ can be regarded as the effectiveness factor of the diffusivity. The anisotropic of ε/τ in the porous layer of varied materials and porosities has been reported[4]. According to the literature above, τ is approximately equals to $\varepsilon^{-1/2}$ which conforms to Bruggeman relation[5] in the x and y directions, but is greater than $\varepsilon^{-1/2}$ in the z direction. In addition, for the computational domain in the flow channel, ε/τ equals 1.

D_i is the multi-component diffusion coefficient, which can be estimated from the individual binary coefficients D_{ij} by Wilke's approach[6,7], as shown in Eq. (3.8).

$$D_i = \frac{1 - \omega_i}{\sum_{j \neq i} \frac{\omega_j}{D_{ij}}} \tag{3.8}$$

According to the Chapman-Enskog theory[8], D_{ij} is proportional to $T^{3/2}P^{-1}$, which depends on the location in the flow field.

Boundary conditions. In the steady state, the reaction rate per unit active area equals to the mass flux at cathode CL and GDL boundary of each component, as shown in Eqs. (3.9) and (3.10), which restricts the boundary conditions of mass fraction of each component and velocity respectively.

$$-r_{si}M_i = \omega_i \rho \boldsymbol{U} \cdot \boldsymbol{n} - \boldsymbol{D_{ei}} \rho \nabla \omega_i \cdot \boldsymbol{n} \tag{3.9}$$

$$\sum -r_{si}M_i = \rho \boldsymbol{U} \cdot \boldsymbol{n} \tag{3.10}$$

where $-r_{si}$ is the consumption rate per active area of species i [mol/(m^2·s)], $\boldsymbol{n}$ is the normal vector at the cathode CL-GDL boundary [-], which points outward from the GDL is defined as positive orientation.

Table 3.1: Physical properties (353 K, 101.325 kPa)

Variable	Symbol	Value
Viscosity of O_2	μ_O	2.33×10^{-5} Pa·s [*]
Viscosity of H_2O (g)	μ_S	1.25×10^{-5} Pa·s [*]
Viscosity of N_2	μ_N	1.98×10^{-5} Pa·s [*]
Binary diffusion coefficient between O_2 and H_2O	D_{OS}	2.95×10^{-5} m²/s [*]
Binary diffusion coefficient between N_2 and O_2	D_{NO}	2.74×10^{-5} m²/s [*]
Binary diffusion coefficient between H_2O and N_2	D_{SN}	2.97×10^{-5} m²/s [*]
Permeability of GDL (in-plane direction)[3]	K_x, K_y	1.30×10^{-11} m²
Permeability of GDL (through-plane direction)[3]	K_z	8.99×10^{-12} m²
Porosity of GDL	ε	0.745
Porosity/tortuosity of GDL (in-plane direction)[4]	$(\varepsilon/\tau)_x, (\varepsilon/\tau)_y$	0.63
Porosity/tortuosity of GDL (through-plane direction)[4]	$(\varepsilon/\tau)_z$	0.40

[*] The data was calculated according to Chapman-Enskog theory, the methods and parameters were from reference[8].

The physical properties used in the simulation are listed in Table 3.1. The maximum Reynolds number in the calculation cases is 376, so the gas flow can be regarded as laminar.

__Electrochemical reactions.__ The ORR kinetics can be expressed as Eq. (3.11).

$$-r_{sO} = k_{gc} p_O \tag{3.11}$$

where p_O is the local oxygen partial pressure [Pa], and $-r_{sO}$ is the oxygen consumption rate per active area [mol/(m² s)], which was experimentally proved to be 1st-order to the oxygen partial pressure[9]. k_{gc} represents the partial-pressure-based apparent kinetics constant [mol/(Pa m² s)] which is the function of cathode electromotive force and RH at a fixed temperature[10]. k_{gc} is almost linear to the activity of the water vapor a_w which is equal to RH, when the mass transfer is not the main concern, according to our previous studies[11].

The local current density i [A/m²] can be calculated from the oxygen consumption rate per active area, as shown in Eq. (3.12).

$$i = -zFr_{si} \tag{3.12}$$

where F represents the Faraday constant. z represents the molecular charge number of species i [-], which equals 4 in case of the species i referring to O_2. When k_{gc} at different operating conditions is obtained experimentally, the distribution of each property can be

calculated by the model mentioned above.

3.4 Results and Discussion

3.4.1 Determination of GDL permeability and ORR kinetics

In order to estimate the diving flow rate and cross flow rate accurately, the permeability of GDL was measured and derived from experimental data. The fully blocked flow field with GDL, which has similar geometry as PNN3 but the depth of the narrowed channel was 0, was applied. Two pipelines were inserted into the manifolds in the flow channel to measure the pressure inside the pressure at the inlet and outlet of the flow fields, as shown in Fig. 3.4(a) – (b). The experiment was proceeded without electrical generation, and PTFE sheet was used to replace the MEA of the cell to ensure the no gas permeated between two BP. When dry nitrogen with different flow rates was supplied to the cell, all of the gas was forced to dive into the porous GDL. Since the flow resistances of the flow channel and manifolds are unremarkable, most of the pressure drop occurs in the GDL under the fully blocked parts of the flow channels. The pressure drops were also calculated by the CFD model mentioned in the previous sections, as shown in Fig. 3.4(c). By comparing the experimental data and calculated results, the accuracy of the Darcy equation as well as the GDL permeability can be estimated.

The relationships between flow rate of dry nitrogen and pressure drop of the fully blocked flow fields are shown in Fig. 3.5. The result shows that the pressure drop has the linear relationship with the flow rate, which infers that the Darcy equation is satisfied under the experimental conditions. Although a slightly higher experimental value than the theoretical value at high flow rate was observed, as shown in Fig. 3.5(a), the error is
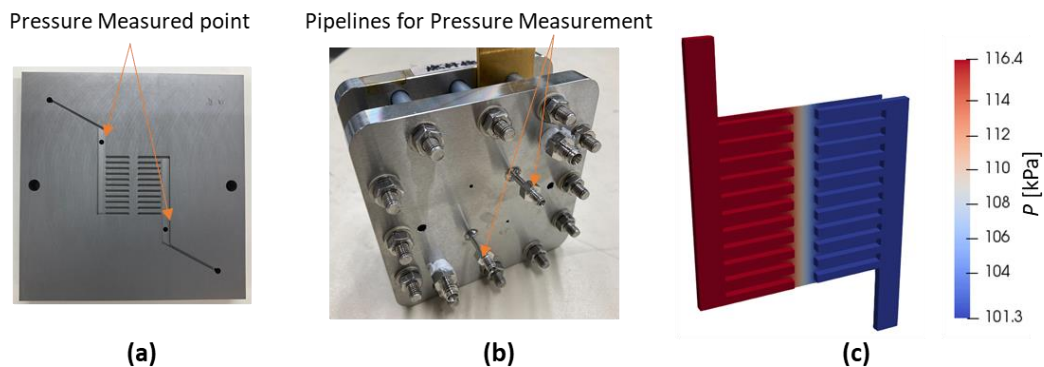

Figure 3.4: Methodology of GDL permeability determination
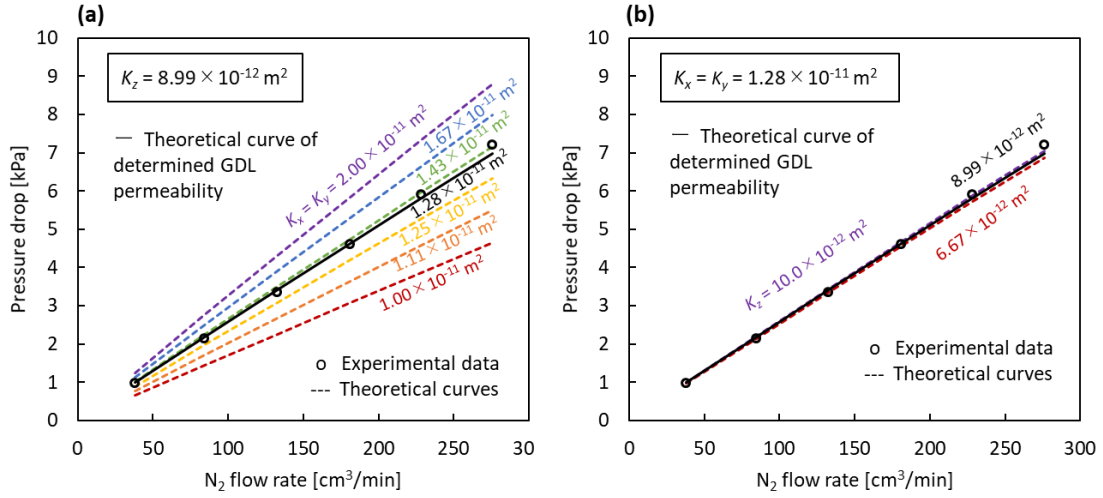(a) fully blocked BP, (b) cell, (c) pressure profile obtained by CFD simulation

Figure 3.5: Impacts of GDL permeability on the pressure drop in the fully blocked flow channels ((a) fixed through-plane GDL permeability, (b) fixed in-plane GDL permeability; dry nitrogen was supplied in the experiments)

about 4 % which is acceptable. In addition, in cases of partially narrowed flow fields, the gas flow rate in the GDL is much less than the flow rate of the present experimental condition, so that the Darcy equation is appropriate to estimate the flow rate inside GDL.

According to the results, when the GDL permeability in the thickness direction is fixed, the GDL permeability in the thickness direction was 1.28×10^{-11} m^2, which extremely approaches to the literature value shown in Table 3.1. On the other hand, the impact of the GDL permeability in the thickness direction is nearly unobservable, as shown in Fig. 3.5(b), since merely a small portion of the momentum transport occurs in the GDL thickness direction. Consequently, the literature value of the GDL permeability in the thickness direction presented in Table 3.1 was applied in the simulation.

The polarization curves corrected by IR in case of PN0 were applied to analyze the ORR kinetics. By comparing the varied current densities between experimental and calculated data, the relationship between the partial-pressure-based apparent kinetics constant at RH = 1, $i.e.$ k'_{gc}, and IR-corrected cell voltage can be obtained, shown as the points in Fig. 3.6. Since the mass transport resistances are different in varied flow rates, the ORR kinetics are utilized in fixed flow rates. Fig. 3.6 shows the IR-corrected cell voltage dependency on k'_{gc} which is dependent on the inlet flow rates. The total electrochemical resistance, which can be regarded as $1/k'_{gc}$, exhibits that it is equal to the sum of 3 types of resistances, as expressed by Eq. (3.13). The curve in Fig. 3.6 shows the fitted results calculated by Eq. (3.13).

$$k'_{gc} = \left(1/k^{\circ}_{gc} + 1/k^{*}_{gc} + 1/k^{(I)}_{pO}a_g\right)^{-1} \qquad (3.13)$$
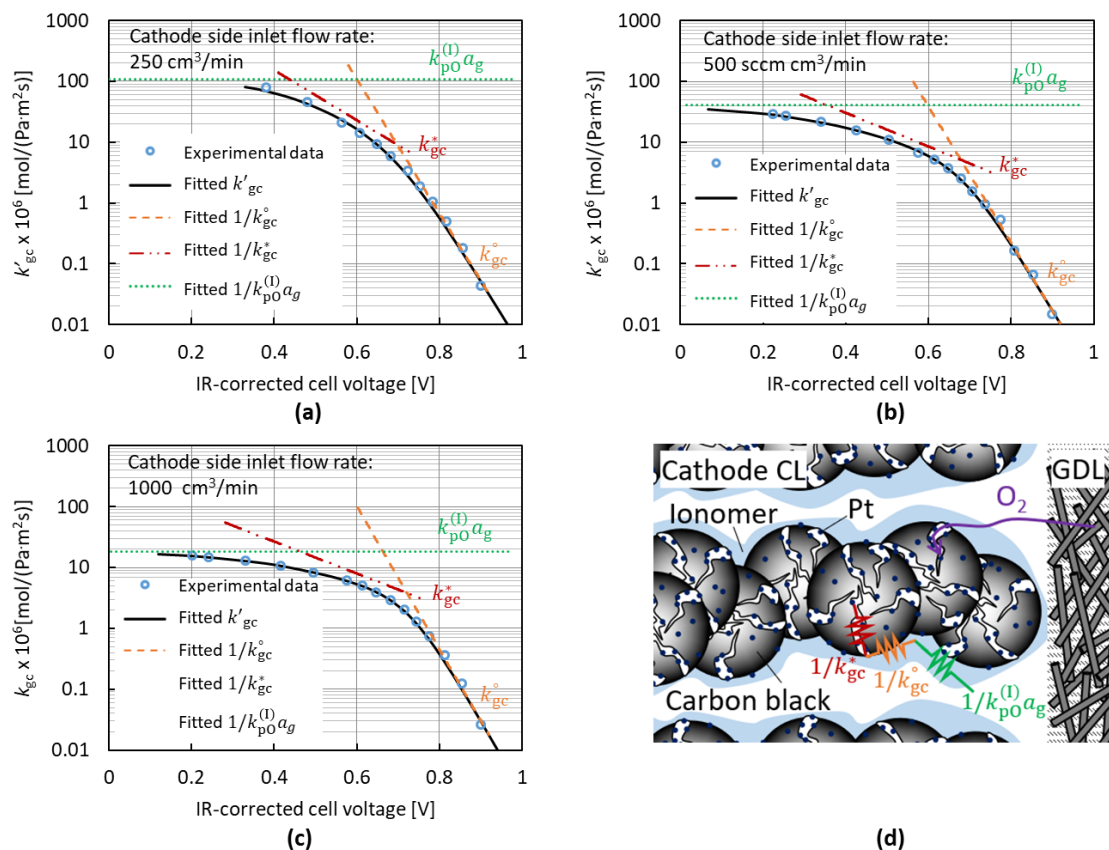
Figure 3.6: ORR kinetics under different flow rate conditions by theory model fitting and oxygen transfer in the cathode CL (flow channel: PN0, humidification temperature 65 $^{\circ}$C, $O_2/N_2 = 0.25$, cathode side inlet flow rate (a) 250 cm^3/min, (b) 500 cm^3/min, (c) 1000 cm^3/min)

$1/k^{\circ}_{gc}$ and $1/k^{*}_{gc}$ represents the electrochemical resistance in primary and secondary pores respectively, which are dependent on the electromotive force[39]. $1/(k^{(I)}_{pO}a_g)$ represents the mass transport resistance in the ionomer, where $k^{(I)}_{pO}$ is the effective oxygen transfer coefficient, and a_g is the electrochemical surface area, which are independent on the electromotive force but the RH[12]. As the oxygen transfer from the GDL to the Pt surface, it will go through the ionomer, primary pores and secondary pores successively, as shown in Fig. 3.6(d), so that the total electrochemical reaction is determined by the 3 processes mentioned above. At the high IR-corrected cell voltage region, the ORR mainly occurs on the Pt surface which is supported on the Ketjen black surface, *i.e.* primary pores' surface, due to the low electrochemical reaction rate limited. As the IR-corrected cell voltage decreasing, the ORR gradually transits to the secondary pores electrochemical reaction rate limited region. At the low IR-corrected cell voltage region, the mass transfer in the ionomer becomes the rate limiting step.

According to the ORR kinetics analysis, the slopes of k^o_{gc} in 3 different flow rates are nearly equal, due to the same types of the CLs. On the other hand, gentler slope of k^*_{gc} is revealed at higher flow rate. In addition, lower $k^{(I)}_{pO} a_g$ can be observed when the flow rate is higher. The phenomenon in these 2 regions can be explained as the worse humidification.
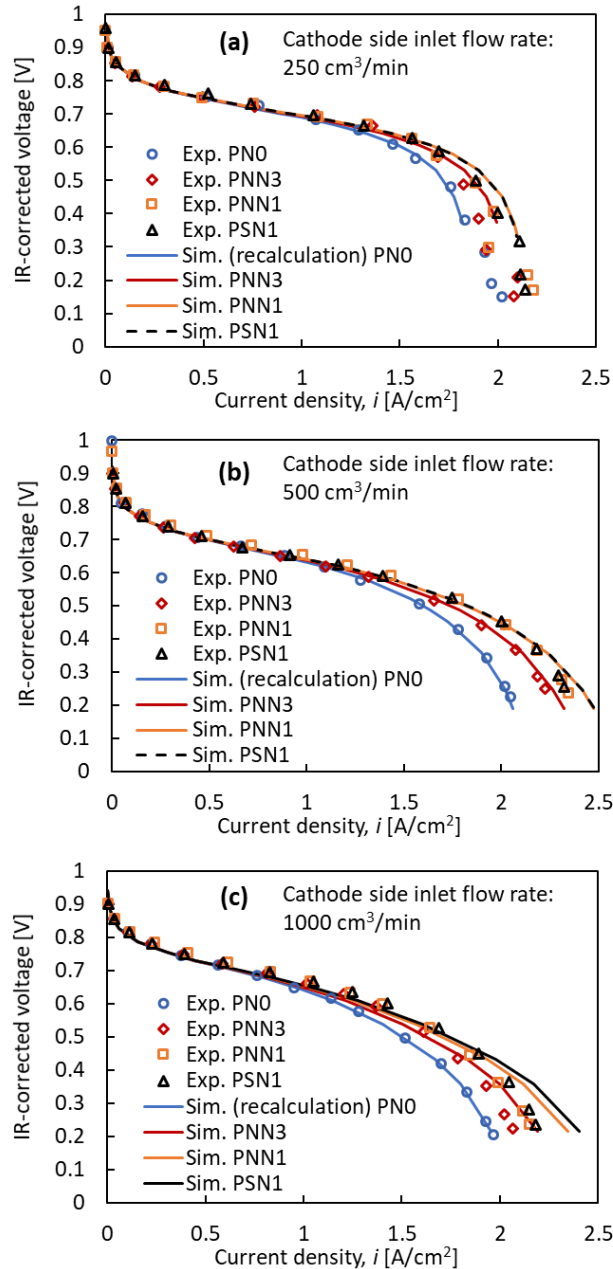
Figure 3.7: Polarization curves of various flow field and flow rates: (a) 250 cm^3/min, (b) 500 cm^3/min, (c) 1000 cm^3/min

3.4.2 Cell performance

By using the ORR kinetics analyzed from the results of PN0 at different flow rates, the polarization curves of PNN3, PNN1, and PSN1 can be calculated by the numerical model. Fig. 3.7 shows the polarization characterization of simulation and experimental results. The simulation reveals a good agreement with the experimental data in each case of the different flow rates, which indicates that the numerical model is able to predict the effects of the different flow fields adequately. Although the current density at low IR-corrected cell voltage of simulation value tends to be slightly (< 7.5 %) higher than that of the experimental value, which means that the performance of the PN0 was underestimated or the performance of other flow fields were overestimated at low IR-corrected cell voltage, the tendency of the performance of each flow field was successfully evaluated. The reason of the derivation may be that some liquid water was locally generated in the GDL, especially where under the rib, at high current density. As a result, the current density at these locations is not as high as estimated in each case of flow fields, and the actual difference between different flow fields is thus less obvious than that of the calculation.
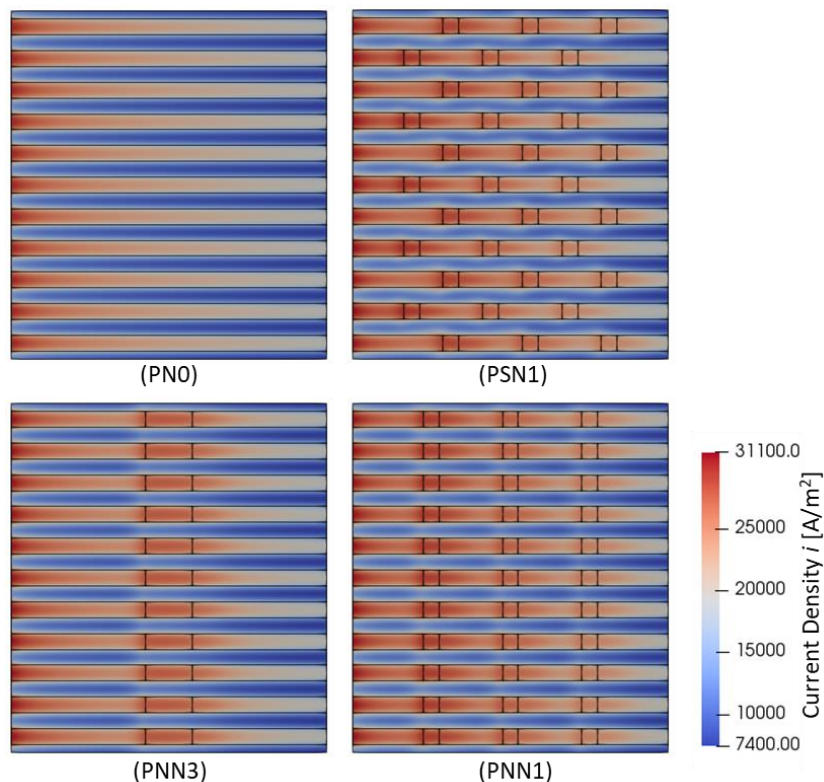

Figure 3.8: Local current density distribution of varied flow channels
(cathode side inlet flow rate: 500 cm^3/min, IR-corrected cell voltage 0.487 V)

Both the experimental and simulated results exhibit that the comparison of performance of each flow field is PSN1 ≥ PNN1 > PNN3 > PN0. The difference of PSN1 and PNN1 depends on the flow rate condition. In case of the high inlet flow rate, *i.e.* 1000 cm^3/min, the performance of PSN1 is slightly better than PNN1. On the other hand, when the inlet flow rate is relatively low, the performances of PSN1 and PNN1 are nearly the same. In addition, in case of the low inlet flow rate, *i.e.* 250 cm^3/min, the polarization curves obtained by experiment are not smooth at high current density. The reason may be that the measurement was unstable due to the liquid water flooding.

The local current density distributions at fixed IR-corrected cell voltage and flow rate of different flow fields calculated by the numerical model are shown in Fig. 3.8, which reveals that the current density is improved near the partially narrowed channels or baffles, comparing to that at the same location of PN0. The improved local current density indicates that the oxygen transfer is enhanced in the GDL under the partially narrowed channel and rib. According to the simulation results, comparing to PNN0, the average oxygen partial pressure on the whole CL surface increases 17.5 %, 17.3 % and 10.8 %, while the total current density increases 14.7 %, 14.3 % and 9.0 %, in case of PSN1, PNN1 and PNN3 at 500 cm^3/min flow rate and 0.487 V IR-corrected cell voltage. In addition, according to the simulation results shown in Fig. 3.8, the current density under the gas channel is 2.3–2.6 times to that under the rib, in case of PN0, under the presented conditions. The effects of flow fields on mass transfer in through-plane and in-plane directions will be discussed from the next section.

3.4.3 Mass transfer in gas channels

Gas flow directions. The cell performance improvement due to the partially narrowed channel can be explained by the enhancement of the mass transport in each separated gas channel. The distributions of the local current density in the gas flow direction at fixed IR-corrected cell voltage and flow rate of varied flow channels are shown in Fig. 3.9.
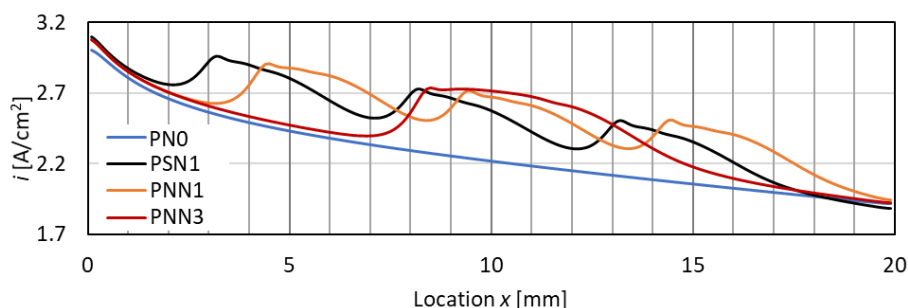

Figure 3.9: Current density distributions of varied flow channels at center section of the middle channel ($y = 11$ mm, coordinate refers to Fig. 3.3, operating conditions as shown in Fig. 3.8)

Along the gas flow direction, the local current density decreases gradually in case of PN0, due to the oxygen consumption. On the other hand, the partially narrowed channels improve the local current density in a range around the narrowed channel. Comparing to PN0, the region where the local current density improves has larger area than the narrowed channel itself. Therefore 2 inferences can be drawn according to this phenomenon:

(1) When relative location among the narrowed channels is fixed, the location of the whole narrowed channel arrangement does not apparently affect the total current in the gas flow direction at a fixed IR-corrected cell voltage. The nearly same performance of PSN1 and PNN1 at 500 cm^3/min flow rate indicates that the effect of the under-rib-convection or cross flow is not obvious at this condition. In addition, PSN1 has the same span between baffles a PNN1 but the different location of baffles in each channel, and the ratios of the current density improvement in PSN1 and PNN1 comparing to PN0 are equal. Therefore, the distance between the gas channel inlet and the baffle has nearly no effect on the performance.

(2) The span among the narrowed channels observably affects the performance, and an appropriate distance is beneficial. When the distance between the narrowed channels is too short, the locations before and behind the narrowed channels where the local current density improved cannot be utilized. Since PNN3 can be regarded as that the distances of narrowed channel of PNN1 are 0, the total area where the local current density improved is smaller than that of PNN1, and PNN3 therefore has worse performance than PNN1 and PSN1.

__Through-plane directions.__ The reason that the current density improved region is larger than the narrowed channel can be attributed to the gas flow distribution in the gas channel. Fig. 3.10 and Fig. 3.11 show the oxygen partial pressure and streamline in the channels and GDL respectively, and 3 effects can be observed.

(1) The narrowed channel improves oxygen concentration on the GDL surface. The oxygen partial pressure tends to be higher near the ceiling of the gas channel and lower near the GDL surface, as shown in Fig. 3.12 (A–A'). When the gas flows into the narrowed channel, the gas in the wider channel flows together and mixes, so that the oxygen partial pressure has more uniform profile in the channel depth direction, as shown in Fig. 3.12 (C–C', (c)). As a result, the oxygen partial pressure at both the GDL and CL surface under the baffle increases[13].

(2) A portion of the gas dives into the GDL at the upstream of the baffle since the gas has a larger flow resistance in the narrowed channel than in the wider channel, as shown
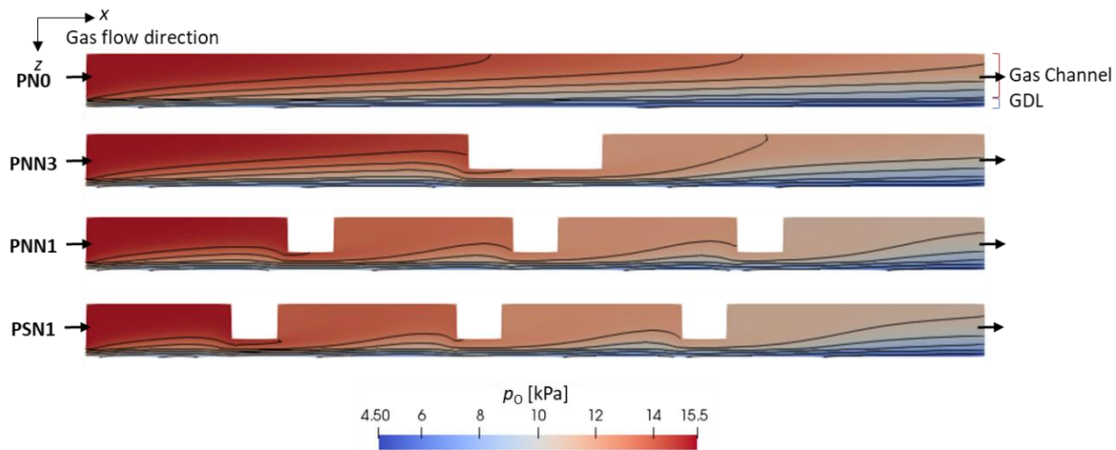
Figure 3.10: Oxygen mole fraction distributions of varied flow channels at center section of the middle channel ($y = 11$ mm, operating conditions as shown in Fig. 3.8)
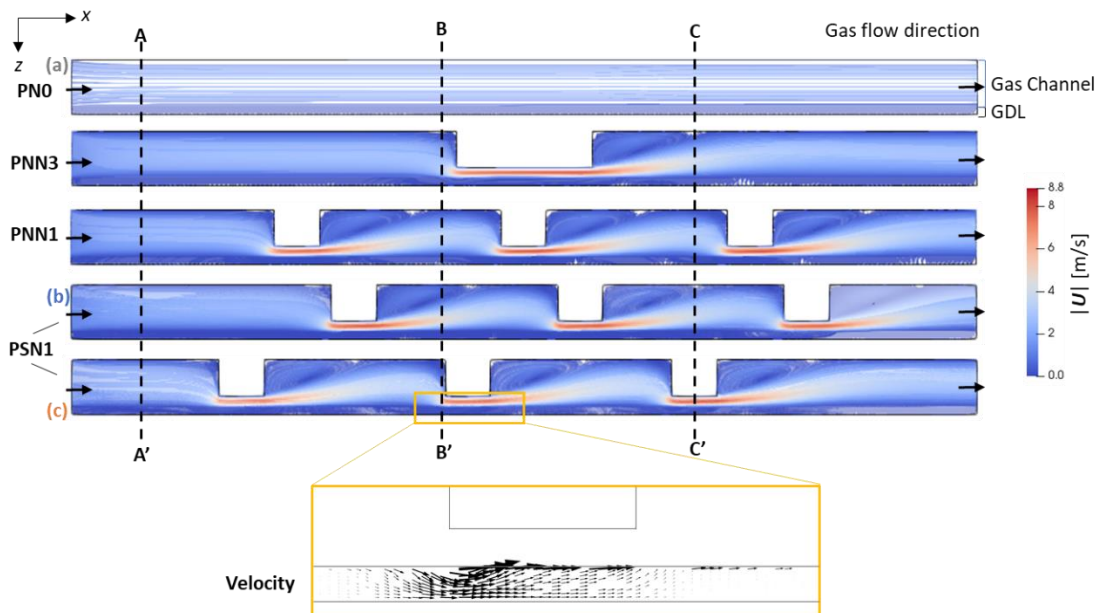

Figure 3.11: Streamline and velocity in the gas channel and GDL ((a) PN0, $y = 11$ mm, (b) PSN1, $y = 12$ mm, (c) PSN1, $y = 11$ mm; A–A': $x = 2$ mm, B–B': $x = 8.2$ mm, C–C': $x = 16.25$ mm; operating conditions as shown in Fig. 3.8. The velocity only in GDL is shown)

in Fig. 3.11, so that the mass transfer in the GDL under the baffle is improved. According to the numerical model, 0.10 % and 0.82 % of the gas flowing in the GDL under the wider channel and baffle respectively, when the total flow rate is 500 cm^3/min and stoichiometry is 7.5, which infers that the baffle remarkably promotes the gas flowing in the GDL.

(3) Due to the suddenly contracted section area of the gas channel, eddies form before and behind the baffles[13], which is also known as the back-flowing region in backward-facing step flow[14]. These eddies dramatically promote the high-oxygen-concentration
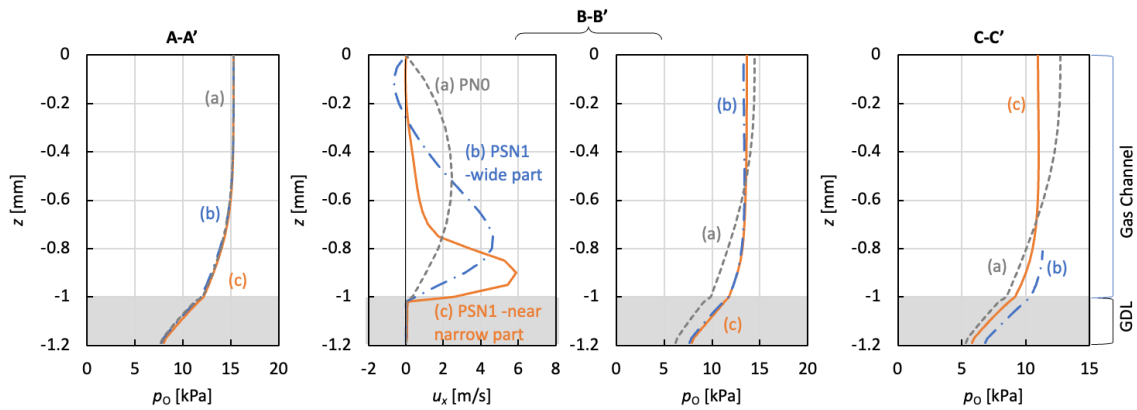
70

Figure 3.12: Distribution of velocity and O_2 partial pressure at center of gas channels ((a), (b), (c), A–A', B–B', C–C' and operating conditions as shown in Fig. 3.8)
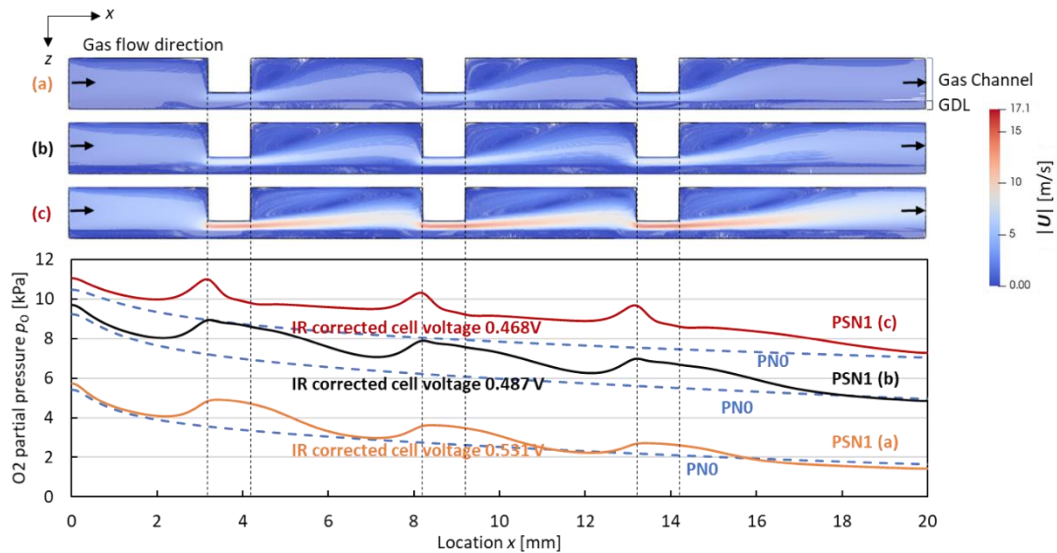

Figure 3.13: Streamlines in the flow fields and oxygen partial pressure profiles on the GDL surface (cathode side inlet flow rate: (a) 250 cm^3/min, (b) 500 cm^3/min, (c) 1000 cm^3/min, $O_2/N_2 = 0.25$, humidification temperature: 65 °C, current density in case of PSN1: 1.9 A/cm^2; data of PN0 at the same IR-corrected cell voltage as PSN1 at each flow rate is shown)

unreacted gas mixing with the low-oxygen-concentration reacted gas in the gas channel, so that the distribution of the oxygen partial pressure is more uniform in the channel depth direction, as shown in Fig. 3.12 (B–B', (b, c)). Hence, the average oxygen partial pressure of partially narrowed channel increases in the GDL under the gas channel where the eddies occur, comparing to PN0. The number of eddies formed in PNN1 and PSN1 is 3 times to that in PNN3, so that the mass transfer and the performance of PNN1 and PSN1 is better than PNN3. Furthermore, although additional pressure drop generates from the

eddy, the improvement in the mass transfer may be more beneficial at some operating conditions.

Operating conditions, especially flow rate, apparently affect the improvement of the mass transfer due to the baffle, which can simultaneously change the eddy in the flow channel and the flow rate in the GDL. At low inlet flow rate, *i.e.*, 500 cm^3/min, although the total current density in case of PSN1 is higher than that of PN0, the current density near the outlet of the PSN1 channel is lower, which indicates the oxygen starvation, as shown in Fig. 3.13. As the inlet flow rate increases, the back-flow region in the channel remarkably expands, the size of which is estimated to be linear to the flow rate in low Reynolds number region[14, 15], so that the current density increased region enlarges. Comparing to PN0, the total current density increases 13.0 %, 14.6 % and 17.6 % when the inlet flow rates are 250 cm^3/min, 500 cm^3/min and 1000 cm^3/min in case of PSN1 at a fixed IR-corrected cell voltage. Therefore, an optimal flow rate condition of partially narrowed flow field exits. However, in the cases of this work, the ratio of mass flow rates in the GDL to that in the flow channels at B–B' section in case of PSN1 are only 0.8 %, 1.4 % and 2.0 %, when the inlet flow rates are 250, 500 and 1000 cm^3/min respectively, at a fixed stoichiometry which is 7.5. It indicates that the effects of the gas flow in the GDL on cell performance in the gas flow direction may be limited in this study, which can be improved by the geometry development.

The effects of the gas flow in the GDL and gas channels also remarkably depend on the geometry of the flow field. Greater number of the baffles and shallower channel promotes the larger amount of the gas diving into the GDL. Shallower channel leads to more uniform oxygen concentration profile in the channel depth direction in the gas channel. Lower ratio of the area of the gas channel and the narrowed channel restrains the eddy in the gas channel, so that the gas mixing in the gas channels is weaker. Furthermore, the baffle design which prevents the eddy forming in the channel has been reported in plenty of literatures[16, 20, 21, 22, 23]. Whereas, the geometry also changed the pressure drops, which may indirectly affect the oxygen partial pressure distribution. In this work, the pressure drop did not observably affect the cell performance due to the small flow fields, so it will not be discussed here.

3.4.4 Mass transfer between adjacent channels

The difference of cell performance between PSN1 and PNN1 can be explained by the mass transfer between adjacent channels, or cross flow. Fig. 3.14 shows the under-channel and under-rib oxygen partial pressure profile in the gas flow direction in cases of PNN1 and PSN1. In case of 500 cm^3/min, the average oxygen partial pressure of both
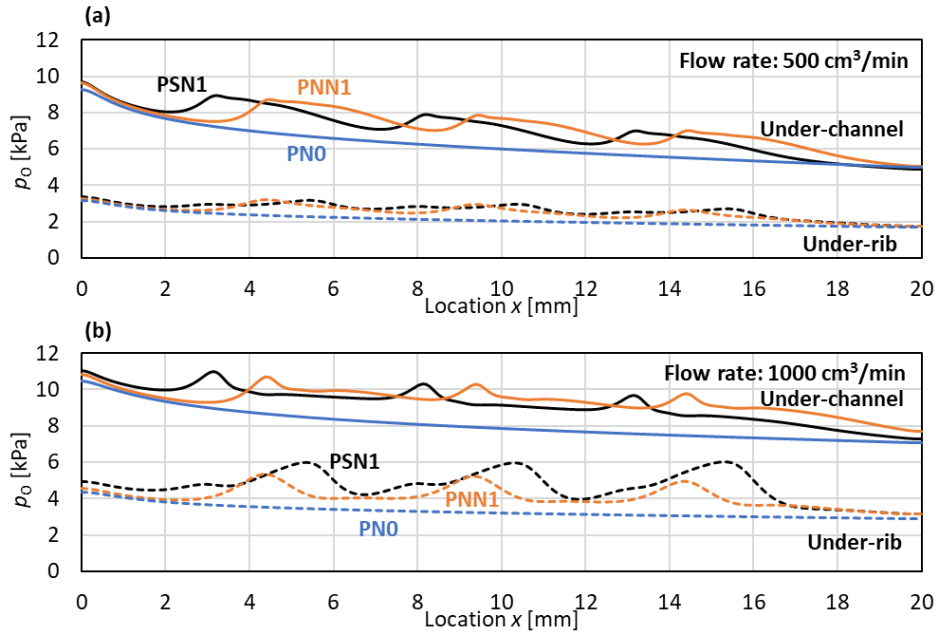
Figure 3.14: Oxygen partial pressure distribution on GDL surfaces (cathode side inlet flow rate: (a) 500 cm^3/min, IR-corrected cell voltage 0.487 V, (b) 1000 cm^3/min, IR-corrected cell voltage 0.468 V. The channel at $y = 11$ mm is shown in case of "under-channel".)

PNN1 and PSN1 are nearly the same, regardless of under-channel or under-rib, which indicates that the effects of cross flow are not obvious. In case of 1000 cm^3/min, the PSN1 has lower average under-channel oxygen partial pressure but higher under-rib oxygen partial pressure than those of PNN1. In other word, only under high flow rate condition, PSN1 generates higher enough cross flow, so that the in-plane oxygen concentration distribution is more uniform. To discuss the effects of the mass transfer quantitively, the in-plane oxygen mass flux profiles were calculated. The oxygen mass flux contains the oxygen mass convection and diffusion, which can be expressed as the first and the second terms in Eq. (3.14) respectively. The orientation of the mass flux is determined by the relative magnitude of the convection and the diffusion.

$$\dot{m}_O = \rho U \omega_O - D_{eO} \rho \nabla \omega_O \tag{3.14}$$

Cross flow in neat-arranged pattern. Generally, in case of near-arranged pattern, the pressure profile in gas flow direction of each gas channel is the same, as shown in Fig. 3.15. In addition, according to the symmetry of the flow field, both the pressure gradient and the mass fraction gradient are zero at the center location of the rib between channels, so that there is no gas exchange between adjacent channels.

At the upstream of the narrowed channel, *e.g.* section D–D' shown in Fig. 3.16, a portion of the reactant gas in the channel dives into the GDL, as mentioned in the previous section, the gas inside the GDL flows not only in the same direction along the channel but multiple directions to the under-rib GDL. In the vertical direction of the gas flow, *i.e.* y direction, the under-channel gas flows to the under-rib GDL. In addition, without the continuously reactant feeding by the gas channel, the under-rib oxygen concentration tends to be lower than that of under-channel, so the orientation of the oxygen mass diffusion is also from the under-channel to the under-rib. Since the convection has the
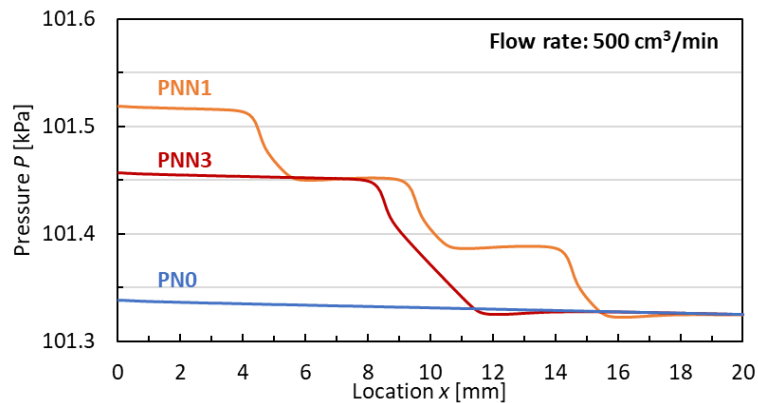

Figure 3.15: Distributions of pressure in each channel of the neat-arranged flow fields (profiles at the center cross section of GDL at $z = 0.95$ mm is shown)
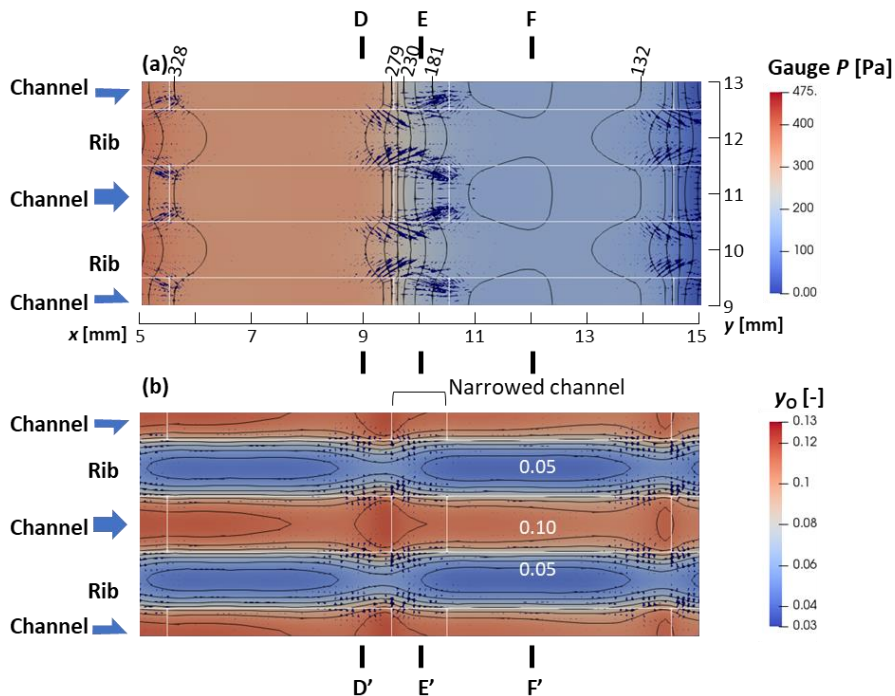

Figure 3.16: Distributions of pressure and oxygen molar fraction in case of PNN1 (profiles at the center cross section of GDL at $z = 0.95$ mm is shown; cathode inlet flow rate 1000 cm³/min; IR-corrected cell voltage 0.468 V)

same orientation as the diffusion, the mass transfer is enhanced, as shown in Fig. 3.17(a) and (d). As a result, the under-rib oxygen partial pressure increases to the local maximum value, as shown in Fig. 3.16 (b).

However, when the gas flows into the narrowed channel, *e.g.* section E–E' shown in Fig. 3.16(a), the lower pressure under-rib than under-channel can be observed. Then, due to the pressure gradient in the GDL under the baffle, the under-rib gas flows back to the under-channel GDL, so that the mass convection has an opposite direction to the mass diffusion, as shown in Fig. 3.17 (b) and (d). The reason can be attributed to the phenomenon which is known as the Venturi effect. When the gas flows through a suddenly narrowed section, due to the Venturi effect as well as the flow friction, the pressure in the narrowed channel abruptly decreased. On the other hand, without the suddenly varied flow field in the GDL, the under-rib gas has lower pressure drop in the
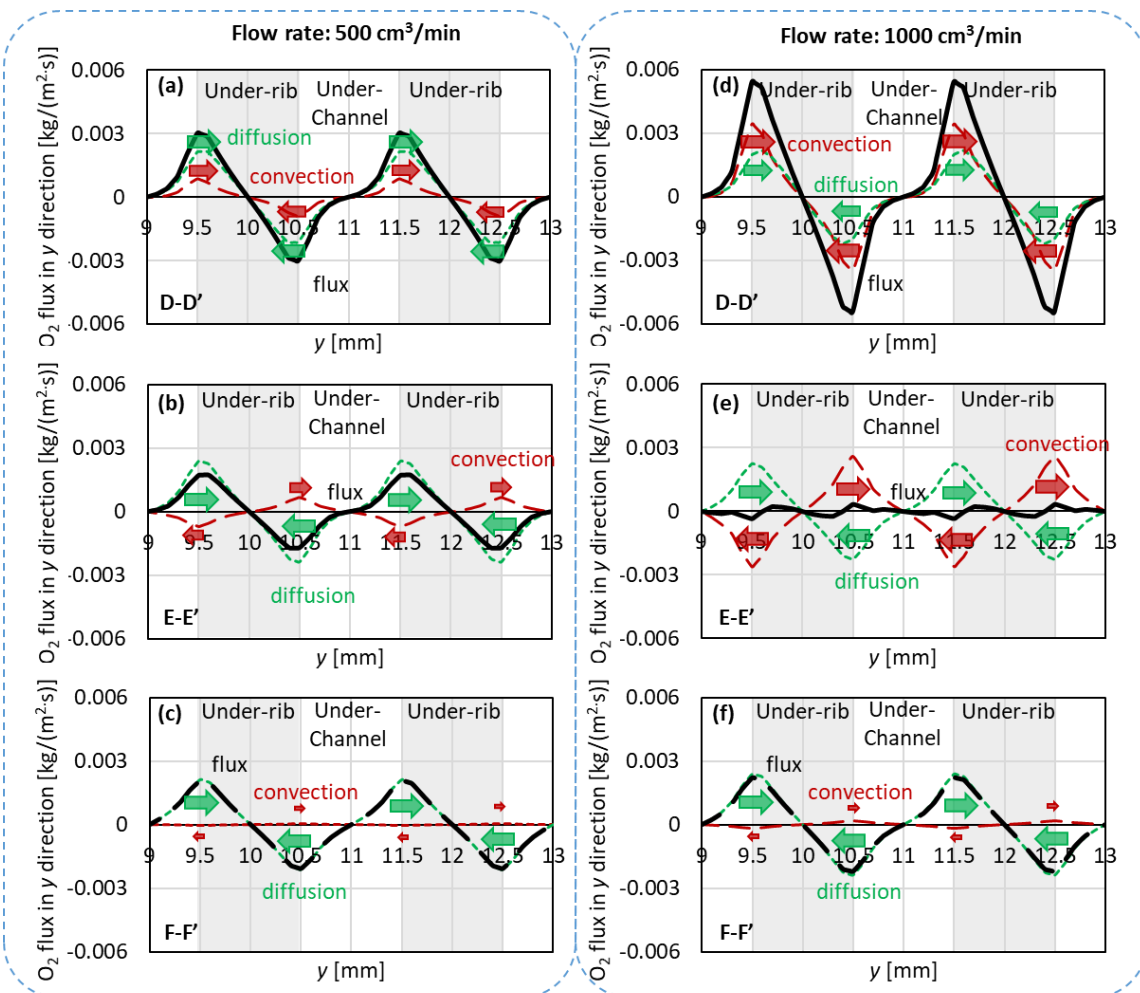

Figure 3.17: Distributions of oxygen mass flux, convection and diffusion in y direction (profiles at the center cross section of GDL at $z = 0.95$ mm is shown; D–D', E–E' and F–F' sections are shown in Fig. 3.16; fixed current density 1.82 A/cm^2)

gas flow direction. Consequently, the under-rib gas is dragged to the narrowed channel. In other words, the mass convection weakens the mass transfer in the GDL, therefore the under-rib oxygen partial pressure decreases from the local maximum value, as shown in Fig. 3.16 (b).

Although the gas flow driven by the gentle pressure gradient between the under-rib and under-channel parts is not remarkable, the mass convection has the same order of the magnitudes to the mass diffusion. At 500 cm^3/min flow rate, the effect of oxygen mass convection at section E–E' is not obvious. However, at 1000 cm^3/min flow rate, the oxygen mass flux is nearly 0, as shown in Fig. 3.17 (d), which means that the Venturi effect apparently affects the mass transfer. Nevertheless, it should be noted that this phenomenon only happens when the gas flows through the suddenly narrowed section. And at other locations where the effect of the baffle is neglectable, *e.g.* section F–F' in Fig. 3.16, nearly no the pressure difference generates between adjacent channels, so the diffusion dominates the mass transfer, as shown in Fig. 3.17 (e) and (f).

Cross flow in staggered pattern. Different from neat-arranged pattern, the pressure profiles in each gas channel of staggered flow channels are different, thus the gas in adjacent channels exchanges with each other alternately, as shown in Fig. 3.18. According to the calculation, the pressure drop mainly generates at the narrowed channel, thus the pressure drop mainly generates at the narrowed channel, thus the cross flow occurs at the downstream of the baffles.

The oxygen mass transfer between adjacent channels is apparently affected by cross flow in case of the PSN1. At section I–I' shown in Fig. 3.19, a large amount of the gas in the odd-numbered channel flows to the even-numbered channel, where the pressure at the former is much higher than that at the latter. When the flow rate is 1000 cm^3/min, the
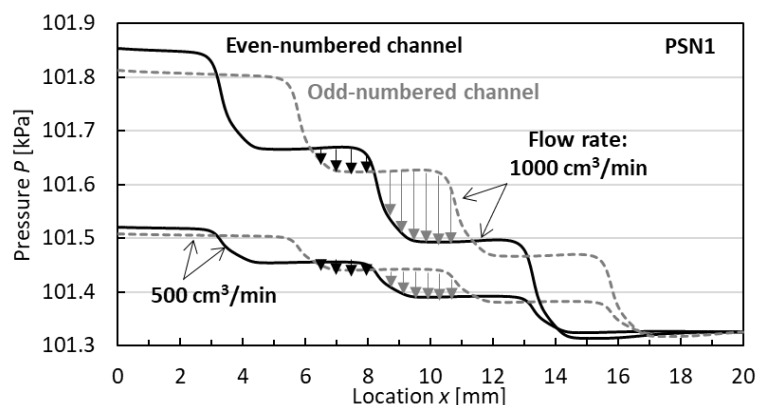

Figure 3.18: Distributions of pressure in the PSN1 flow channels (The arrays show the cross flow between adjacent channels. Profiles at the center cross section of GDL at *z* = 0.95 mm is shown)

oxygen mass convection due to the cross flow is remarkable, so that the total oxygen mass convection is much higher the diffusion, and the oxygen mass flux is thus promoted, as shown in Fig. 3.20 (c) and (f). Consequently, the oxygen mass fraction under the rib exhibits the local maximum value, as shown in Fig. 3.19 (b). Similar phenomenon occurs at section H–H', but the orientation of the cross flow is from the even-numbered channel to the odd-numbered, and the amount is less than that at section I–I'. Therefore, the improvement of mass transfer is less obvious, as shown in Fig. 3.20 (b) and (e).

The Venturi effects also happens in PSN1 flow field, where the pressure difference between the adjacent channels is not obvious, *e.g.* section G–G'. Again, since the opposite orientation of the oxygen mass convection and diffusion, the oxygen mass transfer is weakened, and the oxygen mass fraction exhibits the local minimum value, as shown in Fig. 3.20 (a) and (d). It should be noted that although the oxygen mass convection has the opposite orientation to the diffusion at some locations, the mass transfer is enhanced in the whole in-plane direction.

Nevertheless, the phenomenon mentioned above is not obvious at the flow rate less than 500 cm^3/min under the presented conditions, since the cross flow rate is too low to affect the mass transfer. Table 3.2 exhibits the mass cross flow rate motivated by each single narrowed channel in cases of PSN1 and PNN1 at the fixed stoichiometry. The ratio
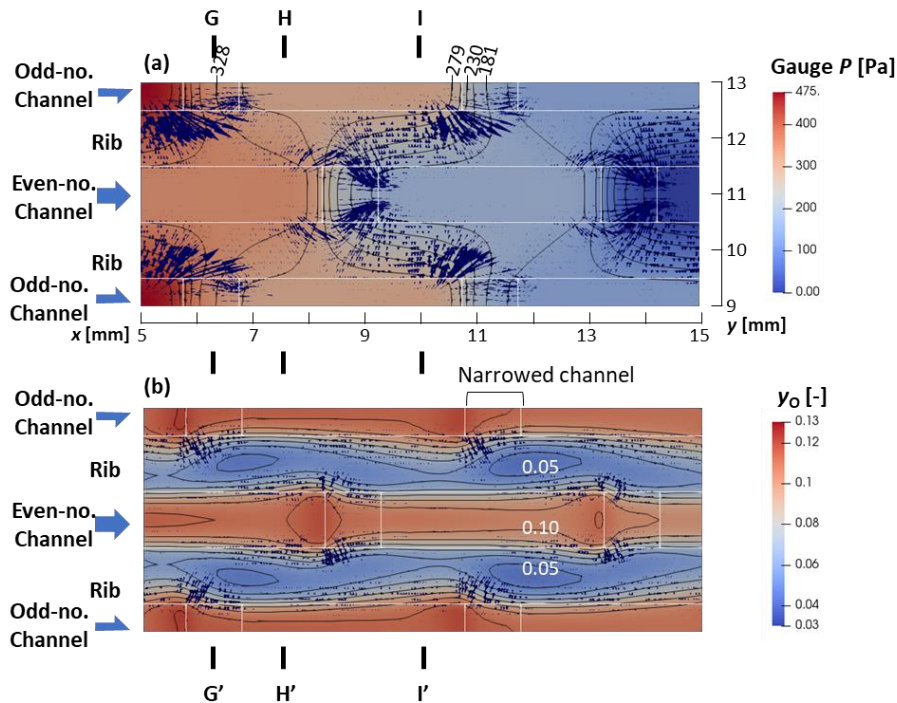

Figure 3.19: Distributions of pressure and oxygen molar fraction in case of PSN1 (profiles at the center cross section of GDL at $z = 0.95$ mm is shown; cathode inlet flow rate 1000 cm^3/min; IR-corrected cell voltage 0.468 V)
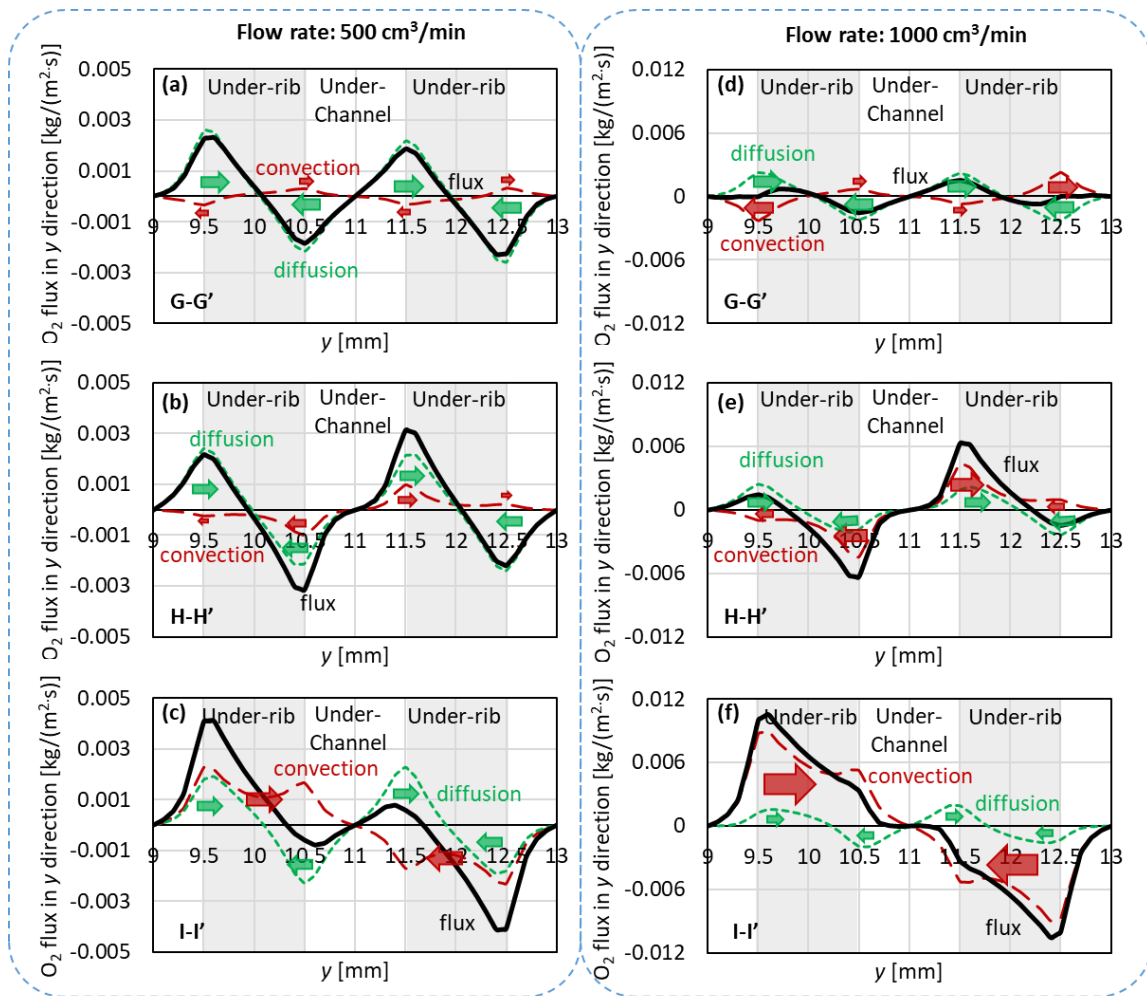
Figure 3.20: Distributions of oxygen mass flux, convection and diffusion in *y* direction (profiles at the center cross section of GDL at *z* = 0.95 mm is shown; G–G', H–H' and I–I' sections are shown in Fig. 3.16; fixed current density 1.86 A/cm^2)

of the cross flow to the channel is tiny, which only increases 10 % when the inlet flow rate increases from 500 to 1000 cm^3/min. Similar oxygen concentration and mass diffusion profiles can be obtained at fixed stoichiometry, whereas the oxygen mass convection is linear to the cross flow rate, and the inlet flow rate directly influences the effects of the cross flow.

Therefore, the main mass transport mechanism is still diffusion under the low flow rate condition, regardless of the neat-arranged or staggered pattern, which explains the reason that the difference of PSN1 and PNN1 is apparent only at 1000 cm^3/min flow rate condition. In addition, the cross flow rate is strongly influenced by the geometry characters, *e.g.* the number of the baffles and the distance between the baffles in the neighboring channels. The optimization of the geometry in order to maximally benefits from the cross flow should be further discussed for future work.
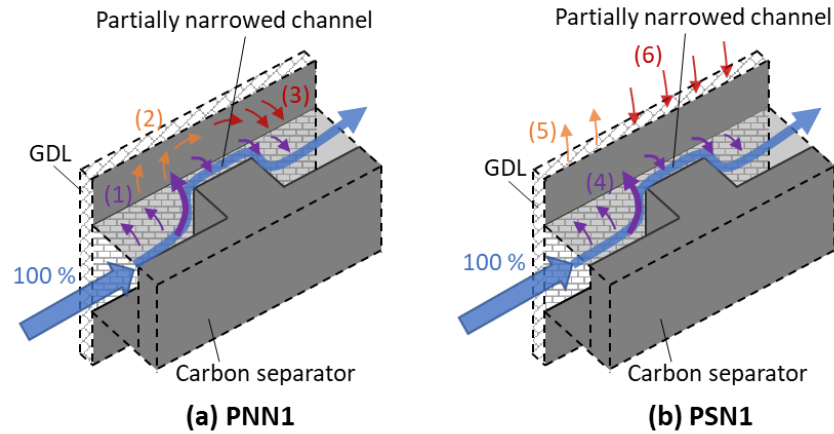
Figure 3.21: Various types of Cross flow around a partially narrowed channel

Table 3.2: Mass flow rate ratio of various cross flow to channel flow near each narrowed channel (fixed stoichiometry: 7.5; the numbers refer to Fig. 3.21)

Inlet flow rate [cm³/min]	PNN1			PSN1		
	(1) Gas diving into the GDL	(2) Under-channel to under-rib	(3) Under-rib to under-channel	(4) Gas diving into the GDL	(5) Gas flowing to the adjacent channel	(6) Gas flowing from the adjacent channel
250	2.80%	0.32%	0.36%	3.20%	0.13%	1.60%
500	3.60%	0.46%	0.50%	4.10%	0.26%	1.90%
1000	4.30%	0.67%	0.69%	4.50%	0.42%	2.10%

3.4.5 Pressure drops

The pressure drop of various flow fields and flow rates at a fixed stoichiometry is shown in Fig. 3.22, in which the experimental data were measured by the pressure gauges at cell inlet and outlet, as shown in Fig. 3.2. The simulation value of pressure drop in the cell inlet and outlet tubing was also solved by the numerical model but without species mass transfer calculation mentioned above. The simulation results reveal a good agreement with the experimental results. Some deviation may origin from the water droplet in the experiment.

The flow field with the narrowed channels have greater pressure drop due to the partially narrowed flow resistance and the eddy. According to the results shown in Fig. 3.22, the pressure drop of PN0 is rather neglectable, comparing to the effects of the cell inlet and outlet tubing. PNN3, PNN1 and PSN1 have the same total length and sections of narrowed channels, thereby they have greater pressure drop than PN0. However, the
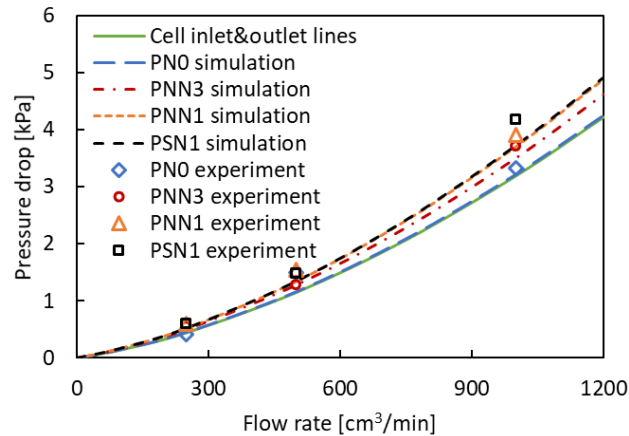
Figure 3.22: Pressure drop at different cathode side inlet flow rate in cases of varied flow fields with cell inlet and outlet lines (fixed stoichiometry: 7.5)
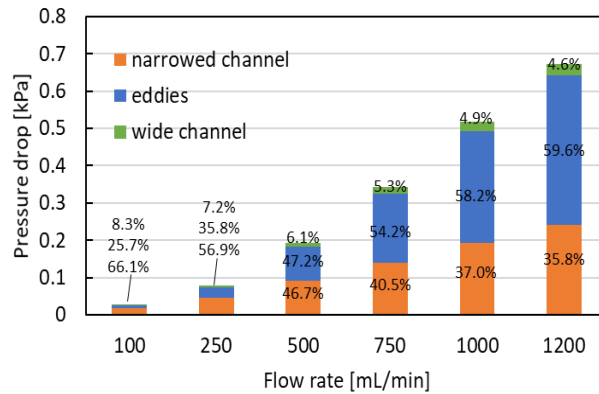

Figure 3.23: Ratio of pressure drop by different influences at different cathode side inlet flow rate in case of PNN1 or PSN1 (except the pressure drop by the cell inlet and outlet lines, fixed stoichiometry: 7.5)

pressure drops of PNN1 and PSN1 are nearly equal but greater than the PNN3, which can be attributed to the eddies in the gas channels. Since the number of the eddies in PNN1 or PSN1 is 3 times to that in the PNN3, more energy is consumed, which causes the local pressure drop. It also indicates that when the total length of the narrowed channel is fixed, the flow filed having greater number of the narrowed channels tends to have greater pressure drop.

By comparing the pressure drops in each case of the flow fields at different flow rates, the pressure drops caused by each factor except the cell inlet and outlet tubing can be estimated, as shown in Fig. 3.23. In case of PNN1 or PSN1, most of the pressure drop can be owed to the narrowed channel sections and the eddies, especially at high inlet flow rate. In addition, since the eddies become larger in a fixed volume of the flow field, larger ratio of the energy of the fluid is consumed, and the pressure drop by this influence
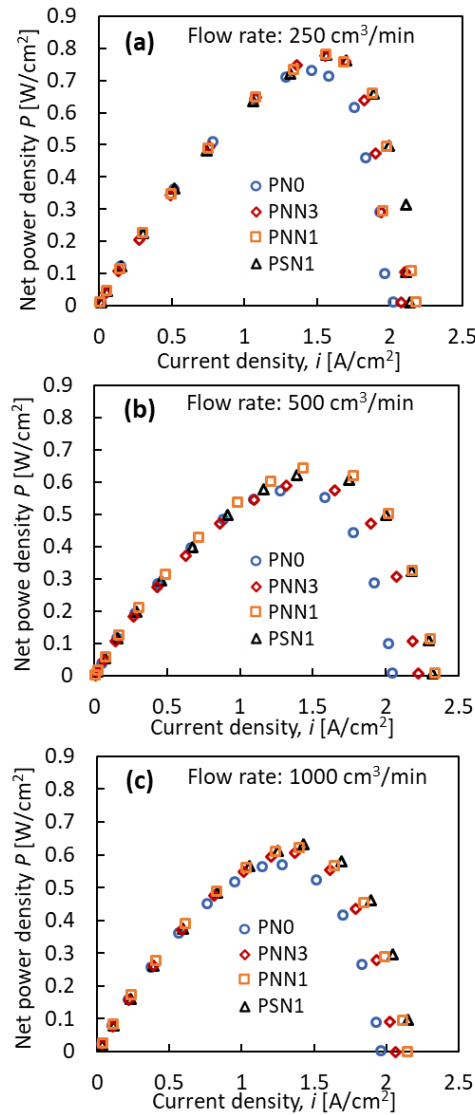
Figure 3.24: Net power density curve of experimental data:
(a) 250 cm^3/min, (b) 500 cm^3/min, (c) 1000 cm^3/min

becomes more remarkable. Despite a great pressure drop is generated by the narrowed channel and eddies, which is 0.32 kPa comparing to the 0.02 kPa of straight parallel flow fields at 750 cm^3/min flow rate, the pressure drop is still acceptable comparing to the pressure drop of the conventional serpentine channel, which is 8.2 kPa comparing to the 0.03 kPa of the parallel flow fields at 700 cm^3/min in 25 cm^2 flow fields, according to calculation results in the literature[16].

The net power density curves of different flow fields obtained from the experimental data were demonstrated in Fig. 3.24. The pumping energy for supplying the reactant gas to the flow fields was calculated from pressure drop, which contains the portion of cell inlet and outlet tubing, by assuming the pump efficiency of 80 %. It should be noted that

the potential energy loss due to the pressure drop is only up to 3.1 % to the total electrical energy generated in case of PSN1 at 1000 cm^3/min, which does not obviously cause the total energy loss. According to the results, the maximum net power density at low flow rate is higher than that at high flow rate, which implies the inadequate humidification at the latter condition. However, the maximum net power density of PSN1 increases 6.6 %, 8.7 % and 11.3 % comparing to PN0 at 250, 500 and 1000 cm^3/min flow rate respectively, which indicates that the cell performance improvement in the partially narrowed flow channel is more obvious at high flow rate, due to the more remarkable effects of cross flow.

3.5 Conclusions

The cell performance and pressure drop of 4 kinds of flow fields, PN0, PNN3, PNN1 and PSN1, were compared and analyzed by experiments and simulations. The ORR kinetics were obtained by experiments. The pressure drops of the fully blocked flow channel under different gas flow rates analyzed by the numerical model exhibited a good agreement with the experimental data and literature value, which indicates the reliability of the momentum transport in the GDL predicted by the model. The numerical model well explained the difference of cell performance between these flow fields, and the diving flow rate and the cross flow rate were also predicted. The transport phenomenon as well as the effects of the diving flow and cross flow were analyzed in this work. The following conclusions can be drawn:

1. The partially narrowed flow fields improves the electrical generation efficiency mainly by increasing the oxygen concentration on the GDL and CL surfaces under the baffles. When the gas flow through the narrowed channel, 2.8–4.5 % of the gas in the channel is forced to dive into the GDL, which promotes the mass convection inside GDL. Moreover, the convergence of the gas in the channel and the eddies forming before and behind the baffles promotes the gas mixing, so that the oxygen concentration on the GDL surface increases. Therefore, an appropriate span between neighboring baffles should be designed to maximally benefit from the gas mixing effects.

2. The gas which dives into the GDL also flows towards the under-rib location and enhances the oxygen mass transfer at the upstream of the baffle. On the other hand, the Venturi effect causes local low pressure in the narrowed channel and draws the under-rib

gas flowing back to the channel, which weakens the local oxygen mass transfer and is unbeneficial to the cell performance, when the gas flowing through the narrowed channel.

3. In cases of the staggered pattern of the partially narrowed flow fields, the cross flow between adjacent channels apparently improves the under-rib convection, so that the in-plane oxygen concentration distribution in more uniform, comparing to the neat-arranged pattern. Although the cross flow rate between adjacent channels is only around 2 % to the gas flow in the channel, the oxygen convection has apparent impacts on the mass transport mechanism, when the inlet flow rate is high enough.

4. Although at cost of the higher pressure drop so that the mass transfer is promoted in cases of the partially narrowed flow fields, they also have better comprehensive performance than the conventional parallel flow fields. The net power density of PSN1 increases up to 11.3 % comparing to the conventional parallel design under the present condition.

Furthermore, the improvement on the cell performance of the partially narrowed flow fields strongly depends on the geometry and operating conditions, whose optimizations should be further discussed. Additionally, a decent liquid water removal performance can be expected owing to high pressure drop and cross flow mentioned above. The estimation of this point should be in the future work.

3.6 Symbols

D_i	Multi-component diffusion coefficient diffusivity of species i	[m/s^2]
D_{ij}	Binary diffusivity of species i and j	[m/s^2]
D_{ej}	Effective diffusivity of species j in the mixture	[-]
$\mathbf{D_K}$	Darcy coefficient tensor	[m^{-2}]
F	Faraday constant	[C/mol]
i	Current density	[A/m^2]
k_{gc}	Reaction rate constant	[mol/(Pa·m^2·s)]
k'_{gc}	Reaction rate constant at RH=1	[mol/(Pa·m^2·s)]
K	Permeability	[m^2]
$\dot{\mathbf{m}}_O$	Oxygen mass flux	[mol/(m^2·s)]
M_i	Molecular weight of species i	[kg/mol]
$\mathbf{n}$	Normal vector of boundary	[-]
p	Partial pressure	[Pa]

P	Total pressure	[Pa]
$-r_{si}$	Surface consumption rate of species i	[mol/(m^2·s)]
R	Molar gas constant	[J/(K·mol)]
T	Temperature	[K]
U	Velocity vector	[m/s]
y_i	Mole fraction of species i	[-]
z	Number of electrons transferred	[-]
$1/k^{\mathrm{o}}_{\mathrm{gc}}$	Electrochemical resistance in primary pores	[Pa·m^2·s/mol]
$1/k^{*}_{\mathrm{gc}}$	Electrochemical resistance in secondary pores	[Pa·m^2·s/mol]
$1/(k^{(\mathrm{I})}_{\mathrm{pO}}\, a_{\mathrm{g}})$	Oxygen transport resistance of ionomer	[Pa·m^2·s/mol]

Greeks

ε	Porosity	[-]
μ	Viscosity	[Pa·s]
ρ	Density	[kg/m^3]
τ	Tortuosity	[-]
ω_i	Mass fraction of species i	[-]

Subscripts

i	Species i
j	Species j
s	Boundary surface of cathode CL and GDL
S	Water steam
N	Nitrogen
O	Oxygen
x	x direction
y	y direction
z	z direction

3.7 References

[1] S. Cruz–Manzo, and R. Chen, *J. Electroanal. Chem.*, **694**, 45–55 (2013).

[2] H. G. Weller, G. Tabor, H. Jasak, and C. Fureby, *Comput. Phys.*, **12**, 620–631 (1998).

[3] J. T. Gostick, M.W. Fowler, M. D. Pritzker, M. A. Ioannidis, and L. M. Behra, *J. Pow. Sour.*, **162**, 228–238 (2006).

[4] M. E. Hannach, and E. Kjeang, *J. Electrochem. Soc.*, **161**, F951–F960 (2014).

[5] D. A. G. Bruggeman, *Ann. Phys. (Leipz.)*, **24**, 636–664 (1935).

[6] S. B. Beale, H. Choi, J. G. Pharoah, H. K. Roth, H. Jasak, and D. H. Jeon, *Comput. Phys. Commun.*, **200**, 15–26 (2016).

[7] C. R. Wilke, *Chem. Eng. Prog.*, **46**, 95–104 (1950).

[8] B. E. Poling, J. M. Prausnitz, and J. P. O'Connell, *The Properties of Gases and Liquids*, 5th ed., p. 639, McGraw-Hill (2001).

[9] M. Kawase, K. Yamaguchi, M. Kageyama, K. Sato, and G. Inoue, *ECS Trans.*, **75**(14), 147–156 (2016).

[10] M. Kawase, K. Sato, R. Mitsui, H. Asonuma, M. Kageyama, K. Yamaguchi, and G. Inoue, *AIChE J.*, **63**, 249–256 (2017).

[11] H. Ogawa, M. Kageyama, and M. Kawase, *ECS Trans.*,**104**(8), 45–58 (2021).

[12] T. E. Springer, T. A. Zawodzinski, and S. Gottesfeld, *J. Eleltrochem. Soc.*, **138**, 2334–2342 (1991).

[13] J. Shen, L. Zeng, Z. Liu, and W. Liu, *Int. J. Heat Mass Transf.*, **55**, 811–822 (2019).

[14] B. F. Armaly, F. Durst, J. C. F. Pereira, and B. Schönung, *J. Fluid Mech.*, **127**, 473–496 (1983).

[15] T. Lee, and D. Mateescu, *J. Fluids Struct.*, **12**, 703–716 (1998).

[16] G. Inoue, Y. Matsukuma, and M. Minemoto, *J. Pow. Sour.*,**157**, 136–152 (2006).

Chapter 4

Operating Conditions in Hydrogen Recirculation System

4.1 Introduction

The water management is of vital importance to achieve maximum performance and durability of PEFC[1]. As mentioned in the previous chapters, the PEM should be maintained in an appropriate hydration to reduce the ohmic loss in PEM and proton and oxygen transport resistance in CL, meanwhile the flooding should be avoided to prevent cell performance deterioration. On the other hand, the water transport as well as the cell performance can be affected by factors such as gas flow pattern[2] and reactant conversion[3], which can affect the distribution of temperature, pressure, composition, electrical potential *etc.* in the cell, especially when the current density is high.

PEFCs generally use hydrogen recirculation operation in commercial applications. The cell can be humidified by the water produced in the ORR by using the hydrogen recirculation operation, as shown in Fig. 4.1, where the subscripts S, O, N represent water vapor, oxygen, nitrogen, respectively. In addition, when all of the anode outlet gas recycles to the inlet, the overall hydrogen utilization can be 100 % and hydrogen loss can be effectively avoided. The external humidifier can be removed by this operation so that the space and the cost of the PEFC system can be reduced. The experimentally optimal parameters such as the recirculation flow rate and the GDL structure[4,5] of the PEFC system have been reported. However, the effects and mechanisms of parameters such as gas flow pattern and one-pass conversion for the PEFC system with hydrogen recirculation was lack of the report.
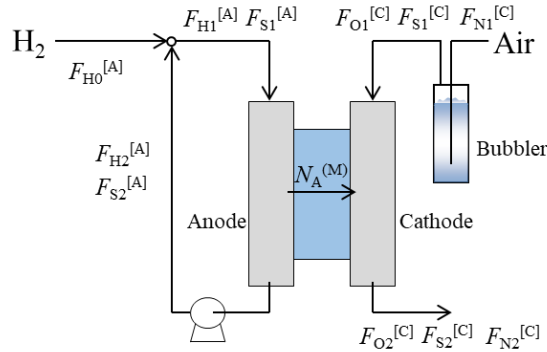
Figure 4.1: PEFC system with hydrogen circulation

The purpose of this study is to elucidate the effects of gas flow pattern and one-pass conversion on the performance of a PEFC system with hydrogen recirculation in different humidifying conditions in a perspective of chemical reaction engineering. The distribution of properties such as oxygen partial pressure, proton conductivity, PEM moisture content, the water transport, and current density were calculated by isothermal $1 + 1$-dimension $(1 + 1D)$ model for optimizing the operating conditions. The conclusion may offer an effective operation method for PEFC system and promote the commercialization of PEFC.

4.2 Numerical Models

In this study, the PEFC system is assumed to be in steady state. The cell is regarded as isothermal since the temperature difference in thickness direction is not great[6]. Water only exists in vapor phase when the RH is less than 1. Dried make-up H_2, whose supplying rate is equal to its consuming rate, is mixed with anode outlet gas and fed to anode inlet. Synthetic air (consists 20.95 % O_2 and 79.05 % N_2, mole fraction), which has 0.5 times O_2 molar flow rate of H_2 flow rate of anode inlet, is humidified by a bubbler and fed to cathode.

The $1 + 1D$ model was applied in this work, in which the properties are considered to have distributions in two directions, the gas channel direction and the MEA thickness direction. The gas channel was regarded as a straight line, so that phenomenon in the in-plane direction could be analyzed in 1D. The processes including air, hydrogen, water, and proton transport and ORR in the CLs, GDLs, PEM at each position in the gas channel were analyzed by combined model in MEA thickness direction. Additionally, the

competition of reaction and mass transfer in cathode CL (CCL) was analyzed and solved by dimensionless model[7]. Without solving partial differential equations mentioned in previous chapters, this 1 + 1D model is thus less computationally expensive comparing to 3D simulation.

4.2.1 Gas channel direction

Gas channels are regarded as straight lines and the gas flow inside is a plug flow. When the gas flows in anode and cathode sides are the same direction, the flow pattern is called co-current. When the gas flows in anode and cathode sides are the opposite directions, the flow pattern is called countercurrent, as shown in Fig. 4.2. The distribution of flow rate along the gas channel can be expressed as Eqs. (4.1) and (4.2) according to the material balance in steady state in case of co-current operation.

$$dF_H^{[A]} = -\frac{i}{2F}A_h dl \tag{4.1}$$

$$dF_O^{[C]} = -\frac{i}{4F}A_h dl \tag{4.2}$$

$$dF_S^{[A]} = -N_A^{(M)}A_h dl \tag{4.3}$$

$$dF_S^{[C]} = (\frac{i}{2F} + N_A^{(M)})A_h dl \tag{4.4}$$

In the equations, i is the current density [A/m^2], A_h is the electrode area per unit length of the gas channel [m^2/m], F_S, F_H and F_O are water, H$_2$ and O$_2$ molar flow rate [mol/s] respectively. Superscripts [A] and [C] represent anode and cathode gas channels. F is Faraday constant [C/mol]. $N_A^{(M)}$ is the water permeation flux through PEM [mol/(m^2·s)], which is defined to have a positive direction from anode to cathode side. In case of the countercurrent, the right sides of Eqs. (4.1) and (4.3) are positive.
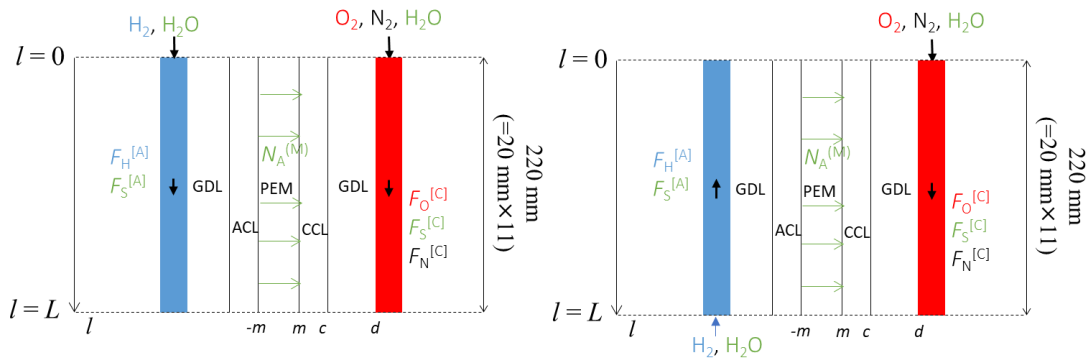

Figure 4.2: Gas flow direction model (left: co-current, right: countercurrent)

Although $N_A{}^{(M)}$ has a distribution in the gas channel direction, the total water permeation rate is 0 according to the material balance since the make-up H_2 fed into the system is dry and no water produced in anode side in steady state, as expressed by Eq. (4.5).

$$\overline{N}_A^{(M)} = \frac{1}{L} \int_0^L N_A^{(M)} dl = 0 \tag{4.5}$$

4.2.2 MEA thickness direction

PEM Model. In this study, gas crossover through PEM is neglected, so that only water and protons can transfer through the PEM. $N_A{}^{(M)}$ counts 2 different water transport mechanisms, _i.e._, the electroosmosis and back diffusion, as expressed by Eq. (4.6).

$$N_A^{(M)} = a_A \frac{i}{F} - D_{eA}^{(M)} c^{(M)} \rho^{(M)} \frac{d\lambda}{dz} \tag{4.6}$$

The electroosmosis drag coefficient a_A is assumed as 1 mol-H_2O/mol-H^+. The effective H_2O diffusivity in PEM, $D_{eA}^{(M)}$ [m^2/s], the ion exchange capacity of PEM, $c^{(M)}$ [mol-SO_3H/kg-Nafion] and the PEM density, $\rho^{(M)}$ [kg/m^3] are regarded as constants, so that the moisture content of PEM, λ [mol-H_2O/mol-SO_3H] has a linear distribution in the PEM thickness direction. The equilibrium moisture content at catalyst layer–GDL boundaries are assumed and calculated by Springer's equation expressed by Eq. (4.7), where a is the water vapor activity which can be regarded as the gas RH. The proton conductivity, $\sigma_p^{(M)}$ [S/m] is a function of λ expressed by Eq. (4.8)[7] when the temperature is 80 °C.

$$\lambda = 0.043 + 17.81a - 39.85a^2 + 36.0a^3 \tag{4.7}$$

$$\sigma_p^{(M)} = 0.931044\lambda - 0.590621 \text{ [S/m]} \tag{4.8}$$

Cell voltage, V [V], is assumed to have a uniform and constant distribution in the plane. Electron conductivity is assumed to be neglected comparing to the proton conductivity, so that PEM resistance $R^{(M)}$ [$\Omega \cdot$cm^2] is only determined by $\sigma_p^{(M)}$ expressed by Eq. (4.9) where the subscripts _-m_ and _m_ represent anode CL–PEM and PEM–CCL boundaries respectively, and IR corrected cell voltage E_{cm} [V] can be calculated by Eq. (4.10)[7].

$$R^{(M)} = \int_{z_{-m}}^{z_m} \frac{1}{\sigma_p^{(M)}} dz \tag{4.9}$$

$$E_{cm} = V + iR^{(M)} \tag{4.10}$$

CCL Model. Local current density i is calculated from Eqs. (4.10) – (4.11), where k_{vcm} is the 1st-order cathode reaction rate constant per layer volume [mol/(Pa·m^3·s)], p_{Oc} is the

partial pressure of oxygen at the CCL–GDL boundary [Pa], and F_e is the effectiveness factor of the CCL which represents the ratio of observed rate to intrinsic rate, $k_{vcm}p_{Oc}$. ρ_b is the platinum loading per unit layer volume [kg-Pt/m^3]. $k_{mc}^\oplus$ is the reaction constant at emf = 0 per unit platinum mass [mol/(Pa·kg-Pt·s)]. b_c is the Tafel slope [V] of the ORR.

$$i = 4F\delta^{(C)}k_{vcm}p_{Oc}F_e \tag{4.10}$$

$$k_{vcm} = k_{mc}^\oplus \rho_b \exp(-E_{cm}/b_c) \tag{4.11}$$

F_e is determined by only 4 dimensionless moduli M_{Om}, M_{pm}, P_{Om} and y_{Oc} [7]. y_{Oc} represents the oxygen mole fraction at the CCL–GDL boundary. M_{Om} represents the ratio of oxygen diffusion resistance to ORR resistance (Thiele modulus). M_{pm} represents the ratio of proton transport resistance to ORR resistance (our modulus). P_{Om} represents the ratio of the convection to the oxygen diffusion (Péclet mumber). The definition of M_{Om}, M_{pm} and P_{Om} are expressed by Eqs. (4.12) – (4.14), where N_{gm} is the total gas flux at the PEM–CCL boundary [mol/(m^2·s)] which equals to $N_A^{(M)}$ when crossover through PEM is neglected, C_g is the total gas molar concentration [mol/m^3], $D_{eO}^{(C)}$ is the effective oxygen diffusion coefficient [m^2/s], $\delta^{(C)}$ is the thickness of CCL. $\sigma_{ep}^{(C)}$ is the effective proton conductivity [S/m] in the CCL, which is assumed to be ε_I^2 times to $\sigma_p^{(M)}$, where ε_I is the ionomer volume fraction.

$$M_{Om} = \delta^{(C)}\sqrt{\frac{k_{vcm}RT}{D_{eO}^{(C)}}} \tag{4.12}$$

$$M_{pm} = \delta^{(C)}\sqrt{\frac{4Fk_{vcm}p_{Oc}}{\sigma_{ep}^{(C)}b_c}} \tag{4.13}$$

$$P_{Om} = \frac{\delta^{(C)}N_{gm}}{C_g D_{eO}^{(C)}} \tag{4.14}$$

GDL Model. The distribution of the oxygen mole fraction, y_O, exists in the GDL due to its diffusion from the gas channel to the CCL. In this study, the total pressure drop through the GDL is assumed 0. According to the oxygen conservation and Fick's diffusion law in the GDL thickness direction, Eqs. (4.15) – (4.16) and boundary conditions (4.17) – (4.18) can be attained. The effective O$_2$ diffusivity in the GDL, $D_{eO}^{(D)}$ [m^2/s], is assumed constant. N_g is the total gas flux [mol/(m^2·s)]. N_O represents the oxygen flux through GDL [mol/(m^2·s)] which is proportional to the oxygen consumption rate and the current density as expressed in Eq. (4.16). The subscripts c and d represent the CCL–GDL boundary and the GDL–gas channel boundary respectively.

$$\frac{dN_O}{dz} = 0 \tag{4.15}$$

$$N_O = N_g y_O - C_g D_{eO}^{(D)} \frac{dy_O}{dz} = -\frac{i}{4F} \tag{4.16}$$

$$\text{B.C.} \quad y_O = y_{Oc} \quad @ \quad z = z_c \tag{4.17}$$

$$\text{B.C.} \quad y_O = y_{Od} \quad @ \quad z = z_d \tag{4.18}$$

By solving Eqs. (4.6) – (4.18), the distribution of the oxygen flux, the oxygen partial pressure, the electrical potential in MEA thickness direction, and the local current density can be obtained. By solving Eqs. (4.1) – (4.5), the distributions of the local current density, the gas flow rate, the ohmic resistance and $N_A^{(M)}$ in the gas channel direction can be obtained. The parameters used in the numerical simulation are listed in Table 4.1.

Table 4.1: Parameters used in numerical simulation

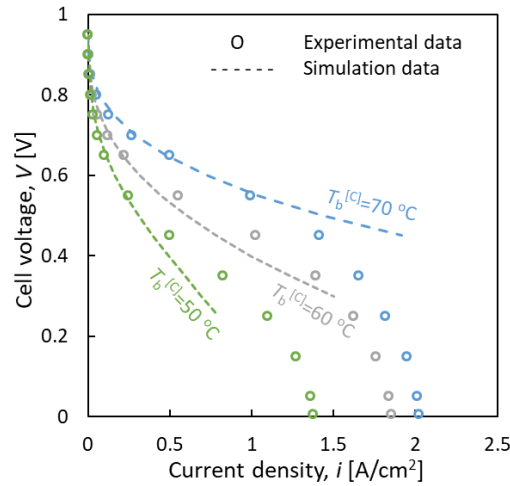| Variable	Symbol	Value
CCL thickness	$\delta^{(C)}$	0.000015 m
Effective O_2 diffusivity in CCL[8]	$D_{eO}^{(C)}$	3.61×10^{-7} m²/s
Ionomer volume fraction	ε_I	0.21
Platinum loading per unit layer volume	ρ_b	289 kg-Pt/m³-CCL
GDL thickness	$\delta^{(D)}$	0.00019 m
Effective O_2 diffusivity in GDL	$D_{eO}^{(D)}$	0.000018 m²/s
Electrode area per unit length of gas channel	A_h	0.0004/0.22 m²/m
Effective H_2O diffusivity in PEM[9]	$D_{eA}^{(M)}$	8.8×10^{-10} m²/s
PEM density	$\rho^{(M)}$	2000 kg/m³
Ion exchange capacity of PEM	$c^{(M)}$	0.91 mol-SO₃H/kg-Nafion
PEM thickness	$\delta^{(M)}$	0.0000508 m
Electroosmosis coefficient	a_A	1 mol-H₂O/mol-H⁺
Reaction constant at emf = 0 per unit platinum mass	$k_{mc}^{\oplus}$	(70 ºC ≤ T_b < 80 ºC) 3.86×10^6 mol/(Pa·s·kg-Pt)
		(65 ºC ≤ T_b < 70 ºC) 8.03×10^5 mol/(Pa·s·kg-Pt)
		(60 ºC ≤ T_b < 65 ºC) 1.43×10^4 mol/ Pa·s·kg-Pt)
		(50 ºC ≤ T_b < 60 ºC) 21.9 mol/(Pa·s·kg-Pt)
Tafel slope	b_c	(70 ºC ≤ T_b < 80 ºC) 0.0313 V
		(65 ºC ≤ T_b < 70 ºC) 0.0327 V
		(60 ºC ≤ T_b < 65 ºC) 0.0378 V
		(50 ºC ≤ T_b < 60 ºC) 0.0515 V

Figure 4.3: Polarization curves at different humidification temperature (humidification temperature of anode and cathode are the same, gas flow direction: co-current, inlet flow rate at 101.325 kPa on dry basis: anode H_2 200 cm^3/min, cathode O_2 100 cm^3/min + N_2 100 cm^3/min, 20 °C)

4.2.3 Model evaluation

The numerical model was verified by comparing with the experimental data. Fig. 4.3 shows that the results measured and calculated at varied humidified temperature in case of the co-current gas flow direction. The parallel flow channel was applied in the experiment. The results demonstrate that the simulation data shows a good agreement with the experimental data at high cell voltage regions, which is higher than 0.55 V. The results indicate that the Tafel slope and reaction constant applied in the Table 4.1 offer high reliability in the low current density region, where the mass transport resistance is not remarkable, and the cell should be operated in this region[10]. On the other hand, the deviation in the high current density region may result from the underestimation of the mass transport resistance in the experiment due to the flooding at 70 ˚C of humidified temperature, and the overestimation of the mass transport resistance in the simulation which offered the non-intrinsic reaction constant.

4.3 Results and Discussion

4.3.1 Effects of gas flow direction on cell performance

The distributions of current density, RH and water permeation flux for the different gas flow directions at the identical total current density and the one-pass conversion
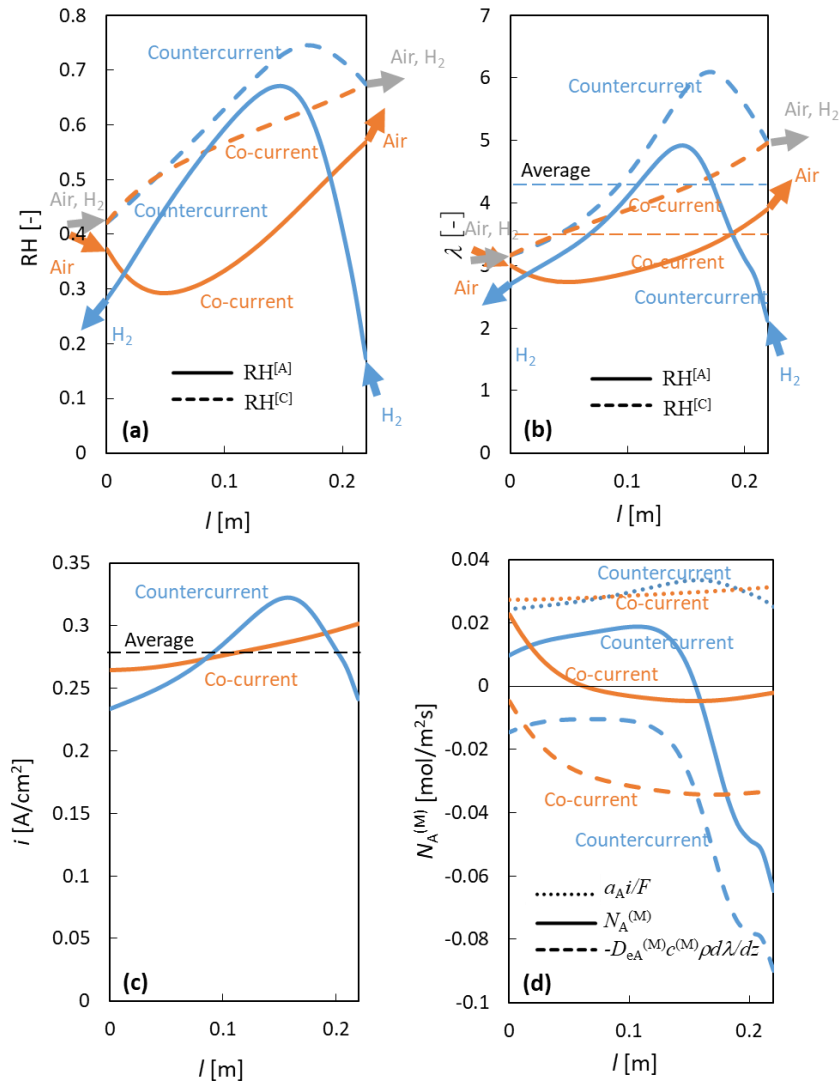
Figure 4.4: Distributions of (a) relative humidity, (b) PEM moisture content, (c) current density and (d) water permeation flux in a PEFC system with hydrogen circulation (current density = 0.280 A/cm^2, one-pass conversion = 0.42, $F_{H1}^{[A]}/F_{O1}^{[C]}$=2, bubbler temperature: 60 ˚C)

conditions are shown in Figs. 4.4 and 4.5. In case of the co-current, near the inlet of the cell, the RH of both anode and cathode is relatively low, and the back diffusion flux is also low. As a result, water transfers from anode to cathode since the electroosmosis is relatively greater than the back diffusion. On the other hand, near the outlet of the cell, due to the consumption of reactant gas and the generation of water in ORR, the RH of both anode and cathode is relatively high, especially cathode. As a result, the back diffusion flux becomes greater and more water in drawn back to the anode side.
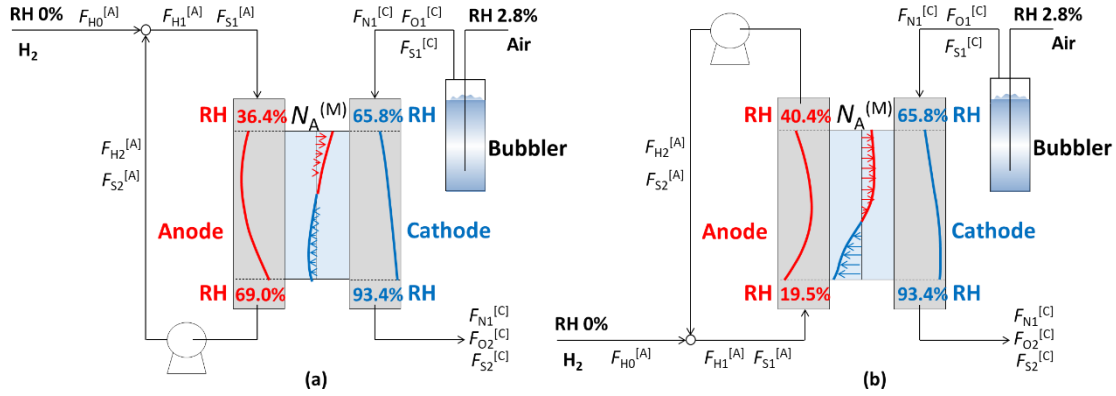
Figure 4.5: RH and $N_A^{(M)}$ distributions in a PEFC system with hydrogen circulation ((a) co-current, (b) countercurrent, current density = 1.43 A/cm^2, one-pass conversion = 0.57, $F_{H1}^{[A]}/F_{O1}^{[C]}$=2, bubbler temperature: 70 °C)

However, in case of the countercurrent, the RH at the anode inlet is relatively low and the RH at the cathode outlet is relatively high, the back diffusion flux is much greater than that in case of the co-current. As a result, a critical point exists, where the RH in both anode and cathode, as well as the current density, reach the maximum, as shown in Fig. 4.4(a)–(c). Therefore, although the total water permeation rate through the PEM is 0 in two cases, $N_A^{(M)}$ distribution in case of the co-current is more uniform and the RH in cathode increases monotonically. On the other hand, in case of the countercurrent, $N_A^{(M)}$ distribution is less uniform and RH in cathode tends to have a maximum value at a certain position.

In addition, when the total current and the one-pass conversion are determined, the outlet RH of the cathode side is determined as well, which can be calculated by Eq. (4.19) when the total water permeation rate is 0. In Eq. (4.19), y is the mole fraction, I is the total current. Subscripts 1 and 2 represent cell inlet and cell outlet. x_H is the one-pass conversion of hydrogen, which is equal to the oxygen conversion, since the inlet oxygen molar flow rate is 0.5 times of the inlet hydrogen inlet molar flow rate. According to Eq. (4.19), the outlet RH in cathode side is only determined by the inlet condition and one-pass conversion, independently of the gas flow direction. That indicates when the inlet condition and one-pass conversion are identical, the RH in cathode is more likely to exceed 1, which indicated the flooding is more likely to take place, in case of the countercurrent operation, since the maximum RH exists at a certain position in the cathode gas channel.

$$\text{RH}_2^{[C]} = \frac{F_{S1}^{[C]} + \dfrac{I}{2F}}{\left(F_{S1}^{[C]} + F_{O1}^{[C]} + F_{N1}^{[C]} + \dfrac{I}{4F}\right)y_S^{sat}} = \frac{y_{S1}^{[C]} + 2y_{O1}^{[C]}x_H}{(1 + y_{O1}^{[C]}x_H)y_S^{sat}} \tag{4.19}$$
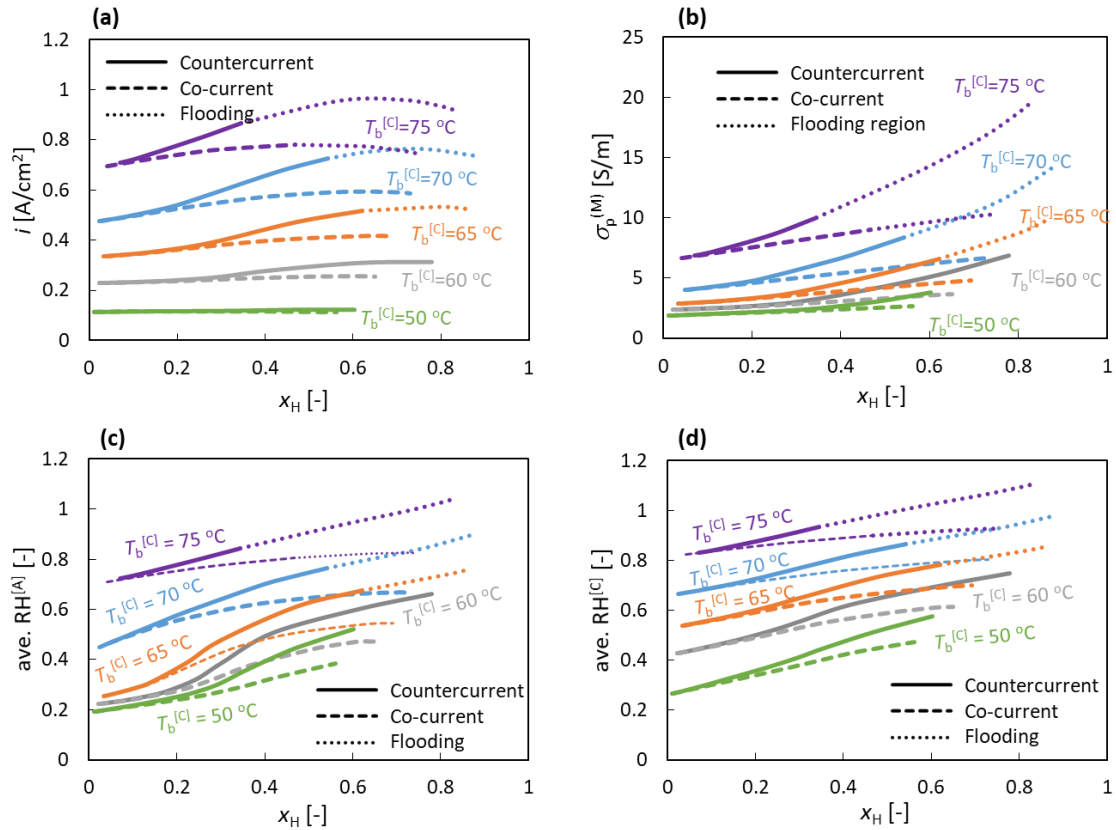
Figure 4.6: Impacts of one-pass conversions on (a) output current density, (b) proton conductivity, (c) average anode RH and (d) average cathode RH (cell voltage = 0.6 V)

At an identical cell voltage of 0.6 V where the model applies high reliability as shown in Fig. 4.3, relationships between the output current density and the one-pass conversion in the different gas flow directions and bubbler temperatures are shown in Fig. 4.6(a). The countercurrent operation exhibits a higher output current density as well as better performance than the co-current operation when the one-pass conversion and the bubbler temperature are high. Additionally, the performances of the countercurrent and the co-current operations are similar when the one-pass conversion and the humidification temperature are low.

The difference can be explained by the PEM hydration. Fig. 4.6(b) – (d) shows the impacts of the one-pass conversion on proton conductivity of PEM and average RH of anode and cathode at fixed cell voltage. The difference in the proton conductivity of PEM, as well as the average RH, between the co-current and the countercurrent operations is not remarkable at low one-pass conversion. When the one-pass conversion is low, the gas flow rate in the gas channel is high at fixed current density, so that the water produced in the ORR cannot humidify the cell sufficiently, and the RH in the gas channels varies in a narrow range. Since the RH distributes uniformly along the gas flow direction, the water
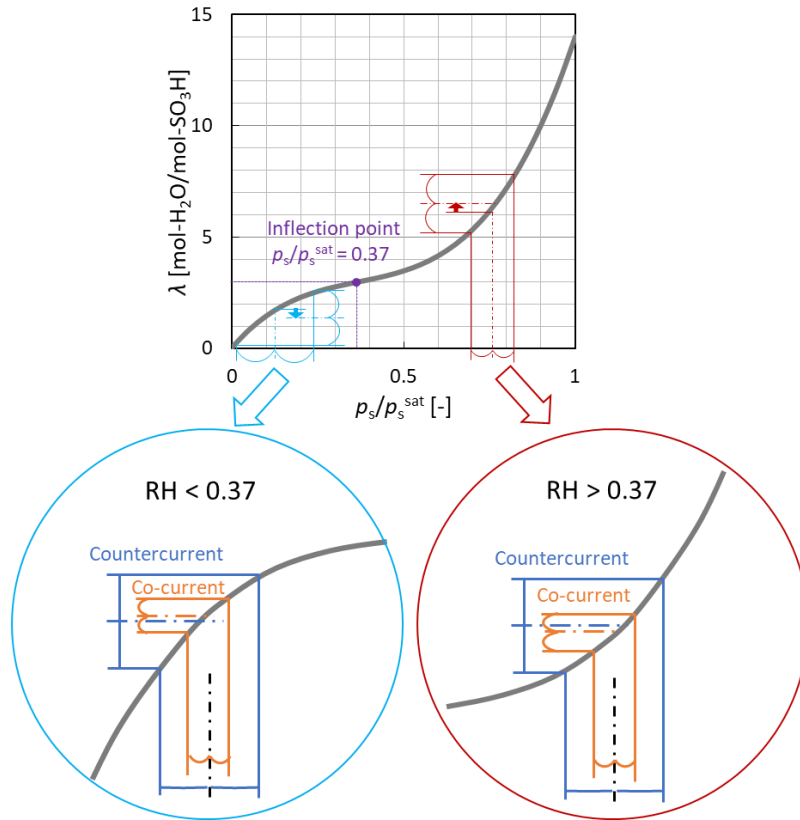
Figure 4.7: Relationship between Nafion membrane moisture content and RH

permeation flux is low in case of both the co-current and countercurrent operations, resulting in little performance difference caused by the difference in the flow directions.

In addition, a low-temperature bubbler cannot humidify the cell as well. The proton conductivity and the current density are low when the cell is not humidified sufficiently, as shown in Fig. 4.6(b). In this situation, less water is produced in ORR and the electroosmosis flux is low. When the bubbler temperature is 50–65 °C, the cathode inlet gas RH is 26–53 %. According to Fig. 4.7, which is plotted by Springer's equation (Eq. (4.7)), in this RH range, the PEM moisture content increases slowly as the RH increases. As a result, although the average RH in the cathode is higher than that in the anode, the gradient of PEM moisture content in the through-plane direction is little, and the back diffusion flux is low as well, according to Eq. (4.6). In summary, the low one-pass conversion and the low bubbler temperature cause the RH and the water permeation distribute uniformly at a low level, so that the difference in the cell performance between the co-current and the countercurrent operations is not remarkable.

The difference of the effects co-current and countercurrent on the cell performance can be explained by the characteristic hydration curve of the Nafion membrane. An inflection

point exists at RH = 0.37, above which the curve is downward convex, below which the cure is downward concave, as shown in Fig. 4.7. The average RH of inlet and outlet of cathode of co-current and countercurrent are nearly the same at fixed current density and conversion. When the humidification temperature is high, since the water permeation distribution along the gas channel is less uniform in case of the countercurrent operation, which means that the maximum RH is higher, and the minimum RH is lower in case of the countercurrent. As the result, the average moisture content of the countercurrent is higher, as shown in Fig. 4.4(b), due to the downward convex curve when the RH is higher than 0.37, the inflection point, so that the proton transfer resistance is lower, and the performance is better. On the other hand, when the RH is lower than 0.37, the co-current operation has higher average moisture content owing to the downward concave curve, so that the performance is better than the countercurrent operation in this region. It should be noted that the average RH should be high enough to maintain a low proton transfer loss, and the generated water humidifies the cell as well, so that the cell is not likely to be operated in the region of RH < 0.37. Therefore, the countercurrent is basically preferable in the actual operation.

4.3.2 Effects of one-pass conversion on cell performance

Effects of the one-pass conversion on the performance are ascribed to the competition of the mass transport and the reaction. As mentioned above, when the one-pass conversion is low, the water produced in the ORR cannot humidify the cell sufficiently, resulting in high proton transfer resistance and poor cell performance. However, as the ORR rate increasing, the average oxygen partial pressure decreases, which is disadvantageous to the ORR, as shown in Fig. 4.8(d). When the one-pass conversion is low, the decrease in ohmic resistance and increase in effectiveness factor due to the water produced in the ORR have more significant effects than the decrease in the average oxygen partial pressure, resulting in the increase of the output current density. On the other hand, when the one-pass conversion is high, the decrease in the ohmic resistance and mass transport resistance cannot reverse the decrease in the average oxygen partial pressure. As a result, the output current density firstly increases and then decreases as the one-pass conversion increases, due to the competition of mass transport and ORR, as shown in Fig. 4.6(a).

By increasing the one-pass conversion, the proton conductivity increases. According to the definitions of the dimensionless moduli (Eqs. (4.9) – (4.10)), our modulus M_{pm}, which represents the ratio of proton transport resistance to ORR resistance[7], decreases while the one-pass conversion increases. On the other hand, although the ORR rate constant k_{vcm} increases due to the decreased ohmic resistance and the decreased emf, the
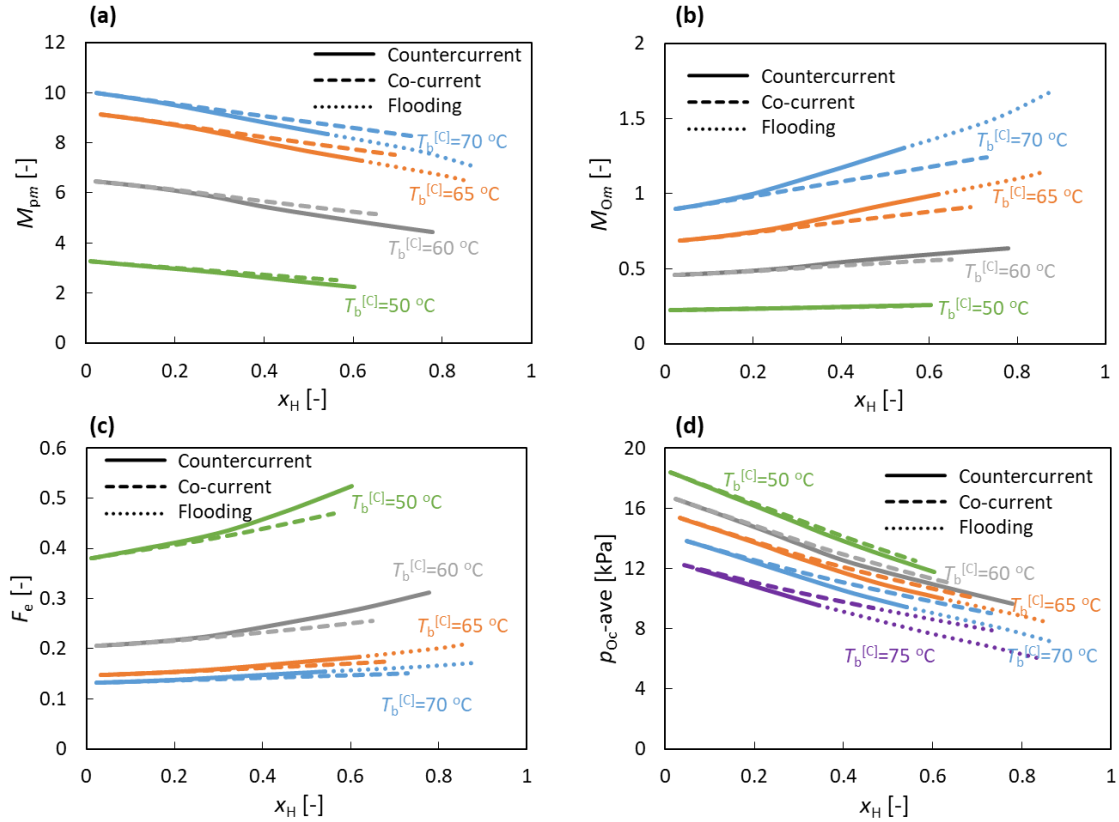
Figure 4.8: Impacts of one-pass conversion on (a) Our modulus, (b) Thiele number, (c) effectiveness factor and (d) average oxygen partial pressure in cathode gas channel (cell voltage = 0.6 V)

Thiele number M_{Om} which represents the ratio of the oxygen diffusion resistance to the ORR resistance[7], increases quite slowly comparing to M_{pm} decreasing while the one-pass conversion increases, as shown in Figs. 4.8(a) – (b). That indicates the decrease in the proton transport resistance is more significant than the oxygen diffusion resistance increase comparing to the ORR resistance, while the one-pass conversion increases. As a result, when the one-pass conversion increases, the effectiveness factor increases, as shown in Fig. 4.8(c).

4.3.3 Optimization of operating conditions

As mentioned above, when the average RH is higher than 0.37, the countercurrent operation exhibits higher performance than the co-current operation, but the flooding is more likely to take place. When the humidifier temperature is low, the co-current setup can be chosen to prevent the flooding at high one-pass conversion.

Since decrease in the proton transfer resistance is more significant than the oxygen transfer resistance increases when the one-pass conversion increases, especially at the
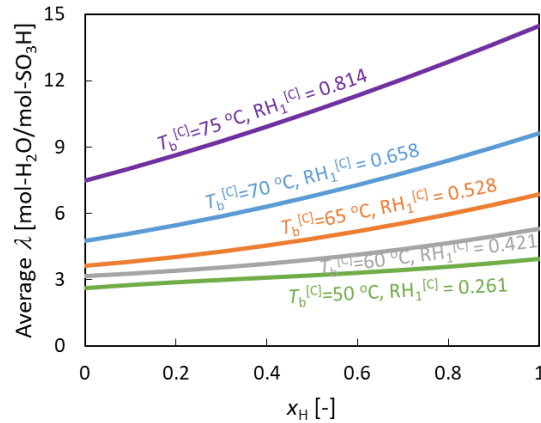
Figure 4.9: The average PEM moisture content under different one-pass conversion

high humidification temperature, the cell performance can be improved effectively by increasing the one-pass conversion. However, according to Fig. 4.6(a), the current density increases slowly at the same cell voltage when the one-pass conversion is low, both of the proton transfer resistance in CCL and the ohmic resistance in PEM are high, which indicates that the cell is not well humidified.

The average RH of cathode can be calculated from Eq. (4.20) derived from Eq. (4.19) according to the material balance, where y_{O0} is the dry-based oxygen mole fraction of cathode inlet air. As the x_H increasing, the average RH increases nearly linearly, but the PEM moisture content increases slowly at first and quickly then. The inflection point shown in Fig. 4.7 is at RH = 0.37 or PEM moisture content at 3.0, which indicates that when the average PEM moisture content is higher than 3.0, the boost of the proton conductivity as well as the cell performance by humidification is more obvious. Fig. 4.9 shows the average PEM moisture content under different one-pass conversion, which is calculated by Eqs. (4.7) and (4.20). When the PEM moisture content is more than 3.0, the slope of the curves becomes larger which indicates that the higher one-pass conversion offers higher average PEM moisture content, as well as better cell performance. Therefore, the lower limit of one-pass conversion can be given by Eq. (4.21) derived from Eq. (4.20), where the minimal average cathode RH can be regarded as 0.37. It should be noted that the RH of anode which is determined by Eq. (4.5) is difficult to be evaluated, so that the total PEM moisture content is estimated from the average cathode RH instead. Therefore, the total PEM moisture content is overestimated, since the anode RH is usually lower than the cathode RH, so that the valued obtained by Eq. (4.21) is underestimated.
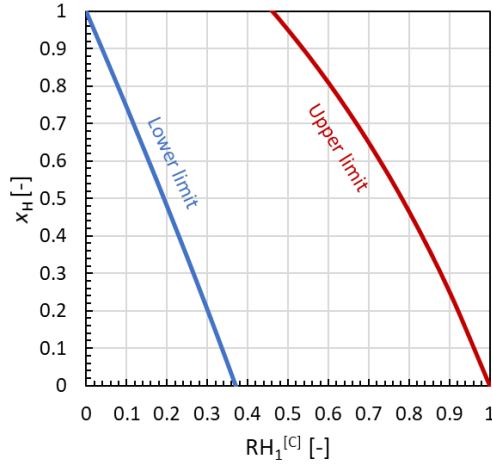
Figure 4.10: Operating limitation of hydrogen one-pass conversion

$$\overline{RH}^{[C]} \approx \frac{RH_1^{[C]} + RH_2^{[C]}}{2} = \frac{RH_1^{[C]} + \left(\dfrac{RH_1^{[C]}}{2} + \dfrac{1}{y_S^{sat}}\right)\left(1 - RH_1^{[C]}y_S^{sat}\right)y_{O0}x_H}{1 + \left(1 - RH_1^{[C]}y_S^{sat}\right)y_{O0}x_H} \tag{4.20}$$

$$x_{H,min} = \frac{\overline{RH}_{min}^{[C]} - RH_1^{[C]}}{y_{O0}\left(1 - RH_1^{[C]}y_S^{sat}\right)\left(\dfrac{RH_1^{[C]}}{2} + \dfrac{1}{y_S^{sat}} - \overline{RH}_{min}^{[C]}\right)} \tag{4.21}$$

On the other hand, to prevent flooding, the one-pass conversion should be less than the value calculated from Eq. (4.22), which is derived from Eq. (4.19). The $RH^{[C]}_{2,flood}$ is the RH of the cathode outlet gas when the flooding happens, which can be regarded as 1 in case of co-current operation. In case of countercurrent, the maximum $RH^{[C]}$ exists in the cathode channel instead of the outlet, therefore the valued obtained by Eq. (4.22) is overestimated.

$$x_{H,max} = \frac{(RH_{2,flood}^{[C]} - RH_1^{[C]})y_S^{sat}}{(2 - RH_{2,flood}^{[C]}y_S^{sat})(1 - RH_1^{[C]}y_S^{sat})y_{O0}} \tag{4.22}$$

Fig. 4.10 shows the operating limitation of hydrogen one-pass conversion, which was obtained by Eqs. (4.21) and (4.22). Although the optimal one-pass conversion can be obtained from Fig. 4.6(a), the value is complicated to calculate, so that the value usually depends on the experience. On the other hand, when the optimal one-pass conversion is higher than the upper limit given by Eq. (4.22), the actual one-pass conversion should be lower than the upper limit.

4.4 Conclusions

Since the co-current operation has more uniform water permeation flux distribution, the flooding is less likely to occur, comparing to the countercurrent operation in the PEFC system with hydrogen recirculation. When the current density and the one-pass conversion are determined, the difference between the co-current and the countercurrent operations is not remarkable in case of poor humidification and low one-pass conversion, although the better cell performance by the co-current operation can be predicted. On the other hand, the countercurrent operation attains better performance when the bubbler temperature is high, due to the larger RH range and higher average PEM moisture content.

The effect of one-pass conversion on performance is determined by the competition of mass transport resistance and the reaction resistance. The proton transfer resistance decreases and the oxygen transfer resistance increases, as the one-pass conversion increasing. The decrease in proton transfer resistance is more remarkable than the increase in oxygen transfer resistance, resulting in effectiveness factor increasing. However, the ORR rate decreases due to the decrease in the oxygen partial pressure averaged over a flow channel, as the one-pass conversion increasing. As a result, the maximum current density exists at fixed cell voltage.

To humidify the cell sufficiently, the one-pass conversion is required to be higher than the value which offers the average RH of cathode and anode higher than 3.7. And to prevent the flooding, the one-pass conversion should be lower than the value at which water vapor is saturated in the gas channel.

4.5 Symbols

A_h	Electrode area per unit length of the gas channel	[m^2/m]
a	Water vapor activity	[-]
a_A	Electroosmosis drag coefficient	[mol/mol]
b_c	Tafel slope	[V]
$c^{(M)}$	Ion exchange capacity of PEM	[mol/kg]
$D_{eA}^{(M)}$	Effective H_2O diffusivity in PEM	[m^2/s]
$D_{eO}^{(C)}$	Effective O_2 diffusivity in CCL	[m^2/s]
$D_{eO}^{(D)}$	Effective O_2 diffusivity in GDL	[m^2/s]

E_{cm}	IR corrected cell voltage	[V]
F	Faraday constant	[C/mol]
F_i	Molar flow rate of species i	[mol/s]
i	Current density	[A/cm^2]
$k_{mc}\oplus$	Reaction constant at Emf = 0 per unit platinum mass	[mol/(Pa·kg·s)]
k_{vcm}	1st-order cathode reaction rate constant per layer volume	[mol/(Pa·m^3·s)]
L	Length at gas channel	[m]
l	Location of gas channel	[m]
M_{Om}	Thiele modulus	[-]
M_{pm}	Our modulus	[-]
$N_A^{(M)}$	Water permeation flux through PEM	[mol/(m^2·s)]
N_g	Total gas flux	[mol/(m^2·s)]
N_O	Oxygen flux	[mol/(m^2·s)]
P_{Om}	Péclet mumber	[-]
p_O	Partial pressure of oxygen	[Pa]
R	Molar gas constant	[J/(K·mol)]
$R^{(M)}$	Electrical resistance of PEM	[Ω·cm]
T	Temperature	[K]
T_b	Humidification temperature in bubbler	[K]
V	Cell voltage	[V]
x_H	Hydrogen conversion	[-]
y_O	Oxygen mole fraction	[-]
y_{O0}	Dry-based oxygen mole fraction of cathode inlet air	[-]
y_S^{sat}	Water steam mole fraction in saturated water vapor	[-]
z	Location at MEA thickness direction	[m]

Greeks

ε_I	Ionomer volume fraction	[-]
$\delta^{(C)}$	Thickness of CCL	[m]
λ	Moisture content of PEM	[mol/mol]
$\rho^{(M)}$	Density of PEM	[kg/m^3]
ρ_b	Platinum loading per unit layer volume	[kg/m^3]
$\sigma_{ep}^{(C)}$	Effective proton conductivity	[S/m]
$\sigma_p^{(M)}$	Proton conductivity of PEM	[S/m]

Subscripts

1	Cell inlet
2	Cell outlet

c	CCL–GDL boundary
d	GDL–gas channel boundary
m	CL–PEM boundary
-m	PEM–CCL boundary
S	Water steam
H	Hydrogen
N	Nitrogen
O	Oxygen

Superscripts

[A]	Anode channel
[C]	Cathode channel
(C)	Cathode catalyst layer
(D)	GDL
(M)	PEM

4.6 References

[1] M. Ji, and Z. Wei, *Energies*, **2**, 1057–1106 (2009).

[2] G. Inoue, T. Yoshimoto, Y. Matsukuma. M. Minemoto, H. Itoh, and S. Tsurumaki, *J. Pow. Sour.*, **162**, 94–104 (2006).

[3] A.A. Kulikovsky, *Electrochim. Acta*, **49**, 617–625(2004).

[4] T. Kitahara, H. Nakajima, and K. Ishikawa, *ECS Trans.*, **75**(14), 209–217(2016).

[5] T. Kitahara, H. Nakajima, and K. Ishikawa, *J. Electrochem. Soc.*, **163** (13), F1366–F1372 (2016).

[6] M. Kawase, H. Takesue, K. Mizuno, and K. Miura, *212th ECS Meet. Abstr.*, 518 (2017).

[7] M. Kawase, K. Sato, R. Mitsui, H. Asonuma, M. Kageyama, K. Yamaguchi, and G. Inoue, *AIChE J.*, **63**(1), 249–256 (2017).

[8] G. Inoue, M. Kawase, K. Yokoyama, J. Oyama, T. Terao, and N. Kubo, 228th ECS Meeting (Phoenix), #1285 (2015).

[9] S. Ge, X. Li, B. Yi, and I-M. Hsing, *J. Electrochem. Soc.*, **152** (6), A1149–A1157 (2005).

[10] P. Rodatz, F. Büchi, C. Onder, and L. Guzzella, *J. Pow. Sour.*, **128**, 208–217 (2004).

Conclusions

Addressing in climate change and energy shortage, the PEFC technology has been focused for decades, which is expected to be further developed and commercialized in the world-wide range. Along with the endeavor of exploring the novel material for the catalyst to improve the performance and reduce the cost, the enhancement of the mass transport is comparably significant. The introduction chapter summarized attempts and methods of improving the mass transport in prior study, which found that the optimizations of flow fields and operating conditions provide promising solutions for the issues. However, a comprehensive and computationally inexpensive model is required to understand the complicated processes and offer theoretical basis for PEFC design procedure. In addition, the perspectives in chemical engineering are potentially available for PEFC modeling. Therefore 4 topics were discussed in this dissertation.

Summary of main conclusions

In Chapter 1, the intrinsic ORR kinetics, effective oxygen diffusivity and proton conductivity were derived from the Pt-loading dependency by the isothermal CCL dimensionless model. The determined dimensioned properties have good agreement with the literature values, whereas more accurate experimental data is required for the analysis in this model. The dimensionless moduli derived from the experiments demonstrates that the proton transport resistance is 5.7 times to the oxygen transport resistance in the CCL. The results also indicate that the higher Pt-loading offers better cell performance but lower effectiveness factor due to the limitation of the mass transport, which infers that the Pt cannot be utilized efficiently when the Pt-loading is too high. Moreover, the model successfully reproduced the experimental data in the oxygen conversion region lower than 0.10, where the in-plane distributions of physicochemical properties can be ignored.

In chapter 2, the effects of gas macromixing in 2 typical gas channels, *i.e.,* parallel and serpentine, on the cell performance were analyzed by RTD method and reactor compartmental model. The cell performance with different gas flow rate and active area was well explained by simplifying the parallel and the serpentine channels by 22.4 % PFR followed by 77.6 % CSTR and 42.6 % PFR followed by 57.4 % CSTR respectively.

Moreover, the self-catalytic reaction behavior of ORR was observed experimentally. The water humidification is more beneficial at low oxygen conversion, but the oxygen consumption draws back the cell performance, which implies that the gas macromixing is beneficial at low oxygen conversion. Therefore, the parallel the serpentine channel have better performance at low and oxygen conversion respectively. It also indicates that a structure which promotes the gas macromixing can be designed near the cell inlet in the gas channel to improve the cell performance.

Chapter 3 demonstrates more detailed mass transport mechanism in the different flow fields, especially in the partially narrowed flow fields, which aims at forcing the diving flow and cross flow to enhance the mass transfer. The results analyzed by CFD technique had a good agreement with the experimental results, which found that although the pressure drop becomes higher, the net power density increases 11.3 % in cases of partially narrowed flow fields comparing to the conventional parallel flow fields. According to the numerical simulation, the diving gas and cross flowing gas were 2.8–4.5 % and around 2 % to the gas flowing in the partially narrowed channels. Moreover, the convergence of the gas in the channel and the eddies forming before and behind the baffles promotes the gas mixing, so that the oxygen concentration on the GDL surface increases. Therefore, an appropriate span between neighboring baffles should be designed to maximally benefit from the gas mixing effects. It should be noted that the Venturi effect occurring under the narrowed channel prevents the mass convection between adjacent channels, especially in the neat-arranged pattern, so that the staggered pattern is preferable.

In Chapter 4, the effects of gas flow directions in the PEFC system with hydrogen recirculation were explored by isothermal PFR + CCL dimensionless model, in the perspective of water management. Although the counter current flow pattern offers better performance in the high RH conditions, which is usually applied in the practical uses, it can be predicted that the co-current flow pattern provides better performance in the low RH conditions, due to the different concavity and convexity of the relationship between RH and moisture content of Nafion electrolyte membrane. Furthermore, the effects of hydrogen one-pass conversion were also discussed. Since the proton transport resistance is more remarkable than the oxygen transport resistance, sufficient humidification is of vital importance, and the one-pass conversion is required to be higher than the value which offers the average RH of cathode and anode higher than 3.7. And to prevent the flooding, the one-pass conversion should be lower than the value at which water vapor is saturated in the gas channel.

Outlook of this study

Although considerable models for understanding the reaction and mass transport in PEFC were suggested in this study, some challenges still remain to be solved, which provides the potential directions for the future works.

Firstly, the analysis by the CCL dimensionless model mentioned in chapter 1 could not explain the experimental data at high oxygen conversion, where the effects of the uneven distributions of physicochemical properties was not estimated. 2 methods can be considered to solve this question: (1) to calculate the in-plane distributions of properties; (2) to substitute the average properties. The former method was applied in chapters 3–4, which is computationally expensive, so that the latter method is preferable.

Then, to develop the second method mentioned above, a new question appears: which value should be applied to represent the whole cell. The answer strongly depends on the flow fields design. The model mentioned in chapter 2 may provide a potential suggestion to this question. However, the reactor model suggested from the RTD characterization has many solutions, the compartment model of PFR and CSTR is the simplest one, and more accurate model can be supposed.

Next, a practical and further simplified model for the complex flow fields mentioned in chapter 3 is expected to be suggested. The model is required to have rapid computational capacity to estimate the diving and cross flow rate and the effects of them on the net power output from the flow field design. The solution of this question also relates to the optimization of flow field design.

Finally, the models in this dissertation were reasonably built on the hypothesis of relatively dry condition and steady states. However, accompanied with the unsteady behavior of water droplets in the cell, the time-dependent or periodic phenomenon is common in the practical application, especially in the FCV. Comparing to the relatively quick response of the oxygen and proton transport on the cell performance, the water transport is usually the limit step to prevent the cell approaching steady states. Therefore, the time-dependent or quasi-steady model for developing the operation strategy in a wide-range application is another challenge in the future work.

In summary, due to the complicated processes in PEFC, multiple parameters should be optimized. More exploration on the phenomenon in the cell level is required, and further practical model which can reduce the dimensions should be developed. The development of design procedure of PEFC is still an issue remained to be further resolved.

Acknowledgement

researchers Dr. Dalia Heggo and Mr. Kazuhiro Yamaguchi previously in the PEFC team, who offered me many suggestions when I was a new comer and unfamiliar with my topic.

Thanks also go to many colleagues and friends. It is a great pleasure to meet them in this laboratory. Kanata Murase patiently showed me the way of operating the experimental devices and analyzing the data, so that I could start my study in the first place. Hikaru Ogawa is always hardworking, which is also a great encouragement to me. A lot of meaningful discussions with him clarified my thoughts and broaden my horizons. Jie Ren and Yafei Li also provided me numerous helps and suggestions, so that I even did not feel like being far from my motherland. Moreover, I would be remiss in not mentioning the colleagues and friends, *e.g.*, Beste Balci, Kai-Hung Cheng, and Ziguang Yang, who were also stepping forward to the academic success. There were many others who worked together with me I could not completely list, but I will keep all of them in my mind.

Last but not least, my sincerest appreciation goes to my family, who have supported me unconditionally through many difficult moments during the past years. It is safe to say that I will never complete my work without them.

To close I would like to say that it is for all of their efforts that I could present this dissertation.

Ma Yulei

February 2023

List of Publication

Papers

1. Y. Ma, D. Heggo, M. Kageyama, K. Yamaguchi, and M. Kawase. Determination Method of Dimensionless Moduli from Pt-loading Dependency of ORR in Cathode Catalyst Layer of Polymer Electrolyte Fuel Cell. In preparation. (Chapter 1)

2. D. Heggo, Y. Ma, B. Balci, M. Kageyama, K. Yamaguchi, and M. Kawase (2019). Effect of Cathode Catalyst Layer Structure on the Performance of PEFC. *ECS Trans.*, **92** (8), 165−174. (Paper included in Chapter 1)

3. M. Kageyama, K. Yamaguchi, D. Heggo, Y. Ma, H. Ogawa, and M. Kawase (2020). Determination Method of Dimensionless Moduli for Estimation of PEFC Performance. *ECS Trans.*, **98** (9), 163−175. (Paper included in Chapter 1)

4. Y. Ma, M. Kageyama, and M. Kawase (2021). Performance of PEFC under Different Gas-mixing Conditions. *ECS Trans.*, **104** (8), 205−220. (Chapter 2)

5. Y. Ma, M. Kageyama, and M. Kawase. Effects of Gas Macromixing in Polymer Electrolyte Fuel Cell. In preparation to be submitted to *J. Eletrochem. Soc.* (Chapter 2)

6. Y. Ma, H. Gyoten, M. Kageyama, and M. Kawase (2022). Effects of Partially Narrowed Flow Channel on Performance of Polymer Electrolyte Fuel Cell. *ECS Trans.*, **109** (9), 171−197. (Chapter 3)

7. Y. Ma, H. Gyoten, M. Kageyama, and M. Kawase. Effects of Partially Narrowed Flow Channel on Performance of Polymer Electrolyte Fuel Cell. In preparation to be submitted to *J. Eletrochem. Soc.* (Chapter 3)

8. Y. Ma, K. Yamaguchi, M. Kageyama, and M. Kawase (2020). High Effeciency Operating Conditions in Polymer Electrolyte Fuel Cell System with Hydrogen Circulation. *ECS Trans.* **98** (9), 291−303. (Chapter 4)

Conferences

1. Y. Ma, M. Kageyama, and M. Kawase, "Performance of PEFC Under Different Gas-Mixing Conditions", ECS 240th, I01A-1080, Orland, U.S. (Oct. 2021) (Oral presentation) (Chapter 2)

2. Y. Ma, H. Gyoten, M. Kageyama, and M. Kawase, "Effects of Partially Narrowed

Flow Channel on Performance of Polymer Electrolyte Fuel Cell", ECS 242nd, I01B-1454, Atlanta, U.S. (Oct. 2022) (Oral presentation) (Chapter 3)

3. Y. Ma, K. Yamaguchi, M. Kageyama, and M. Kawase, "High Efficiency Operation Conditions in Polymer Electrolyte Fuel Cell System with Hydrogen Circulation", PRiME 2020, I01B-2211, Honolulu, U.S. (Oct. 2020) (Oral presentation) (Chapter 4)

4. Y. Ma, K. Yamaguchi, M. Kageyama, and M. Kawase, "Effect of Gas Flow Direction in Polymer Electrolyte Fuel Cell System with Hydrogen Recycling", ISChE 2019, OB09, Daejeon, Korea (Dec. 2019) (Oral presentation) (Chapter 4)

5. Y. Ma, K. Yamaguchi, M. Kageyama, and M. Kawase, "Distribution of Water Permeation in Polymer Electrolyte Fuel Cell System with Hydrogen Recycling", APCChE 2019, M223, Sapporo Japan (Sep. 2019) (Oral presentation) (Chapter 4)